

Inferring Air-Sea Carbon Dioxide Fluxes from Scatterometer Sea Surface Backscatter

Dissertation

zur Erlangung des Doktorgrades
an der Fakultät für Mathematik, Informatik und Naturwissenschaften
im Fachbereich Geowissenschaften
der Universität Hamburg

vorgelegt von
Marjan Ghobadian

Hamburg 2017

Gutachter:

Prof. Dr. Detlef Stammer

Dr. Martin Gade

Tag der Disputation:

December 8th, 2017

Declaration

I, Marjan Ghobadian, hereby declare, on oath, that this thesis titled, “Inferring Air-Sea Carbon Dioxide Fluxes from Scatterometer Sea Surface Backscatter” and the work presented in it are entirely my own work and I have acknowledged all sources and aids.

Hamburg, 2017

Marjan Ghobadian

Zusammenfassung

Eine präzise Schätzung der Gasaustausch- Geschwindigkeit an der Schnittstelle von Luft und Meer würde unser Verständnis für den CO₂ Fluss zwischen Atmosphäre und Ozeanen sowie der Leistungsfähigkeit der Ozeane als Kohlenstoffspeicher verbessern. Die Gasaustausch- Geschwindigkeit, κ , wird von Oberflächenwind durch seinen Einfluss auf die Oberflächenwellen und oberflächennahe Turbulenzen beeinflusst. Normalerweise sind Parameter von κ ausschließlich abhängig von der Windgeschwindigkeit, doch diese Abhängigkeit ist noch nicht vollständig ergründet. Beim Versuch, diese Unsicherheit beim Parametrisieren von κ zu verringern ist es wichtig, den Beitrag von umgebenden Einflüssen zu berücksichtigen.

Diese Arbeit befasst sich mit der Gasaustausch- Geschwindigkeit direkt mit der Unebenheit der Meeresoberfläche gemessen mit einem Mikrowellen Radar zu verknüpfen. Für die Bearbeitung das Ziel wurden Langzeit- Radar Messungen über einen Zeitraum von 27 Monaten in der Jahren 2011 bis 2013 auf der Forschungs- Plattform FINO-2 in der westlichen Ostsee durchgeführt, mit einem Multi-Frequenz und Multi-Polarisations Radar, dem Multi³Scat der Universität Hamburg. Die Radarmessungen wurden in Bezug gesetzt mit weiteren Umgebungsdaten bereitgestellt durch die Forschungsplattform, wie z.B. Luft- und Wassertemperatur, Wind- und Wellenparameter sowie CO₂ Flüsse.

Der erste Teil der vorliegenden Dissertation bewertet die Leistungsfähigkeit des neuen Scatterometers im Hinblick auf einzelne und kombinierte Radarsysteme. Um die Qualität der Daten zu gewährleisten, werden die Beobachtungen der Meeresoberfläche des Multi³Scat gegen theoretische Radarrückstreuung und geophysikalische C-band Modell Rechnungen (CMOD5) getestet. Die Abhängigkeit der Radarrückstreuung im Hinblick auf Wind geschwindigkeit und -Richtung, atmosphärische Schichtenbildung und Wellen-Parameter werden bei verschiedenen Radareinstellungen validiert und der optimale Aufbau für die Studie stellt sich als C-Band in HH- und VH-Polarisationen heraus. Radarquerschnitte (Radar Cross Section (RCS)) aus einer Kombination von vier Mikrowellen Frequenzen, vier Polarisationen Kombinationen und drei verschiedenen Einfallswinkeln gemessen vom Multi³Scat liefert uns ein einzigartigen Einblick in die statistische Charakteristik der Meeresoberflächen- Unebenheit. Die mittlere Wellen- Neigung wird berechnet mit dem Integral des Wellenzahlen-Spektrums

über den Wellenzahlen- Bereich $20 < k < 350$ rad/m aufgenommen vom Multi³Scat (relevanter Bereich für Gasaustausch- Analyse). Die Multi³Scat Beobachtungen uns quantitative Informationen über die Meeresoberflächen- Unebenheit verschaffen, welche direkt im Zusammenhang mit der Energie der Kapillar- Gravitationswellen steht, welche verantwortlich sind für den Gasaustausch. Die Kreuz-Radarrückstreuung zeigt eine schwache Richtungsabhängigkeit bei Variation des Windes. Gleichzeitig zeigt sie die geringste Signal- Sättigung bei hoher Windgeschwindigkeit und wenig Abhängigkeit von der Beobachtungsgeometrie, was den Vorteil dieser Einstellung für die Gasaustausch- Analyse hervorhebt. Die horizontal polarisierte Radarrückstreuung hat eine höhere Empfindlichkeit gegenüber zwingende und Wellen-Parametern. Diese Empfindlichkeit kann dem Beitrag der Wellenunterbrechung in den Nicht-Bragg-Teilen des Signals zugeschrieben werden, die bei horizontaler Polarisation signifikant ist. Neben der Polarisation zeigen steilere Einfallswinkel und höhere Mikrowellenf- requenzband-Radar-Rückstreuung eine höhere Empfindlichkeit gegenüber den Umwelteinflüssen.

Der zweite Teil der Arbeit untersucht die Korrelation zwischen der Radarrückstreuung von der Meeresoberfläche und der Gasaustausch- Geschwindigkeit und entwickelt eine neue Parametrisierung für die Gasaustauschsschätzung. Die Multi³Scat Messungen in Kombination mit weiteren Daten benutzt werden um auf die Gasaustausch- Geschwindigkeit zu schließen als eine Funktion aus Windgeschwindigkeit und mittlerer Oberflächenwellenneigung (Oberflächen- Unebenheit). Das lineare Verhältnis zwischen Gasaustausch- Geschwindigkeit und mittlerer Wellenneigung führt zu, eine vorläufige Schätzung der Gasaustausch- Geschwindigkeit als eine Funktion des Radar- Querschnitts der Meeresoberfläche. Im Vergleich zu den traditionellen windbasierten Gasaustausch- Parametrisierungen zeigt die neu verbesserte scatterometerbasierte Gasaustausch- Parametrisierungen eine gute Korrelation zur Beobachtung ($R^2 = 0.84$, RMSE = 9.7 cm/h), besser als die der windbasierten Parametrisierung. Der gemittelte Wert der Gasaustausch- Geschwindigkeit unter Verwendung von Scatterometerdaten beträgt etwa 26.95 cm/h und liegt nahe bei dem gemeldeten Wert für Offshore-Meere. Der durchschnittliche CO_2 -Fluss, $0,23 \mu\text{molm}^{-2}\text{s}^{-1}$, geschätzt mit dem neuen scatterometerbasierte Gasaustausch- Parametrisierungen, führt zu einem Wert in der Nähe den beobachteten Wert, $0,21 \mu\text{molm}^{-2}\text{s}^{-1}$. Zusätzlich hat die Dauer der Messperiode befähigt, saisonale Variationen des CO_2 Flusses, der Austauschgeschwindigkeit und der Meeresoberflächenunebenheit zu untersuchen. Insgesamt zeigen die Ergebnisse eine relativ akkurate Schätzung der Gasaustausch- Geschwindigkeit basiert auf der Radarrückstreuung, welche die Saisonabhängigkeit der Kombination der Komponenten berücksichtigt, die Einfluss auf den Gas-Austausch über die Luft-Wasser Schnittstelle hat. Solch ein Schätzalgorithmus kann weiterführend mit Satelliten Daten verwendet werden um globale Gasaustausch- Geschwindigkeiten abzufragen.

Abstract

An accurate estimate of the gas transfer velocity across the air-sea interface would improve our understanding of the CO₂ flux between the atmosphere and ocean, and of the efficiency of the ocean as a carbon sink. Gas transfer velocity, κ , is influenced by the surface wind stress through its impact on surface waves and near-surface turbulence fields. Typical parameterizations of κ are solely wind speed dependent, but this single forcing dependence is still not fully understood. In an attempt to reduce the uncertainty in κ parameterization, it is important to consider the contribution of environmental forcings and surface/interface parameters on gas transfer velocity estimation.

The objective of this thesis is to directly link the gas transfer velocity to the sea surface roughness obtained from a microwave scatterometer. To address the objective, a long-term radar backscatter measurements were carried out during a period of 27 months in 2011-2013 on the research platform FINO-2 in the Western Baltic Sea by using the multi-frequency and multi-polarization microwave scatterometer, Multi³Scat, of the University of Hamburg. The radar measurements have been correlated with the environmental data collected at the platform, such as air and water surface temperatures, wind and wave parameters, as well as CO₂ fluxes.

The first part of the thesis evaluates the performance of the new scatterometer for individual and combined radar arrangements. To assure the quality of the data, the Multi³Scat observations of the sea surface are evaluated against the scattering theory and C-band geophysical model function (CMOD5). The radar backscatter dependencies on wind speed and direction, atmospheric stratification, and wave parameters are validated at different radar settings and the optimal setup for the study turns out to be C-band in HH and VH polarizations. The combination of four microwave frequencies, four polarization combinations, and three incidence angles radar backscatter measured by the Multi³Scat lead to a unique spectrum, which results in a significant information on the statistical characteristics of sea-surface roughness. The mean square surface wave slope is computed using the integral of the wavenumber spectrum over the wavenumber ranges $20 < k < 350 \text{ rad/m}$ detected by the Multi³Scat (relevant range for gas transfer analysis). The quantitative information on the sea

surface roughness obtained from the Multi³Scat observations can be attributed to the energy dissipated by the combination of the capillary-gravity waves, which are responsible for gas exchange. The cross polarization radar backscatter shows weak directional dependencies to wind variation. At the same time, it shows the weakest signal saturation at high wind speed and weak dependencies to the observational geometry, which represents the advantage of this setting for gas transfer analysis. The horizontal polarization radar backscatter shows a high sensitivity to environmental forcing and wave parameter. This sensitivity can be attributed to the contribution of the wave breaking in the non-bragg parts of the signal, which is significant in horizontal polarization. Besides the polarization, steeper incidence angle and higher microwave frequency band radar backscatter show higher sensitivity to the environmental forcings.

The second part of the thesis investigates the correlation between the radar backscatter from the sea surface and gas transfer velocity and develops a new parameterization for gas flux estimation. The Multi³Scat measurements, in combination with auxiliary data, are used to infer air-sea CO₂ transfer velocity as a function of wind speed and mean square surface wave slope (surface roughness). The linear relationship between gas transfer velocity and mean square slope leads to a preliminary estimation of gas transfer velocity from the radar cross section of the sea surface. In comparison to the traditional wind-based gas transfer parameterizations, the newly improved scatterometer-based gas transfer parameterization shows a good correlation to the observation ($R^2 = 0.84$, $RMSE = 9.7 \text{ cm/h}$), better than that of wind-based gas transfer parameterizations. The averaged value of gas transfer velocity using scatterometer data is about 26.95 cm/h and is close to the reported value for offshore seas. The averaged CO₂ flux of $0.23 \mu\text{molm}^{-2}\text{s}^{-1}$, estimated by using the new scatterometer based transfer velocity parameterization, results in a very close value to the observed value of $0.21 \mu\text{molm}^{-2}\text{s}^{-1}$. In addition, the extent of the measurement period has enabled us to study the seasonal variability of the CO₂ flux, transfer velocity, and sea surface roughness. Overall, the results indicate a relatively accurate estimation of gas transfer velocity derived from microwave backscatter, which considers the seasonality of the combination of the components influencing the gas exchange across the air-sea interface. Such an estimation algorithm can further be employed by satellite data to retrieve global gas transfer velocities.

Contents

Declaration	i
Zusammenfassung	iii
Abstract	v
1 Introduction	1
1.1 Motivation	1
1.2 Goals of the thesis	7
1.3 Structure of the thesis	8
2 State of the art surface CO₂ flux estimation	9
2.1 Air-sea CO ₂ flux estimation	9
2.2 Review of techniques to measure air-sea CO ₂ flux	11
2.2.1 Direct flux measurement technique- Eddy covariance system	11
2.2.2 Bulk formulation	12
2.2.3 Remote sensing technique	12
2.3 Wind-based-CO ₂ transfer velocity	14
3 State of the Art Sea Surface Scatterometry	17
3.1 Microwave interaction with the sea surface	17
3.2 Bragg scattering	19
3.2.1 Bragg scattering model	21
3.3 Composite surface model	22
3.4 Non-Bragg scattering	23
3.5 Geophysical model function	24
3.5.1 Empirical relationship	24
3.5.2 C-band model function	25

4	Experiment and Methodology	29
4.1	Study area-Western Baltic Sea	29
4.2	Instrumentation	31
4.2.1	The scatterometer Multi ³ Scat	31
4.2.2	The research platform, FINO-2	35
4.3	Auxiliary Data	36
4.3.1	Wind	37
4.3.2	Air temperature	37
4.3.3	Buoy data	38
4.3.4	CO ₂ observations in FINO-2	41
5	Multi³Scat observations of sea surface	45
5.1	RCS dependence on Frequency, Polarization, and Incidence angle	46
5.1.1	Incidence angle dependence	46
5.1.2	The effect of different polarizations	52
5.2	Radar cross section dependence on wind and wave parameters	56
5.2.1	Wind speed influence	56
5.2.2	Effect of azimuth angle	63
5.2.3	Effect of atmospheric stability	70
5.2.4	Wave parameters impact on radar backscatter	73
5.3	Concluding remarks	76
6	Air-Sea CO₂ exchange and radar backscatter	79
6.1	CO ₂ flux and transfer velocity analysis	79
6.1.1	Seasonal variation of gas transfer velocity	85
6.2	Flux estimation using Radar observations	88
6.2.1	Algorithm description	88
6.3	Concluding remarks	99
7	Conclusion and Recommendations	101
7.1	Summary of the thesis and main conclusions	101
	Appendices	107
A	Radar Cross Section dependence on radar parameters and wind vector	108
A.1	Angular dependence of RCS	109
A.2	RCS dependence on wind speed	111

A.3	Directional dependence of RCS	114
A.4	Multi ³ Scat observation versus CMOD5 retrieved backscatter	117
A.5	Polarization ratio at downwind direction	121
List of Figures		122
List of Tables		130
Abbreviations		132
Symbols		134
Acknowledgements		143

CHAPTER 1

Introduction

1.1 Motivation

Carbon dioxide (CO₂) is the primary greenhouse gas that contributes to the ongoing anthropogenic climate change by changing earth's radiative balance. The Intergovernmental Panel on Climate Change (IPCC) has documented the radiative forcing of each human-activity-induced climate driver based on measurements of the quantities of greenhouse gases in the atmosphere [IPCC AR5; Pachauri et al., 2014]. This report points out a considerably larger radiative effect of CO₂ in the atmosphere than that of all other greenhouse gases, such as methane, nitrous oxide, and water vapor. The main reason for the difference in the radiative effect is that CO₂ is added much faster to the atmosphere and remains much longer in its original form: throughout a period of centuries, compared to a period of decades for methane and nitrous oxide and days for water vapor. The increases in atmospheric CO₂ concentration is mainly caused by the burning of fossil fuels and deforestation. This results in a positive radiative forcing which leads to an uptake of energy by the climate system [IPCC AR5; Pachauri et al., 2014].

Based on observations between 1750 and 2011, the IPCC report concludes that the atmosphere holds about 40% of total anthropogenic CO₂ emissions and that the rest is absorbed by the ocean or the terrestrial biosphere [IPCC AR5; Pachauri et al., 2014]. The ocean absorbs about 30% of CO₂ emissions; therefore, it plays a critical role in balancing the radiative forcing. As long as atmospheric CO₂ concentrations continue to rise, the oceans will continue to take up CO₂ because of its high solubility. However, the rate of uptake is limited by the finite speed of vertical mixing, biological activity, and complex processes in the air-sea interface. The rate of CO₂ absorption by the ocean decreases with increasing CO₂ concentration in the water due to the over-saturation of CO₂. As anthropogenic forcing may slow down ocean circulation due to increased stratification from increased temperature, the water trapped at the surface would become saturated, which would, in turn, reduce the efficiency

of the ocean's CO₂ uptake.

To better understand the climate system's responses to CO₂, it is important to understand the processes determining the air-sea CO₂ exchange, to quantify and parameterize them in terms of large-scale observable quantities and to improve the representation of air-sea CO₂ exchange in climate models. For this to happen, it is important to know the role of the oceans as a carbon sink. In this respect, some of the large unknowns are the processes that influence the air-sea gas exchange. However, estimating CO₂ fluxes at the ocean and the atmosphere interface is challenging.

In general terms, the air-sea CO₂ flux can be expressed as:

$$F = \kappa \alpha (P_{\text{CO}_2, \text{water}} - P_{\text{CO}_2, \text{air}}) \quad (1.1)$$

Here, κ is the gas transfer velocity [cm/h], α is the solubility of the gas in sea-water [$mol\ m^{-3}\ atm^{-1}$], and $P_{\text{CO}_2, \text{water}} - P_{\text{CO}_2, \text{air}} = \Delta P_{\text{CO}_2}$ [μatm] represents the partial pressure difference between sea water and the air above. The equation states that CO₂ exchange across the air-sea interface is proportional to partial pressure of P_{CO₂} between the atmosphere and the ocean, as well as to the gas transfer velocity.

The air-sea partial pressure difference is the thermodynamic driving force for CO₂ flux. It varies mostly due to the changes in the partial pressure of CO₂ in sea water. The atmospheric P_{CO₂} variation is mostly due to the seasonality of terrestrial vegetation. However, this variation is relatively small in comparison with the seasonal variation in the water P_{CO₂}. Basically, the air-sea partial pressure difference is controlled by changes in total CO₂ concentration in the water and the atmosphere, pH, total alkalinity (AT), temperature, salinity, and it also changes zonally and seasonally.

The transfer velocity is the kinetic driver of CO₂ flux and represents the transfer velocity of the gas molecules across the air-sea interface which depends on first order on the turbulence at the air-sea interface. This is mainly explained by the wind speed but is modified also by surface films, breaking waves, rain, boundary layer stability, and the rate of diffusion of the gas through the water, which is temperature dependent (faster at higher temperature).

An example of a resulting time-mean global CO₂ surface flux was presented by [Takahashi et al. \[2009\]](#) using a wind speed dependent parameterization of gas transfer velocity, κ , by [Wanninkhof \[1992\]](#) and the monthly averaged measurements of surface water P_{CO₂} (Figure: 1.1).

Figure 1.1 shows the climatological mean annual air-sea CO₂ flux for the reference year 2000. The tropical ocean is a source area for atmospheric CO₂ and emits $0.69\ PgC\ y^{-1}$. Between latitudes 20° and 50° (both hemispheres) a region of CO₂ uptake is apparent. Another

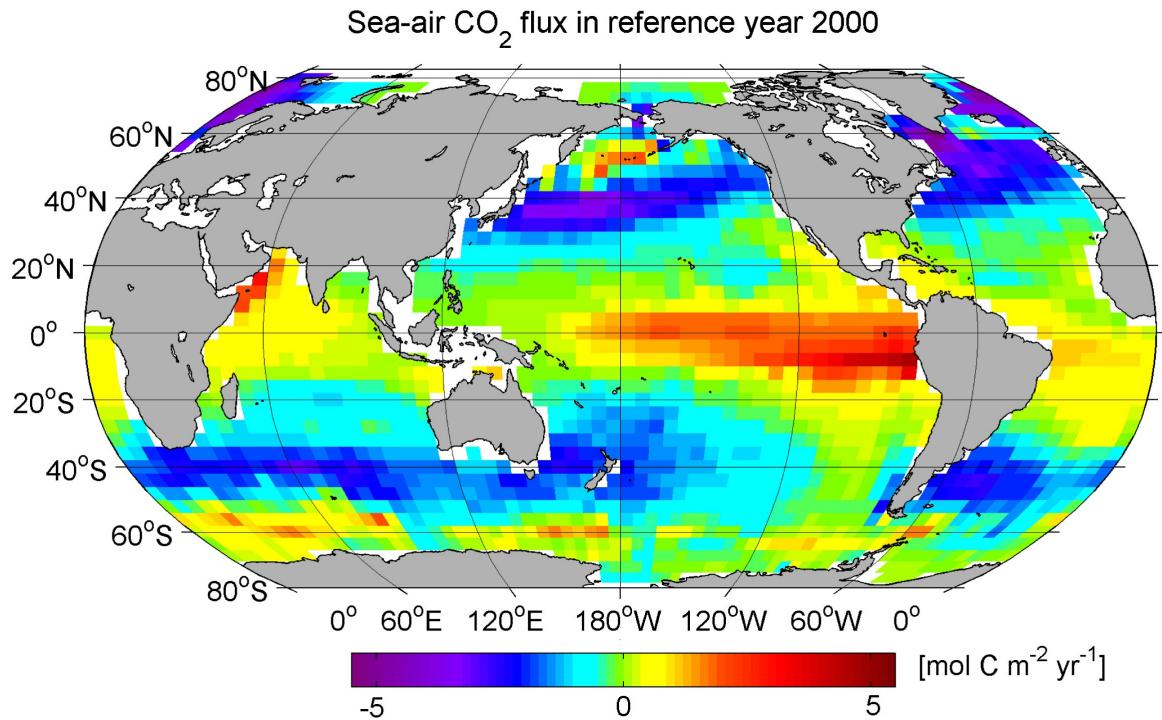


Figure 1.1: Climatological mean annual air-sea CO_2 flux ($\text{mol C m}^{-2} \text{ year}^{-1}$) for the reference year 2000, based on [Takahashi et al. \[2009\]](#). The mean was computed by using the monthly averaged measurements of surface water P_{CO_2} , the NCEP-DOEAMIP-II Reanalysis 6-hours wind speed data, and the quadratic model of transfer velocity with a scaling factor of 0.26.

uptake region with 0.27 PgC y^{-1} is seen at latitudes over 50° N [[Takahashi et al., 2009](#)].

Despite these widely used values, there are considerable uncertainties remaining in the existing estimates of the air-sea exchange of CO_2 [[Lansø et al., 2015](#); [Yu et al., 2014](#); [Jonsson et al., 2008](#); [Takahashi et al., 2002](#)]. This holds for the time mean and especially for the time-varying component. In both cases, uncertainties arise mainly from the two terms: ΔP_{CO_2} and transfer velocity κ . In this context, the relative importance of each term and its uncertainty can vary substantially if we consider time-mean conditions and time-varying conditions. However, there is still insufficient understanding of the processes driving the air-sea gas transfer velocity, κ [[Lansø et al., 2015](#); [Rutgersson et al., 2009](#)]. This thesis is especially concerned with the uncertainties in κ and an attempt to reduce them.

The processes relevant for the variance of transfer velocity will be discussed in Section 2.1. These processes are schematically depicted in Figure 1.2, showing the sensitivity of κ to wind speed and other factors, such as sea surface roughness and near surface turbulence. Surface waves, small scale wave breaking, bubbles, sea spray, rain, and surface films also in-

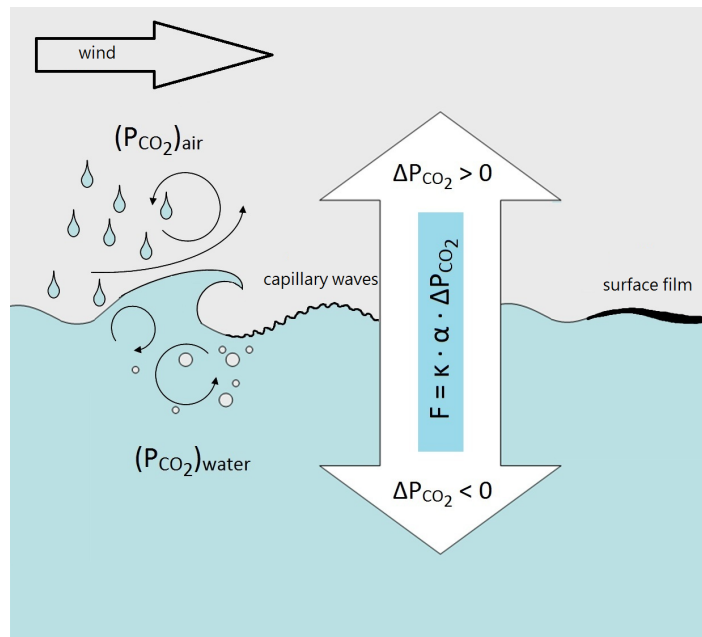


Figure 1.2: Simplified schematic of CO₂ exchange across the air-sea interface (adapted from [Hinrichs, 2014]). The surface films and capillary waves that are riding on top of longer gravity waves are shown, as well as the wave breaking with the sharp crest and bubbles.

fluence the gas exchange across the air-sea interface by influencing the gas transfer velocity [Garbe et al., 2014b]. These parameters also influence the sea surface roughness and near surface turbulence. Therefore, a parameterization of κ using surface/interface parameters may reduce the uncertainty in air-sea gas exchange estimation.

In principle, it is possible to measure the effect of these processes in field campaigns, and account for most of the involved processes, as well as their dependence on large-scale parameters in the ocean and atmosphere. Over the last decade, increased effort, based on laboratory work, modeling and field studies, has been made to improve measurement techniques and parameterizations of gas transfer [Wanninkhof et al., 2009]. In practice, direct measurements of the fluxes over the ocean have proven to be difficult because of the combination of small concentrations and/or small fluxes. Therefore, such measurements are not technically feasible. Nevertheless, a few parameterizations of κ have been proposed to account for its variability and interaction with the large-scale processes influencing the air-sea interface.

Traditional air-sea gas transfer velocity parameterizations use the simple empirical function that depends only on the wind speed [Wanninkhof et al., 2009; Jonsson et al., 2008; Weiss et al., 2007; Ho et al., 2006; Nightingale et al., 2000; Wanninkhof and McGillis, 1999; Wanninkhof, 1992; Cole and Caraco, 1998; Liss and Merlivat, 1986]. These wind-based

parameterizations attempt to relate the gas transfer obtained from deliberate tracer studies, wind tunnel data, and direct covariance flux measurements to the wind speed. These parameterizations are of the basic form:

$$\kappa = au^b (Sc)^n \quad (1.2)$$

where u is the wind speed, a and b are the coefficients determined by experimental data, Sc is the Schmidt number, and the parameter n is an empirical value which varies between $\frac{1}{2}$ (calm surface) and $\frac{2}{3}$ (rough surface) depending on the friction velocity and mean square slope of the waves [Jähne et al. \[1989\]](#). The Schmidt number, Sc , is defined as:

$$Sc = \frac{\text{Kinematic Viscosity in sea water}}{\text{Molecular diffusivity}} \quad (1.3)$$

Figure 1.3 displays the gas transfer velocity obtained from four different wind based parameterizations. The gas transfer velocity estimation from different formulations varies by a factor of 2 or more and causes uncertainties when quantifying the ocean CO_2 sink. These uncertainties are maximal at high wind speeds, reaches to 100 cm/h. [Takahashi et al. \[2002\]](#) show more than 50% variation in the oceanic CO_2 uptake as a consequence of the different wind exponents in gas transfer velocity parameterizations; from the cubic wind dependent function to the quadratic function. This uncertainty comes from the dependence of the gas

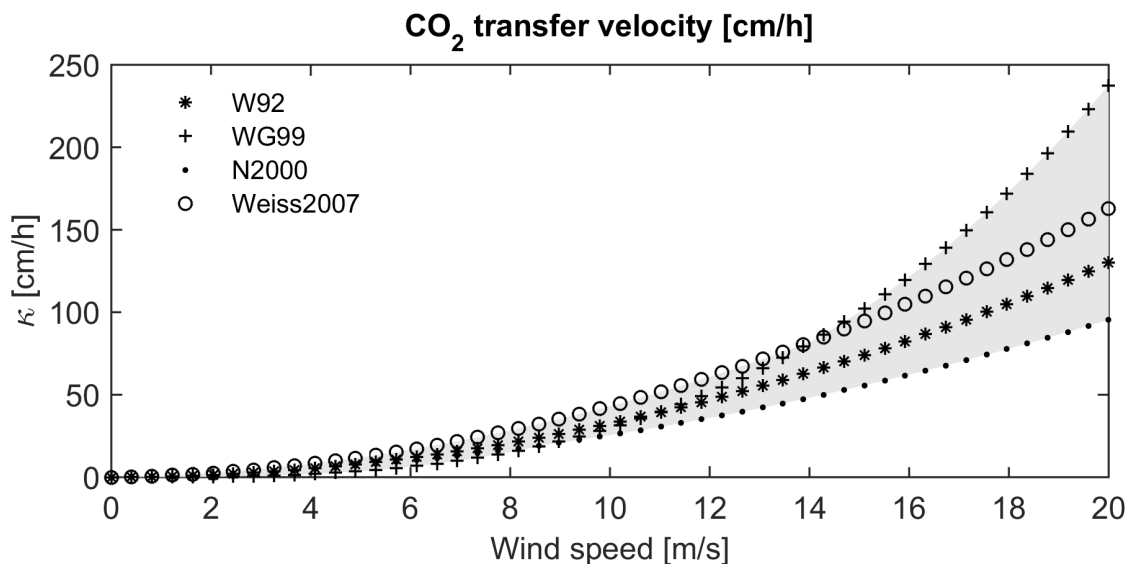


Figure 1.3: Wind based-gas transfer velocity parameterizations (shown in Table 2.1). They include the general relationships of [Wanninkhof \[1992\]](#) (star), [Wanninkhof and McGillis \[1999\]](#) (plus), [Nightingale et al. \[2000\]](#) (dot), and [Weiss et al. \[2007\]](#) (circle). The shaded area describes the deviation in the transfer velocity estimation from different formulations.

transfer velocity on the air-sea boundary layer processes that may not be accounted by using the wind-dependent parameterizations. The wind speed may be the dominant parameter in the air-sea interface, but is still not a sufficient descriptor of the factors mediating the gas transfer velocity [Weiss et al., 2007; Bock et al., 1999; Melville, 1996; Banner and Phillips, 1974].

In all wind-related parameterizations, the wind speed is used as the primary forcing factor of the gas transfer velocity across the air-sea interface based on the hypothesis that the wind controls air-sea gas exchange through the direct or indirect influence on surface waves and near surface turbulence. However, there are several other physical processes and physical properties mediating the transfer velocity across the air-sea interface such as surface films and wave breaking, which are more difficult to account for in wind speed parameterization.

Regardless of frequency, the energy contained in small-scale capillary waves is responsible for gas exchange. The small-scale waves influence the transfer rate through nonlinear interaction between wave motion and turbulence within the water, hence by dissipation of wave energy into turbulence. Furthermore, the small-scale waves can directly create velocity fluctuations on a scale small enough to affect the transfer rate [Hasse, 1980]. Moreover, these are the different impacts of surface films on short and long wind-generated surface waves, especially at low wind speed, which produce different results on gas transfer velocity rates over the same wind conditions [Zappa et al., 2004, 2001; Jähne et al., 1987].

Because of the strong dependence of the transfer velocity on small-scale turbulence and wave breaking, the surface roughness and the surface wind stress might be better proxies for gas transfer than the wind speed. If that would be true, a relation between surface roughness and the transfer velocity κ might be a better algorithm to estimate surface CO₂ transfer than the one dependent on only wind speed.

An effective way of estimating small-scale surface roughness is related to radar backscatter measurements from the sea surface. It appears plausible to test the usefulness of radar backscatter data to estimate surface CO₂ fluxes. Satellite radar instruments may provide enough data to attempt to relate the transfer velocity directly to the complex variety of processes on the ocean surface, including wave slope, atmospheric stratification, microscale breaking waves and the contribution of longer gravity waves which carry the short capillary waves. This can help to improve our understanding of the role of the ocean in the uptake of CO₂ and the scale of variability of the gas transfer rate between the ocean and atmosphere.

Attempts to relate air-sea CO₂ fluxes to radar backscatter data have been made before. In studies based on early altimeter data, the gas transfer velocity shows a correlation with the mean square slope regardless of the surface film concentrations or wave breaking [Goddijn-Murphy et al., 2013; Glover et al., 2007; Frew et al., 2007; Glover et al., 2002]. This conclu-

sion makes it feasible to use radar technology to infer the small scale ocean surface roughness and replace it with wind speed in gas transfer parameterizations.

The existing empirical relationships between radar backscatter and sea surface roughness derived from observations done by space-, air-, or ship-borne scatterometers, suffer from the limitation of spatiotemporal observations. This problem restricts the range of the wind, atmospheric, and sea state conditions and limits the usage of these empirical relationships [Long et al., 1999; Rufenach, 1995; Keller et al., 1989b; Donelan and Pierson, 1987; Keller et al., 1985]. Therefore, in an attempt to improve these relationships, in situ observations with better time resolution and smaller footprint area (better temporal resolution) are necessary.

In order to reach a better scatterometry-based estimation of gas transfer velocity, it is first necessary to have a better understanding about microwave scatterometry and the impact of sea surface roughness of different scales on radar backscatter. So far, however, there has been little discussion about the derivation of gas transfer velocity from scatterometry [Bogucki et al., 2010] and most of the approaches are from altimeter nadir viewing radar backscatter [Goddijn-Murphy et al., 2013; Frew et al., 2007; Glover et al., 2002]. However, there are still considerable uncertainties due to several factors which must be removed, such as 1) the lack of high-quality observations; temporal and spatial, 2) the uncertainty in the selected model, 3) the instrument measurements bias, and 4) the type of instrument for the purpose of the measurement.

1.2 Goals of the thesis

The objective is to investigate whether an improved algorithm for the air-sea CO₂ transfer velocity can be provided based on microwave scatterometer observations of the sea surface. In the first step, the performance of the new scatterometer for individual and combined radar arrangements will be evaluated. This will be done by testing the Multi³Scat observations against the scattering theory and C-band geophysical model function (CMOD5). In the second step, a test of the newly improved algorithm based on the observations available in the Baltic Sea will be made to verify if the algorithm leads to more accurate estimates than the previously available algorithms based on wind information alone.

To this end the thesis attempts to:

- test the newly available scatterometer data collected in the Western Baltic Sea with respect to their usefulness for air-sea CO₂ exchange studies;
- correlate the radar backscatter and CO₂ transfer velocity using observations in the Western Baltic Sea by considering wind stress as a proxy;

- develop a parameterization to better estimate CO₂ exchange across the air-sea interface, which can be further used for satellite scatterometer data;
- test the new algorithm against eddy correlation estimates and against traditional wind-based flux estimates.

1.3 Structure of the thesis

The remaining thesis consists of seven chapters:

In Chapter 2, the state of the art CO₂ fluxes estimation is discussed. An overview of the studies and achievements in the field of CO₂ fluxes and gas transfer velocity is given. The different methods to quantify the CO₂ flux and transfer velocity including observational methods and models are discussed.

Chapter 3 presents the state of the art microwave scatterometry including the theoretical background of ocean surface scatterometry, Bragg scattering theory, the interaction of the microwave pulses with the surface water and their behavior at different radar settings. This chapter reviews the relationship between the radar backscatter and environmental parameters and the available empirical parameterizations and models.

Chapter 4, provides the detailed descriptions of the Western Baltic Sea as the study area, FINO-2 platform, measurements campaign, the scatterometer used for the measurements and the auxiliary data collected at the platform. The technical information regarding the scatterometer and the data measured by the scatterometer, can be found in [Stammer \[2017\]](#).

Chapter 5, contains the statistical analysis of the new scatterometer data and explains the dependencies of the radar backscatter on environmental parameters at different scatterometer settings. The variation of the radar data with respect to the time due to the influence of the contribution of surface/interface parameters is discussed. The advantages of the combination of the radar observation settings (frequency, polarization, and incidence angle) to estimate the sea surface roughness scale are shown.

In Chapter 6, explores CO₂ flux observations using eddy covariance method in FINO-2. The new scatterometer-based gas transfer parameterization is introduced and compared with the traditional models. Mean square slope of the surface waves are computed using radar observation at different settings and correlates the radar backscatter to gas transfer velocity. The new algorithm to estimate gas transfer velocity and gas flux from radar data is introduced and verified.

Finally, an overview of the findings contained in this thesis with the main concluding remarks is given in Chapter 7, as well as recommendations for future work.

CHAPTER 2

State of the art surface CO₂ flux estimation

This chapter reviews the important parameters influencing gas exchange estimation, the existing uncertainties, and summary of the studies done to improve gas exchange estimation. We briefly discuss the most direct algorithms to estimate air-sea CO₂ flux and the available gas transfer parameterizations with the factors involved.

2.1 Air-sea CO₂ flux estimation

Questions about the deviation between measured and modeled gas exchange arose from the fact that measuring a very small fluctuation of CO₂ in presence of huge concentrations makes direct CO₂ flux measurements difficult [Jonsson et al., 2008]. Therefore using tracer gases such as SF₆ turn the experiments more simple. However, the difference in the timescale of CO₂ measurements with the eddy covariance system (EC-system) (order of the minutes) and SF₆ (order of the days) cause uncertainty. The timescale for SF₆ amendment is different from the timescale of wind speed change [Jonsson et al., 2008].

To model the air-sea exchange of CO₂, it is necessary to consider the biological and physical properties of the ocean as well as the meteorological conditions in the atmosphere. For the time-varying part, it might not be just the uncertainties in the transfer velocities but to some extent also variations in the partial pressure difference that cause problems. The partial pressure at the water surface is controlled by biological, chemical and physical processes in the ocean. To investigate the processes controlling the flux, the horizontal variation of water P_{CO₂} in the footprint area is important. The length of the footprint area depends on atmospheric stratification and water surface temperature and thus on the biological productivity; a very large footprint area for stable atmospheric condition makes the flux estimation more uncertain [Aubinet et al., 2012]. Horizontal variations of water P_{CO₂} can be large during the biologically active season, i.e., in spring and summer. It means that the CO₂ uptake during spring and summer is strongly controlled by the organic matter production that directly and strongly affects the partial pressure of CO₂ and may vary between individual years [Schnei-

der et al., 2014; Rutgersson et al., 2008; Weiss et al., 2007].

During autumn, when the productive season reduces P_{CO_2} , the water CO₂ concentration becomes under-saturated, higher wind deepens the mixed layer depth, which brings CO₂-enriched water from depth to the surface, and again increases the P_{CO_2} . The seasonality and interannual variation of P_{CO_2} through the investigation of different production periods in the Baltic Sea is explained by Schneider et al. [2014]. The seasonal variation of water P_{CO_2} can range from 150 [μatm] during the spring/summer up to the atmospheric level of the P_{CO_2} during autumn/winter. The annual increase in the atmospheric P_{CO_2} over the Baltic Sea was estimated to be up to 1.9 [μatm].

On shorter time-scales than seasonal changes, P_{CO_2} variations are subject to diurnal changes caused by the daily biological cycle and physical processes. The day to day variation of P_{CO_2} based on observation in the Baltic Sea is reported to be up to 40 [μatm] [Wesslander et al., 2011]. These variations were attributed to the combination of production/mineralization processes, mixing and, advection.

Weiss et al. [2007] evaluate the transfer velocity-wind speed relationship based on the CO₂ flux measurements by the eddy covariance system in the Baltic Sea. They show that the large scatter in the measured data is caused by the influence of other factors which affect sea surface roughness and near surface turbulence, thereby changing the gas transfer. The parameterization by Weiss et al. [2007] produces larger values than the other wind speed-gas transfer models, however, we will consider their parameterization in this study, as their experiments were conducted within our study area.

Recently, Takahashi et al. [2002] showed a large uncertainty in the global CO₂ uptake estimation as a consequence of different wind speed-gas transfer parameterizations. Along those lines, Yu et al. [2014] report the uncertainty in air-sea CO₂ flux caused by the different transfer velocity formulas. They concluded 6.41 [$PgCyear^{-1}$] maximum difference in the global monthly mean values for the air-sea CO₂ flux due to the different transfer velocity parameterizations. They presented the sea-state-dependent gas transfer parameterization based on the wave age, wave steepness, and significant wave height. The gas transfer velocity as a function of sea state results in a deviation about 150 cm/h between very young waves to fully developed wind waves, which correspond to the different wave steepness (wave steepness decreases when wave age increases)[Soloviev et al., 2007]. To date, however, there is still insufficient data to implement the influence of several important factors on gas transfer velocity estimation and to narrow the existing uncertainty.

Besides the fact that the single-forcing gas transfer velocity causes major uncertainty in the estimation of ocean CO₂ uptake rate, small biases of wind data can produce a much larger bias in the flux results. For instance, a global average wind speed of 6.6 m/s reported by

NCEP (National Center for Environmental Prediction) and the global averaged QuickSCAT satellite winds of 7.9 m/s , result in 43% biases in global CO₂ fluxes from quadratic dependencies and 71% from cubic relationships. Therefore, particular attention needs to be paid to the choice and quality of wind data used in CO₂ flux studies [Wanninkhof et al., 2009; Fangohr et al., 2008].

In this regard, our study attempts to develop an analysis which integrates the impact of several environmental forcing and physical process in the air-sea boundary layer to improve the gas transfer velocity estimation. In the next section, we discuss the most common methods to determine the air-sea CO₂ flux. Each method has advantages and limitations caused by technical difficulties, the spatial and temporal scale, accuracy and uncertainty.

2.2 Review of techniques to measure air-sea CO₂ flux

2.2.1 Direct flux measurement technique- Eddy covariance system

The most direct method to estimate fluxes is the eddy-covariance (EC) method which is commonly used at fixed-earth platforms. For observation on a moving platform, corrections due to the movement of the platform are necessary before using the EC method [Webb et al., 1980]. The eddy covariance method is based on the assumption that the net transport between the ocean and the atmosphere is one dimensional. In that case, the vertical flux density can be calculated based on the covariance between the turbulent fluctuation of the vertical wind and the quantity of interest. This quantity can be heat, mass and momentum [Aubinet et al., 2012].

To implement this method, the vertical wind is measured by a sonic wind anemometer, and an infrared gas analyzer measuring water vapor and carbon dioxide, in addition to the software packages for the eddy covariance method. This method is typically used in the surface boundary layer where the atmospheric turbulence is the dominant transport mechanism and supports the use of this method to measure the fluxes. This layer of the atmosphere is assumed to be a constant height turbulent flux layer [Aubinet et al., 2012]. With this assumption, it is possible to estimate the flux at the boundary between water and atmosphere based on the fluxes which are measured at any height in this lower layer of the atmosphere [Aubinet et al., 2012]. The CO₂ flux in this study is measured by the eddy covariance method. More detailed information about the instrumentation, observation, and data are discussed further in Section 4.3.4.

2.2.2 Bulk formulation

The bulk formulation (equation 1.1) simplified the determination of air-sea CO₂ flux using the measurements of solubility (from temperature and salinity), air and water CO₂ partial pressure and transfer velocity. The partial pressure of carbon dioxide is related to carbon dioxide concentration using $CO_2 = \alpha P_{CO_2}$ and the partial pressure difference of CO₂ is related to CO₂ concentration in the air using:

$$\Delta CO_2 = CO_{2,water} - \frac{CO_{2,air}}{H} = \alpha \Delta P_{CO_2,water} \quad (2.1)$$

where H is Henry's law parameter.

The effects of water temperature and salinity are considered in the solubility formulation based on the physical and molecular properties of the air, gas, and water. In principle, the movement of the gas molecules across the air-sea interface is due to diffusive transport which is influenced by the environmental variables. From the technical point of view, the bulk formulation is relatively easy and is a widely used method for the gas exchange estimation. However, this method is directly related to the gas transfer velocity estimation, which needs further exploration.

2.2.3 Remote sensing technique

Infrared imaging technique

Infrared imaging techniques are tools to quantify processes controlling air-sea gas exchange by using heat as a proxy tracer for gases to investigate the transport processes across the sea surface microlayer.

In this method, an infrared radiometer measures the sea surface temperature fluctuations and the characteristic timescale of the heat transfer process. The fluctuations of the sea surface temperature show the turbulent nature of the transport mechanism. The heat transfer coefficient is given by the molecular diffusive coefficient of the heat, D_{heat} , and the time scale of the transfer process.

$$\kappa_{heat} = \sqrt{\frac{D_{heat}}{time}} \quad (2.2)$$

The calculated heat transfer velocity can be extrapolated to the other gases such as CO₂ with the simple relationship considering that heat is a scalar, the same as for a dissolved gas tracer, and thus the convective transport velocity of both is equal and, only the molecular

transport differs. Therefore:

$$\frac{\kappa_{gas}}{\kappa_{heat}} = \left(\frac{D_{gas}}{D_{heat}}\right)^n = \left(\frac{Sc_{gas}}{Sc_{heat}}\right)^{-n} \quad (2.3)$$

where D is the molecular diffusivity of the gas and heat in water, Sc is the Schmidt number depending on the kinematic viscosity and molecular diffusivity (equation 1.3), and the parameter n depends on the surface roughness, which varies between $\frac{1}{2}$ and $\frac{2}{3}$.

The advantage of this method is that the heat flux can be sensed remotely from above the air-sea interface, and therefore very rapid changes in the transfer velocity on the time scale of less than one minute might be detected.

Satellite remote sensing technique

Recently, satellite remote-sensing data are used to parameterize various components of the equation 1.1. The radar data for air-sea gas flux estimation include sea surface temperature, surface salinity, sea surface roughness, wind speed, and direction. These data are used to determine the gas transfer velocity, κ , solubility, and P_{CO_2} [Fangohr et al., 2008].

As explained in Section 2.1, the short wind waves and near surface turbulence have a major influence on the air-sea gas exchange. Capillary-gravity waves and gas transfer velocity are small scale phenomena which relate to each other through viscosity and surface tension. The transmitted signal from an active sensor such as altimeter or scatterometer interacts with the ocean surface and returns back to the receiver of the instrument. The backscatter includes information about the sea surface roughness.

The altimeter is an active radar with a nadir-looking antenna emitting pulses toward the sea surface and works based on specular reflection theory to infer the sea surface roughness. Because of the short pulses interacting with the wave surface, the returned signal has a different shape from that of the transmitted one and therefore analyzing the wave spectrum of the returned signal infers the sea surface roughness. Glover et al. [2007] introduced an improved parameterization which relates gas transfer velocity and mean square surface wave slope using data from JASON-2 altimeter and then they compared their results with JASON-1 and TOPEX/Poseidon altimeter data. However, to isolate the specific wave lengths of interest for gas exchange estimation, their algorithms considered dual altimeter returns (in C- and Ku-bands) [Goddijn-Murphy et al., 2013; Glover et al., 2002]. In this regard, [Glover et al., 2002] describe an algorithm which results in a 16 cm/h error on the long term global averaged κ_{660} , as below:

$$\kappa_{660} = 7000 \left(\frac{0.38}{\sigma_{Ku}^0} - \frac{0.48}{\sigma_C^0 + 0.5} \right) \left(\frac{Sc}{660} \right)^{-0.5} \quad (2.4)$$

here σ^0 is the normalized Radar Cross Section (RCS) and subscript letters, C and Ku, correspond to C- and Ku-microwave frequency bands. Bogucki et al. [2010] proposed a preliminary estimation of the gas transfer velocity as a function of upwind radar cross section measured by the QuickSCAT scatterometer. The scatterometer is an active oblique-viewing radar (incidence angles $20^\circ < \theta < 70^\circ$), which works based on the Bragg scattering theory to estimate the sea surface roughness through the returned signal. The intensity of the scattering is related to the wavelength, slope, and amplitude of the surface waves. More details about the scatterometer will be presented further, as we will use scatterometer data for further analyses. Bogucki et al. [2010] introduced an algorithm to obtain estimates of oceanic uptake of CO₂ with an uncertainty of 7 cm/h. Their algorithm is evaluated applying limited data points (3 points) at limited wind speeds (approximately 6 m/s) to perform the regression, as below:

$$\begin{aligned} \kappa_{660} &= 10^{\frac{(\sigma_{0v}+47.4079)}{21.4248}} \\ \kappa_{660} &= 10^{\frac{(\sigma_{0h}+51.7545)}{22.5334}} \end{aligned} \quad (2.5)$$

2.3 Wind-based-CO₂ transfer velocity

By using CO₂ flux observations from the eddy covariance method, partial pressure difference of CO₂ and rearranging equation 1.1, it is possible to calculate the gas transfer velocity between the ocean and the atmosphere. In parallel, as mentioned in Section 2.1, several parameterizations link the gas transfer velocity to wind speed. In this study we apply several CO₂ transfer velocity- wind speed parameterizations which are shown in Table 2.1, owing to the fact that either their experiments were conducted within the same study area or their parameterizations are the most commonly used.

In order to compare the gas transfer velocity of different methods, the parameterizations are normalized with the Schmidt number. The Schmidt number, as a function of salinity and temperature, is given by Wanninkhof [1992] for fresh and oceanic waters.

$$Sc = A + B(SST) + C(SST)^2 + D(SST)^3 \quad (2.6)$$

The effect of salinity on Schmidt number is included by the coefficients, therefore, we applied linear interpolation to convert the coefficients to the salinity of the Western Baltic Sea which varies between 7 and 9 ppt. Here, A = 1954.3, B = 120.11, C = 3.4993, D =

Table 2.1: Wind-based gas transfer velocity parameterizations applied in this study.

Source	κ parameterizations
Weiss 2007	$\kappa = (0.46u_{10} + 0.365u_{10}^2)(Sc/660)^{(-1/2)}$
N 2000	$\kappa = (0.333u_{10} + 0.222u_{10}^2)(Sc/600)^{(-1/2)}$
WG 99	$\kappa = (0.0283u_{10}^3)(Sc/660)^{(-1/2)}$
W 92	$\kappa = (0.31u_{10}^2)(Sc/660)^{(-1/2)}$

Weiss2007: [Weiss et al. \[2007\]](#), N2000: [Nightingale et al. \[2000\]](#), WG99: [Wanninkhof and McGillis \[1999\]](#), W92: [Wanninkhof \[1992\]](#), Sc: Schmidt number [Wanninkhof \[1992\]](#) (depends on salinity and temperature).

0.0418, and SST is the water surface temperature in degrees Celsius.

The comparison between gas transfer parameterizations listed in Table 2.1 are shown previously in Figure 1.3. The parameterization proposed by [Weiss et al. \[2007\]](#) obtained from observations in the Baltic Sea (near Arkona Basin), which is close to the area of this study. They fit their measured data (wind speed and gas transfer velocity) to a combination of quadratic and linear wind speed dependencies with a correlation factor of 0.81. According to this parameterization, the gas transfer velocity reach 150 *cm/h* for a wind speed of 20 *m/s*. [Nightingale et al. \[2000\]](#) performed experiments in fetch-limited environments and introduce a 100 *cm/h* gas transfer velocity for 20 *m/s* wind speed.

CHAPTER 3

State of the Art Sea Surface Scatterometry

This chapter, outlines the principles of ocean scatterometry and explains the physical mechanisms ruling microwave scattering from the ocean surface. To implement this application and in order to exploit the ocean variables of our interest (e.g., wind speed, mean square surface slope, air and water surface temperature), it is necessary to have a clear picture of the physical processes involved in the interaction of electromagnetic and oceanic waves.

3.1 Microwave interaction with the sea surface

In the category of active remote sensing, the scatterometer is a type of radar designed to transmit short microwave pulses to the earth's surface to determine the radar cross section of the surface based on the energy reflected from the sea surface. Microwaves do not penetrate far into the water body (eg. about 2 mm depth at 10 GHz) therefore, a microwave instrument provides us information on air-sea interface based on sea surface characteristics. A simplified view of a specular reflection and microwave scattering is shown in the Figure 3.1.

From Figure 3.1 (left panel), a scatterometer is transmitting beams towards the calm sea surface. The microwave pulses interact with the sea surface. The reflected beam follows the specular reflection theory, with a reflection angle equal to the incidence angle on the opposite side. In the right panel of Figure 3.1, the sea surface is rough, which results in strong backscatter towards the radar with almost no specular reflection. This simple illustration gives us the idea that for an oblique viewing instrument such as a scatterometer, the intensity of the backscatter increases in the presence of higher sea surface roughness [Robinson, 2004; Valenzuela, 1978].

The radar equation characterizes the proportion of the radar energy transmitted (E_t) to and reflected (E_r) from a unit area of the sea surface in the direction of incidence. For an individual target in the radar beam illumination area, the radar cross section (σ), with the units of area, is described as the measure of a target's ability to reflect radar signals in the

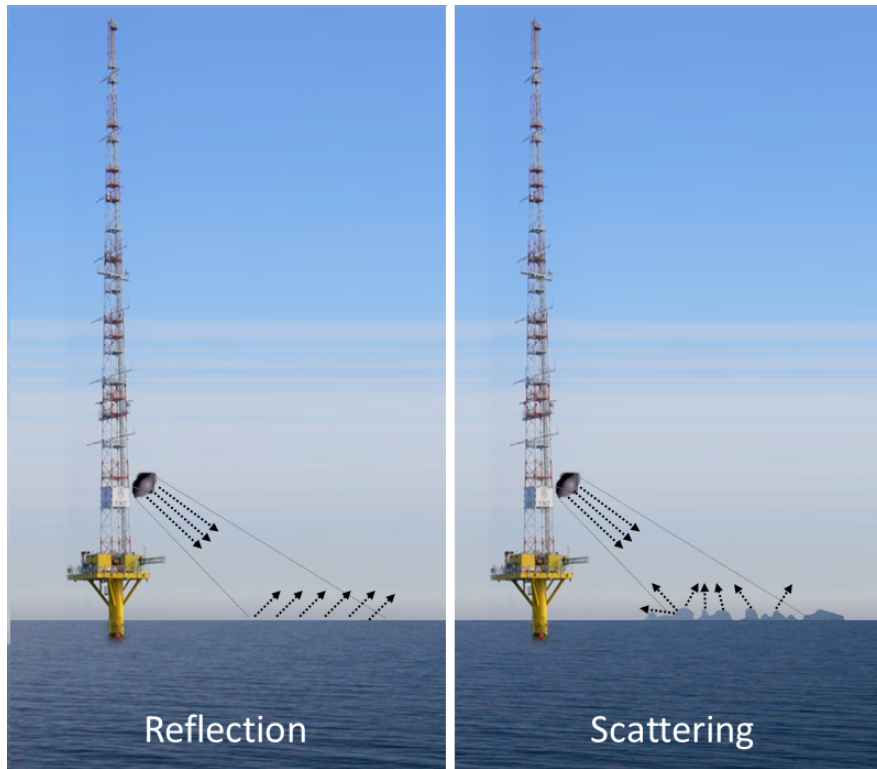


Figure 3.1: The scheme of a specular reflection from a calm sea surface (left) and microwave scattering from a rough surface (right). Here, the microwave scatterometer is fixed at a platform, transmitting and receiving the signals via one antenna.

direction of the radar receiver (see equation 3.1).

$$\sigma = \frac{E_r}{E_t} \cdot \frac{(4\pi)^3 r^4}{G^2 (\lambda_r)^2} \quad (3.1)$$

Here, G denotes the antenna gain, r is the object's distance from the antenna and λ_r is the microwave wavelength. In principle, for each radar backscatter, the cross section is a unique value of backscattering from a specific number of scattering elements over a limited area on the sea surface. However, the radar backscatter of the area scattering consists of all individual backscatter which is computed using the ensemble averaged of the contribution of the radar beams. Therefore, the final electric field detected by the receiver can be considered to be a vector composed of the averaged of the instantaneous electric fields from each radar beam, dependent on their individual phases and traveling distances. Finally, the radar cross section will be normalized to the illumination area of size A and produces a dimensionless variable which is called normalized radar cross section and is denoted by $\sigma_0 = \langle \frac{\sigma}{\delta A} \rangle$ [Robinson, 2004; Ulaby et al., 1982]. σ_0 is normally expressed in a decibel scale $10 \log_{10}(\sigma_0)$.

Based on experimental data and scattering theory, a significant number of empirical and

theoretical backscatter models and algorithms for estimation of sea surface characteristics have been developed. For rest of this chapter, we will study some of these models and algorithms.

3.2 Bragg scattering

The scattering process at intermediate incidence angles, $20^\circ < \theta < 70^\circ$ (θ is the angle between the transmitted beam and the direction perpendicular to the surface) can follow the Bragg mechanism when

$$\lambda_{radar} = 2 \lambda_{water} \sin(\theta) \quad (3.2)$$

Here, λ denotes wavelength and θ is the incidence angle. At intermediate incidence angles, for a signal transmitting into the sea surface, constructive interference occurs when the surface wavelengths are in resonance with the microwave wavelengths. In Bragg scattering theory, if the transmitted electromagnetic wavelength reaches these particular surface wavelengths, the backscatter signal is the highest [Robinson, 2004]. This implies that the surface waves with wavelengths comparable to the radar wavelengths influence radar backscatter. Therefore, for the scatterometer in the microwave band, these waves are on the scale of centimeters, and are thus short gravity-capillary waves which have the same scale as gas transfer velocity. Table 3.1 summarizes the value of the scatterometer wavelengths and incidence angles used in this study and consequently calculated wavelengths according to Bragg scattering theory.

Table 3.1: The scale of the waves that influence radar backscatter. The water wavelengths are calculated from equation 3.2 according to Bragg scattering theory.

Radar bands	L	S	C	X	Ku	
Frequency [GHz]	1.0	2.4	5.3	10.0	15.0	
Wavelength [cm]	30.0	12.5	5.7	3.0	2.0	
Bragg wavelength [cm]	35°	26.2	10.9	5.0	2.6	1.7
	45°	21.2	8.8	4.0	2.1	1.4
	55°	18.3	7.6	3.5	1.8	1.2

In Table 3.1, the different wavelengths for each combination of the radar wavelength and the incidence angle are noted. According to the Bragg scattering mechanism, the waves of shorter wavelengths are in resonance with the radar wavelength at shallower incidence angles. These shorter wavelengths have less spectral distribution of ocean wave energy. There-

fore, more oblique viewing will sample shorter and smaller amplitude Bragg waves, which lead to lower backscatter [Robinson, 2004]. Figure 3.2 describes the scattering mechanism from the sea surface in three different regions; a) at low incidence angles ($\theta < 20^\circ$) where specular reflection is the dominant process, b) at intermediate incidence angles ($20^\circ - 70^\circ$) where the Bragg scattering mechanism is dominant, and c) at grazing incidence angles ($\theta > 70^\circ$) where the waves with larger crests produce a shadowing effect. In this figure, we see the strong radar backscatter caused by specular reflection at small incidence angle for a smooth surface, but with increasing incidence angle, the radar backscatter falls off quickly because the signal bounces off the surface in a direction away from the radar. For a rough surface, at incidence angles less than 20° , the radar backscatter is lower than from a smooth surface at the same angle because a lot of energy is scattered in many directions. At an incidence angle more than 20° a rough surface still produces a lot of random scatter, but the radar backscatter is more than that of the smooth surface at the same angle.

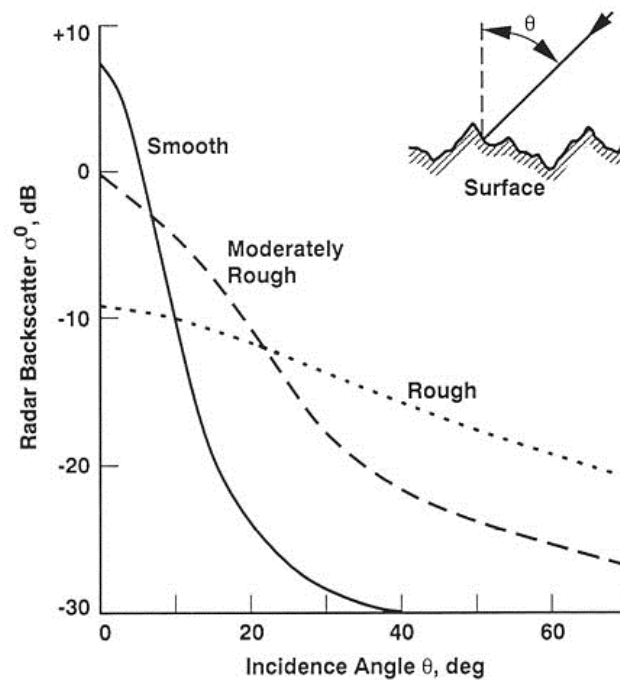


Figure 3.2: Angular variation of radar backscatter for different sea states [Robinson, 2004]. The smooth surface at steep incidence angles follows the specular reflection so that radar backscatter is low. For the rough surface, a lot of energy is scattered in many directions but at shallower incidence angles; the reflected energy is more than that of the smooth surface at the same angle, which produces higher radar backscatter.

3.2.1 Bragg scattering model

The Bragg scattering model uses the radar integral equation to explain the normalized radar cross section for either polarization with Equation 3.3 [Valenzuela, 1978; Wright, 1968].

$$\sigma_B = 16\pi(k_r^4)\cos(\theta)^4|g_p(\theta)|^2\psi(2k_B\sin(\theta),0) \quad (3.3)$$

$\psi(k_x, k_y)$ is the two directional wavenumber spectrum of surface displacement, g_p is the first order scattering coefficient depending on the incidence angle and the dielectric constant of the sea water, and is sensitive to polarization [Plant, 1990; Valenzuela, 1978]. The dimensional spectrum of the surface displacement is including the contribution of the surface waves which are in resonance with the radar wavelength and travelling toward and/or away from the antenna look direction. This term covers only the component of surface wave spectrum specified by Bragg resonance. Plant [1990] describes the angular variation of the Bragg scattering geometric coefficients and compared the coefficients of vertical and horizontal polarizations at 10 GHz radar frequency. His result shows larger coefficients for vertically polarized signals than that of horizontally polarized signals which further cause differences between vertical and horizontal polarization radar backscatter.

The polarization of an electromagnetic wave indicates the direction of the electrical field vector with respect to the plane of incidence. The polarization is horizontal if the electrical field is perpendicular to the plane of incidence and vice versa for vertically polarized signals. The conductive and dielectric properties of sea water can produce different polarization values of radar backscatter [Barale and Gade, 2008; Plant, 1990; Valenzuela, 1978]. As shown in Figure 3.3, this difference is considerable at intermediate incidence angles (Bragg regions, $20^\circ < \theta < 70^\circ$), and enhanced with increasing the incidence angle from 30° to 70° [Barale and Gade, 2008].

For the specular scattering ($\theta < 20^\circ$), there are no differences between horizontal and vertical scattering. At large incidence angles (over 70°), the effect of shadowing reduces radar backscatter. The primary condition for the validity of the Bragg scattering model is Bragg scattering from short gravity wave components. Therefore, when first order Bragg scattering is the dominant contribution to the return signal, radar cross section variation to the wind reflects the spectral density of the particular wavenumber which only considers the short capillary waves. The validity of the Bragg scattering model in the microwave band is confirmed in laboratory experiments by Plant and Wright [1977] and Wright [1968] and with wind generated waves by Plant [1990].

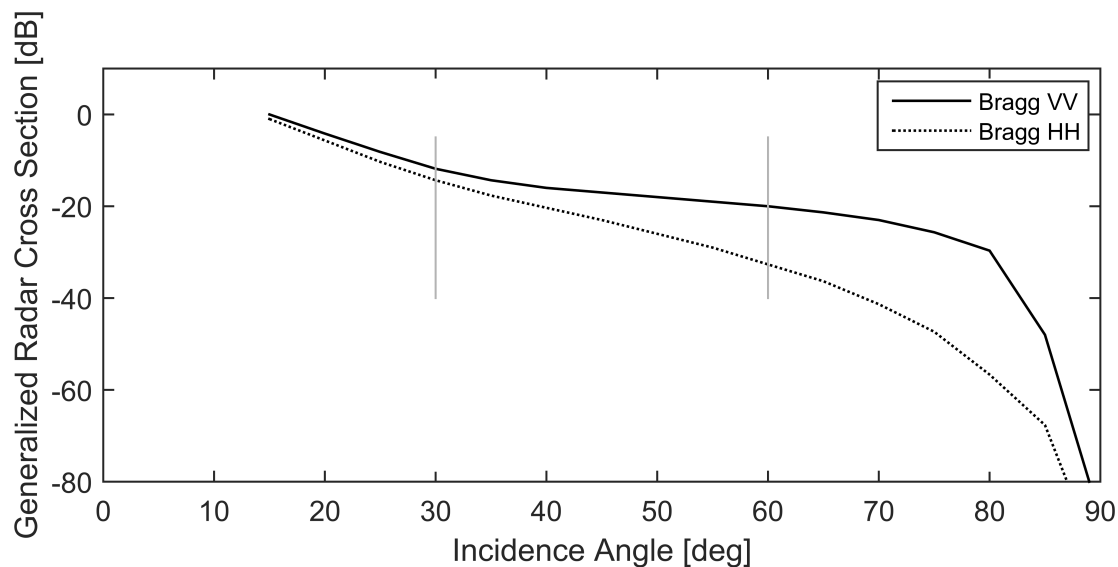


Figure 3.3: Angular dependence of radar backscatter at vertical (solid) and horizontal (dashed) polarizations. The gray vertical lines indicate the region of our measurements. Figure is adapted from [Barale and Gade, 2008].

3.3 Composite surface model

The Bragg scattering model is subject to a small amplitude limitation on surface perturbations, therefore it's wave spectrum only considers the short scale waves [Valenzuela, 1978; Wright, 1968]. However, the realistic ocean surface consists of long gravity waves which carry short capillary waves. The two surfaces are statistically independent in most cases. Therefore, the height and slope of the combination of the two waves are distributed based on the spectrum of the longer waves. Valenzuela [1978] and Wright [1968] showed that, the wave spectrum is divided into two regions, the short wavelength by Bragg model and the longer waves which carry the shorter waves. They showed the velocities of the shorter waves which ride on the longer waves are based on the velocity of the combination of both waves. In this respect, a composite-surface model (or two-scale model) describes the surface as individual small surfaces and applies the Bragg model to each of these surfaces. Then the small amplitude assumption is reasonable for each small surface. The total radar backscatter is the sum of the scattering from all these small surfaces and the wave spectrum is including both distinct regions, the short wavelengths based on the Bragg model, and the long underlying waves [Valenzuela, 1978; Wright, 1968].

3.4 Non-Bragg scattering

Kudryavtsev et al. [2003] describe a model based on the statistical description of the wave fronts proposed by Phillips [1988]. They suggest that the total radar cross section consists of a pure Bragg term, the non-Bragg contribution of breaking waves, and the contribution of specular reflection. We neglect the contribution of specular reflection, because at the incidence angles $20^\circ < \theta < 70^\circ$ (the range of the angles in our study), this term is very small. They suggest that for short waves at high frequencies the spectral level is mainly determined by breaking waves effects. The contribution of wave breaking is independent of the mechanism responsible for backscattering, regarding scattering from specular reflection, wedge scattering, or scattering from wave breaking. The radar cross section of the sea surface and the expression related to the contribution of non-Bragg scattering is given by Equation 3.4.

$$\begin{aligned}\sigma_0^{PP} &= \sigma_B^{PP} + \sigma_{br} \\ \psi(k) &= 10^{-2} |\cos\phi|^{\frac{1}{2}} u_* g^{-\frac{1}{2}} k_r^{-\frac{7}{2}} \\ \sigma_{br} &= G(\theta, \phi) \left(\frac{u_*^2 k_r}{g}\right)^{\frac{3}{2}}\end{aligned}\tag{3.4}$$

where, σ_{br} corresponds to the contribution of breaking waves which is polarization independent, $G(\theta, \phi)$ is a function of incidence angle (θ) and azimuth direction (ϕ) (the direction of radar viewing relative to the wind direction). The primary condition for the validity of the non-Bragg contribution is that the radar wavelength is significantly small compared with the scale height of the largest breaking waves. Kudryavtsev et al. [2003] improve the non-Bragg scattering expression proposed by Phillips [1988] and indicate the explicit azimuthal dependence of the non-Bragg scattering to the total radar cross section, which is maximal in the upwind direction (direction of the wind towards the antenna) and is minimal in the downwind direction of radar observations. Their study indicates the significance of the non-Bragg scattering in the total radar backscatter which results in better agreement with observations over various scatterometer settings based on some hypothesis to simplify the NRCS model, such as, a) only breakers with scales exceeding the radar wavelength can contribute to increased radar returns; b) a cut-off wave number k_{nb} is fixed to compute backscattering.

The significant contribution of a non-Bragg scattering mechanism which is polarization independent (according to equation 3.4) could possibly be shown by the polarization ratio (PR). When the contribution of non-Bragg scattering in total RCS is dominant ($\sigma_B^{PP} \ll \sigma_{br}$), then PR is close to 1 in the linear unit and close to zero in the logarithmic unit. When the contribution of pure Bragg scattering is dominant in total RCS ($\sigma_B^{PP} \gg \sigma_{br}$) then PR is

large. The polarization ratio can be described as Equation 3.5:

$$PR = \frac{\sigma_0^{vv}}{\sigma_0^{hh}} = \frac{\sigma_B^{vv} + \sigma_{br}}{\sigma_B^{hh} + \sigma_{br}} \quad (3.5)$$

A polarization ratio close to unity (in linear scale) at intermediate incidence angles represents the enhanced roughness caused by the steep forward face of the breaking waves and results from the incoherent backscattering from small scale roughness generated by breaking crest.

3.5 Geophysical model function

3.5.1 Empirical relationship

One major characteristic of the scatterometer is the capability of inferring the wind speed and direction near the sea surface. The technique is based on the sensitivity of the microwave radar backscatter to the short scale surface waves, which are mainly forced by the surface wind. To infer the wind direction, the radar backscatter is sensitive to the azimuth angle relative to the upwind direction due to its sensitivity to the surface wave direction, which is mainly controlled by the surface wind.

In this respect, wind retrieval from microwave radar backscatter as a nonlinear inversion process, based on accurate knowledge of the Geophysical Model Function (GMF) (in the empirical form), relates the radar backscatter to the wind vector. In empirical form, the radar cross section depends on the frequency, polarization, incidence angle of the microwave signal, and on wind speed and azimuth direction [Robinson, 2004; Wentz et al., 1984; Jones and Schroeder, 1978]. The relationship between σ_0 and wind vector, for a given frequency, polarization and incidence angle is explained below:

$$\sigma_0 = aU^b[A_0 + A_1 \cos\phi + A_2 \cos 2\phi] \quad (3.6)$$

Here, ϕ is the azimuth direction of the wind, coefficient A_0 is the steady state term that accounts for major wind speed effects, A_1 is the fundamental term for upwind-downwind anisotropy in which the term $A_1 \cos\phi$ represents a modulation that is maximum in upwind ($\phi = 0^\circ$) and minimum in downwind ($\phi = 180^\circ$) directions, and A_2 is the second harmonic for upwind-crosswind anisotropy which represents the largest modulation of radar cross section as a function of wind direction, which is maximum in upwind and downwind directions and minimum in crosswind direction ($\phi = 90^\circ$). The size of the higher order harmonics to

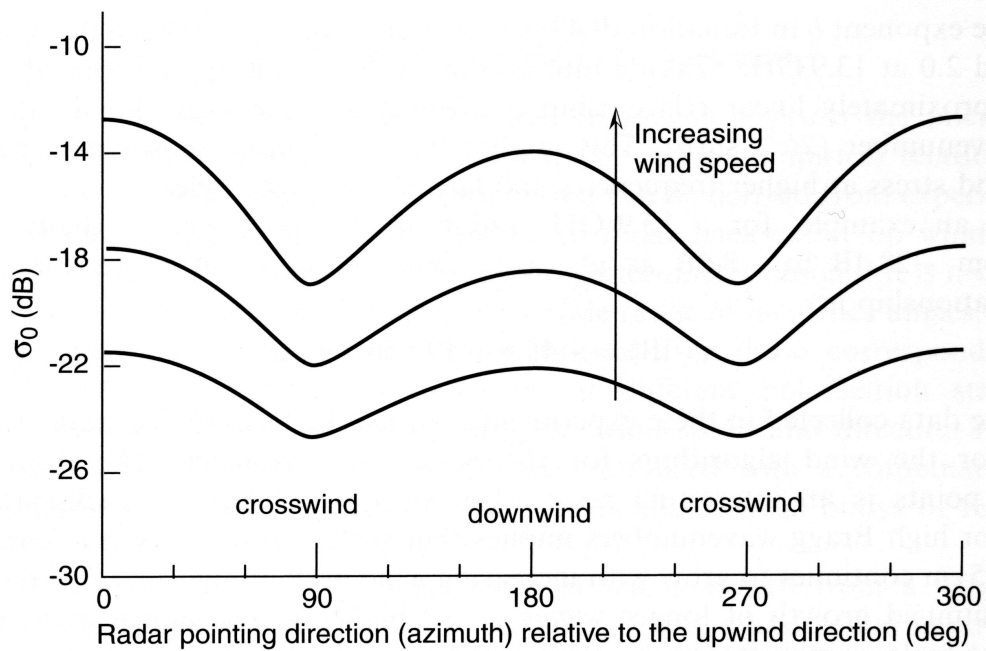


Figure 3.4: The variation of σ_0 with the direction of the radar azimuth relative to the upwind direction at different wind scales. Figure describes radar cross section at 13.9 GHz and 40° incidence angle [Robinson, 2004].

the directional dependence is small enough to shorten the series to 2ϕ [Wentz et al., 1984]. Figure 3.4 shows the anisotropy of σ_0 according to the empirical model. For a specific wind direction, Equation 3.6 comes to the simple form of $\sigma_0 = aU^b$, with a as the scaling coefficient and b as the wind speed exponent, which is a function of radar frequency (f), polarization (pp), and incidence angle (θ), and reflects the sensitivity of RCS to wind speed changes.

3.5.2 C-band model function

The interpretation of the sea surface roughness scale retrieved from the scatterometer sea surface backscatter is aided by using the output from a geophysical model function. Considering the fact that, for practical use, the relationship between radar backscatter from the sea surface and wind rely on empirical models, C-band models (eg. CMOD) describe an empirical function to retrieve the wind from radar backscatter with less possible biases than other methods (eg., empirical relationship and first order Bragg model). The geophysical model function for C-band and vertical polarization is developed by using European Center for Medium-Range Weather Forecasts (ECMWF) and European Remote Sensing Satellite (ERS-1) data. These CMOD models are based on collocation studies between scatterometer

data with in situ data or model fields. The wind biases between satellite data inverted by CMOD4 and field observations, especially at high wind speeds ($> 20 \text{ m/s}$), was a reason to update the model function. In this regard, CMOD5 attempts to reduce the overestimation caused by upwind-downwind asymmetry by multiplying the corresponding term in CMOD4 by an attenuation factor that depends on wind speed and incidence angle, but no correction is considered for the upwind-crosswind term [Hersbach et al., 2007]. Furthermore, we will use CMOD5 model function to compare the radar cross section calculated using GMF and our observations in the Baltic Sea. The major parts of the CMOD5 model function is described here with the formulation (3.7):

$$\sigma_0 = b_0 (1 + b_1 \cos\varphi + b_2 (2 \cos\varphi^2 - 1))^{1.6} \quad (3.7)$$

$$b_0 = f(a_2 u, s_0)^\gamma \times 10^{(a_0 + a_1 u)}$$

$$f(s, s_0) = \begin{cases} (\frac{s}{s_0})^\alpha g(s_0), & s < s_0 \\ g(s), & s \geq s_0 \end{cases}$$

$$g(s) = 1/(1 + \exp(-s)), \quad \alpha = x_0(1 - g(s_0))$$

$$b_1 = \frac{c_{14}(1+x) - c_{15}u(0.5+x - \tanh[4(x+c_{16}+c_{17}u)])}{1 + \exp[0.34(u-c_{18})]}$$

$$b_2 = (d_2 u_2 - d_1) \exp(-u_2)$$

$$u_2 = \begin{cases} a + b(y-1)^n, & y < y_0 \\ y, & y \geq y_0 \end{cases}$$

$$y = \frac{u + u_0}{u_0}$$

$$y_0 = c_{19}, \quad n = c_{20},$$

$$a = y_0 - (y_0 - 1)/n, \quad b = 1/[n(y_0 - 1)^{n-1}]$$

The parameters u_0 , d_1 , and d_2 are functions of incidence angle. More details, and a complete version of the model function with the coefficients, are presented by [Hersbach \[2003\]](#). Figure 3.5 shows the incidence angle dependence of the NRCS results from the CMOD5 model described above. The input data, including wind speed, wind direction, azimuth direction, and incidence angle, are collected for the purpose of this study. The detailed description of the data set will be explained in Chapter 4. Figure 3.5 represents the NRCS at different wind scales (low wind and high wind) and different wind directions (upwind and downwind). As shown in the figure, the NRCS from the model varies with changes in incidence angle. Also, the NRCS shows a clear dependence to the wind speed. However, the bias between upwind and downwind directions is less than 1 dB and is the same at different incidence angles. We will consider the results of the CMOD5 model to test observations used in our study.

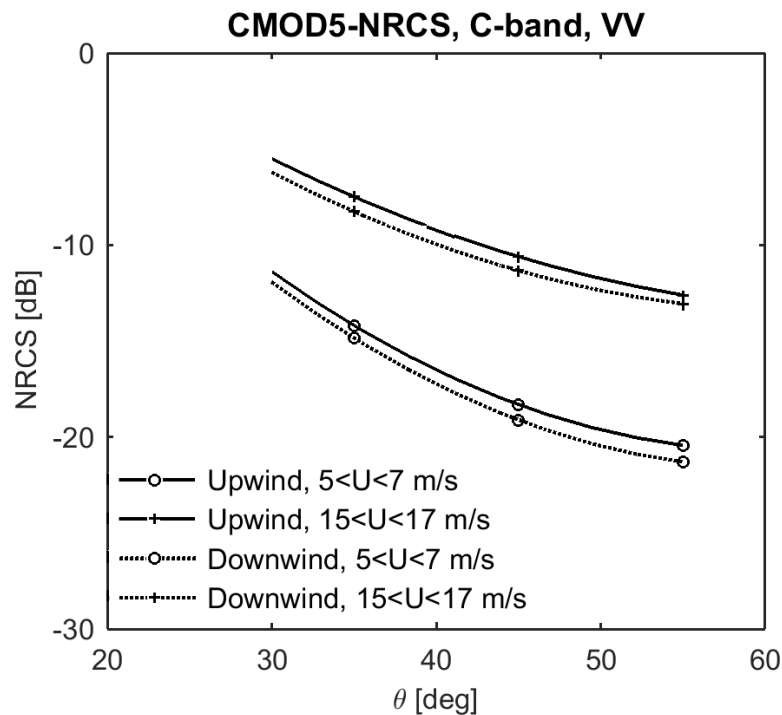


Figure 3.5: The NRCS from CMOD5 model (C-band, VV polarization) as a function of incidence angle. The curves show NRCS at different wind scales; high wind (plus) and low wind (circle), and for different wind directions; upwind (solid lines) and downwind (dashed lines). The calculated NRCS are based on the input data measured for the purpose of this study, including wind speed, wind direction, azimuth direction, and incidence angle.

CHAPTER 4

Experiment and Methodology

In this chapter, the study area, the scatterometer, measurements campaign, and the auxiliary data used in our study will be described. To study the long-term variation of the mean radar backscatter, a tower-based scatterometry provides the quantitative data at the wide range of environmental conditions with the advantage of very small footprint and better time resolution compared to that of the spaceborne scatterometer. A comprehensive data set from the tower-mounted microwave scatterometer allows us to extract useful information of sea surface roughness from radar backscatter which leads to better gas transfer estimation from scatterometer observations.

4.1 Study area-Western Baltic Sea

The marine area investigated in this study is the western Baltic Sea. The Baltic Sea is a semi-enclosed continental shelf sea area, located in northeast Europe. The exchange of water to the open ocean is limited and due to a positive fresh water balance, the Baltic Sea water is slightly salty with a mean salinity about 7 ppt. The salinity stratification varies horizontally, being higher west and south and lower north and east. The salinity of the western Baltic Sea varies between 7-9 ppt. Since about 2000 years salinity in Baltic Sea has been close to the present level [Leppäranta and Myrberg, 2009].

The Baltic Sea is a shallow basin with a mean depth of 54 meters which limits the vertical convection. Figure 4.1 shows the bathymetry of the Western Baltic Sea using the "iowtopo2" data at a resolution of 1 minute of latitude and 2 minutes of longitude ¹ [Seifert et al., 2001]. Monthly averaged precipitation in Baltic Sea is about 20 mm to 100 mm depending on the seasons. The largest monthly precipitation reaches in late summer and in autumn while the smallest values are observed in winter and spring [Leppäranta and Myrberg, 2009].

The wind direction in the Baltic region is dominated by westerly winds. Stronger wind

¹The bathymetry data source; www.io-warnemuende.de/iowtopo

from October to February and weaker wind from April to June are observed in Western Baltic Sea (see Section 4.3 and [Weiss et al., 2007]). Mean wind speed is about 6 m/s, the highest wind speed ever recorded for Baltic Sea is about 30 m/s and the wind speed higher than 17 m/s occurs less than 5%. More than 50% of the winds are between 5 m/s to 9 m/s and less than 15% of the winds are below 3 m/s. The horizontal currents in Western Baltic Sea are weak about 10 cm/s and vertical velocities are less than 0.1 mm/s.

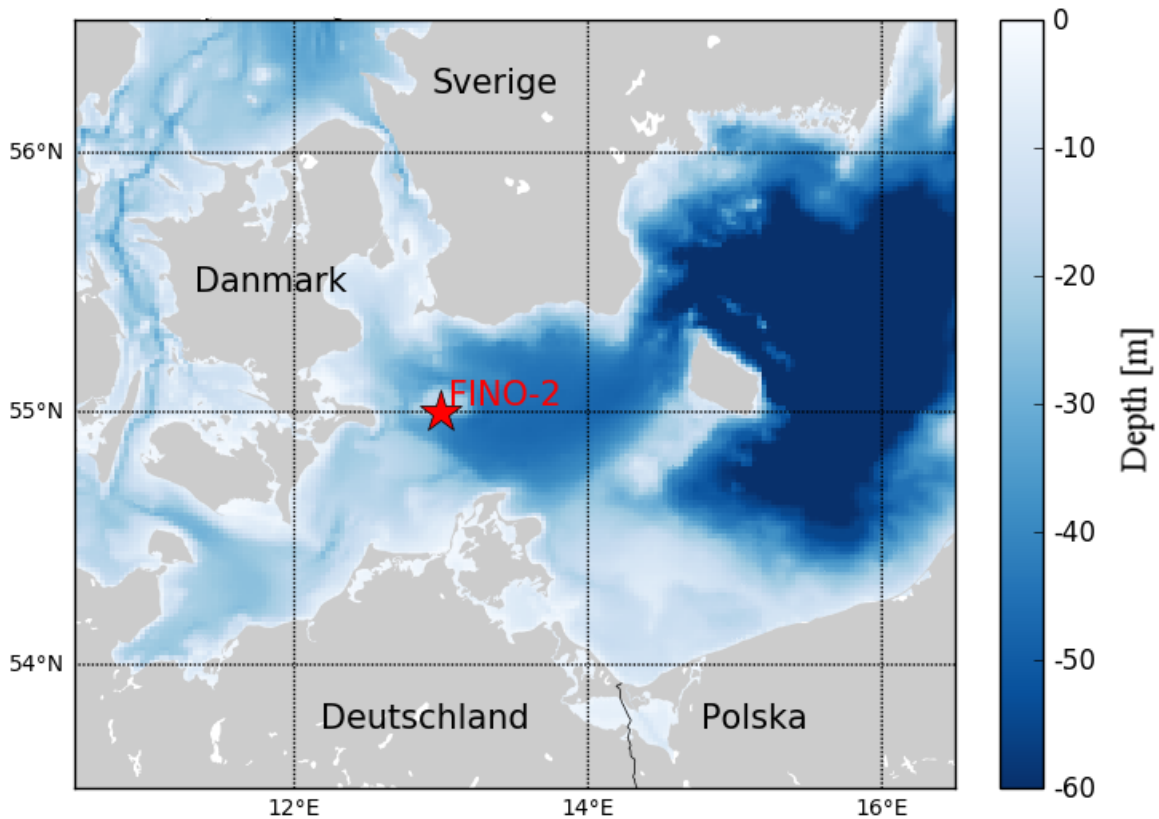


Figure 4.1: The bathymetry map of the Western Baltic Sea, located in Northern Europe (from 11°E to 16°E and from 53.5°N to 57°N) and connected to the North Sea. The data source: Baltic Sea topography 1 minute of latitude and 2 minutes of longitude (iowtopo2).

The surface current speed is 2-3% of the wind speed and direction is 20-30° to the right of the wind direction (based on the Ekman theory at the surface) and during the storm, the current speed may reach 50 cm/s.

Wind generated waves in Western Baltic Sea are subject to deep-water theory. The growth of waves is limited by the duration of wind events and fetch and therefore, wave periods are relatively short, about 7 to 8 seconds except during the strong storms, thus long period waves such as swell are rare in this region. So that, the longest wind generated waves follow the deep water approach; $H > \frac{1}{2}\lambda$. Here, H is the depth and λ is the wavelength.

Studies by [Rutgersson et al. \[2009\]](#) show a larger seasonal amplitude of atmospheric concentrations of CO₂ in the Baltic region rather than at Mauna Loa, Hawaii, which is referred to as a global reference for the atmospheric CO₂ background. According to the climate change scenarios (IPCC AR4) and BACC team (Baltex Assessment of Climate Change, 2008), the atmospheric temperature in Baltic Sea region will increase during the next 100 years which lead to a warmer Baltic Sea with consequence for the annual cycle of hydrography, circulation, ice seasons and ecological state. These details require for further research about the anthropogenic greenhouse gases such as CO₂ in the Baltic Sea region. For this purpose, our study follows a case-study design, with the data being gathered in the Western Baltic Sea, attempts to better estimate air-sea gas exchange rate using microwave scatterometer. The next section will describe the instrumentation and auxiliary data used in this study.

4.2 Instrumentation

4.2.1 The scatterometer Multi³Scat

The Multi³Scat (*M³S*) is a Doppler scatterometer, operated by Institute of Oceanography, University of Hamburg. The subscript three is an indication for multi purposes, multi-frequency and multi-polarization. Multipurpose because of different operational purpose, for example, it can be mounted on a Helicopter for measurements of ice cover thickness or surface films [[Kern et al., 2009](#)]. The system comprises a microwave unit, a control unit, a direct digital synthesizer (DDS) module and a data storage unit. [Stammer \[2017\]](#) describes in detail the instrumental set-up, the measurement campaigns, as well as data processing. The Multi³Scat measured radar cross section (RCS) at five microwave bands (1.0 GHz, 2.3 GHz, 5.3 GHz, 10.0 GHz, and 15.0 GHz; corresponding to L, S, C, X, and *K_u* band, respectively), four polarization combinations (HH, HV, VV, VH; the first and second letter denoting the polarization of the transmitted and the received signal, respectively) and three incidence angles (35°, 45°, 55°). [Figure 4.2](#) shows an overview of the scatterometer components and processes for transmitting and receiving a signal at various scatterometer settings.

A long term in situ measurements was conducted with about 5 minutes interval for 27 months from September 2011 to November 2013 to obtain the backscatter of the ocean surface. Considering the westerly as dominant wind direction in the area of the measurements, the Multi³Scat antenna is aligned toward the west. [Figure 4.3](#) shows the side view of the scatterometer parabolic antenna.

The incidence angles of the Multi³Scat antenna are changed by a small motor from 35° to 55° with a 10° interval during each observation cycle. The theoretical footprint of a

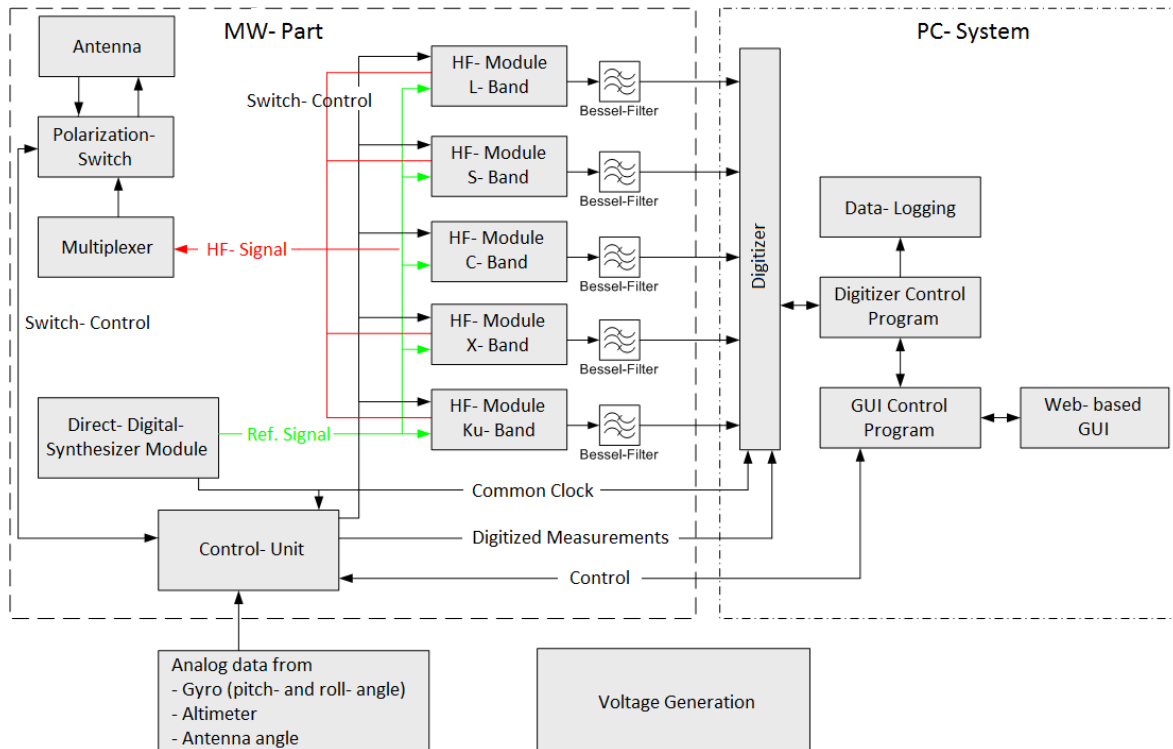


Figure 4.2: The overview of the scatterometer components (Microwave part and PC system). Adapted from the Multi³Scat technical documentation.

parabolic antenna on a surface normal to the direction of its transmission beam is typically circular in shape. The effect of the footprint area on the total averaged radar backscatter

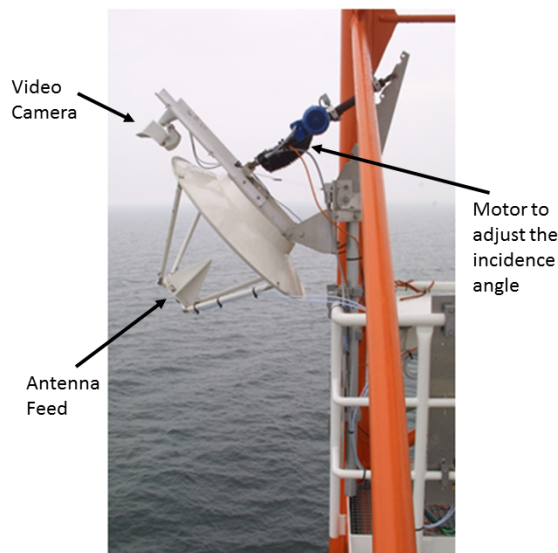


Figure 4.3: The side view of the Multi³Scat antenna on FINO-2 platform, (Pictured by Mayk Fischer). The antenna diameter is 96 centimeters.

of each sampling interval (see Section 3.1), depends on the transmitter power, the receiver sensitivity, and the beam width of the antenna gain pattern and varies considerably at different microwave frequencies (depends on the wavelength of the electromagnetic signal) and incidence angles (see Table 4.1). For a specific wavelength of the electromagnetic signal, the flatter the incidence angle, the larger the field of view, resulting an averaged backscatter power over a larger surface area of different roughness scales and therefore different radar intensity [Ulaby et al., 1982]. The technical overview of the Multi³Scat is summarized in Table 4.1.

Table 4.1: Technical overview of the Multi³Scat instrument. Table explains the frequency, wavelength, antenna gain, and beam width for each particular microwave band.

Type	Doppler scatterometer					
Antenna	Dual polarized parabolic antenna					
Microwave bands	L	S	C	X	Ku	
Frequency [GHz]	1.0	2.4	5.3	10.0	15.0	
Wavelength [cm]	30.0	12.5	5.7	3.0	2.0	
Gain [dBi]	14	22	28	33	35	
3dB Beamwidth [°]	22	10	4.5	2.5	1.5	
Footprint [m^2]	35°	83.3	13.8	2.7	0.79	0.33
	45°	132.6	21.6	4.3	1.2	0.51
	55°	260.8	40.8	8.15	2.29	0.96

The effect of noise is checked and removed from the measured data. The radar cross section measured by the Multi³Scat over the period of this experiment and at all various scatterometer settings (frequency bands, polarization combinations, and incidence angles) are shown in Figure 4.4. The effect of minor observation errors, unwanted spikes, and noises are reduced applying data smoothing. For this purpose, we applied the bin averaged of 1-day to show the variation of the data more clearly. However, for the rest of the analysis, we applied the bin averaged of 1-hour data. The fluctuations associated with some aspect of the months indicate a seasonal pattern observed by the radar backscatter.

The upper panel in Figure 4.4, compares the different radar frequencies and indicates the strongest variability of the RCS at X-band and the weakest variability is noticed for L-band RCS. The measurements of the 15 GHz frequency (Ku-band) are discarded due to the inappropriate high-frequency conductivity of the used cable, which produce the power loss due to the noise effect. This power loss increases with increasing the frequency, so that, the Ku-band is close to the noise level and affected strongly by noise and therefore we do not discuss the results of Ku-band in this study.

The middle panel discusses the differences between different polarizations, shows the strongest backscatter in vertical polarization.

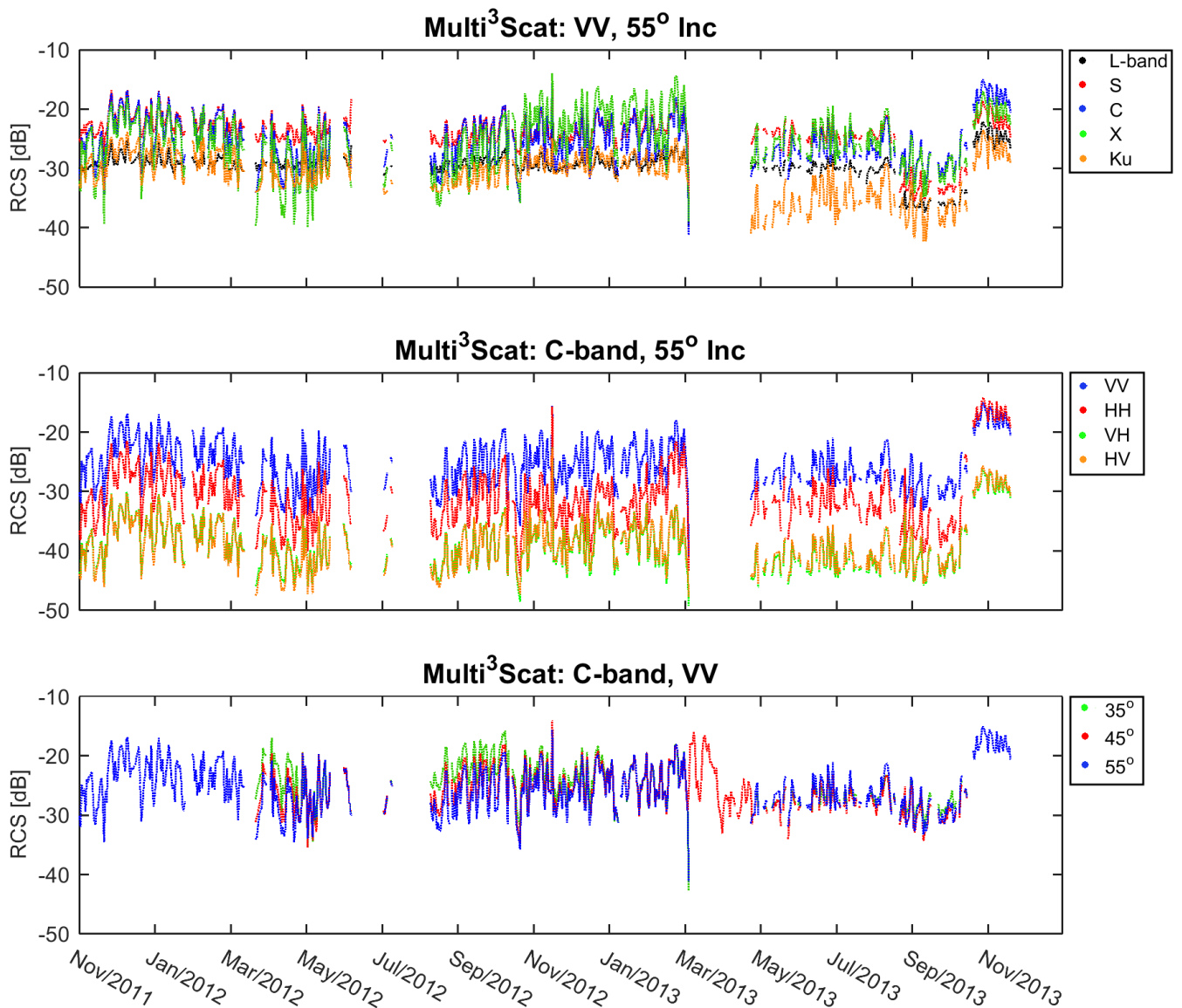


Figure 4.4: Variation of the radar backscatter measured by the Multi³Scat at different radar setting during the time of the measurements. Upper panel shows the backscatter with the focus on presenting the different microwave frequencies, the middle panel shows a comparison between polarization combinations, and the lower panel shows the aspect of various incidence angles. Each point indicates bin averaged of 1 day.

The two cross-polarized data sets lie almost on top of each other, suggesting that there is no difference between VH and HV radar backscatter at the wind speeds observed. Therefore, only the VH polarized signal is shown in the remainder of this thesis as a representative of cross-polarization signals.

The lower panel is focused on the variation of the radar backscatter at different incidence angles, indicates the strong backscatter signal at steeper incidence angle. However, we have

the longest time observation at 55° incidence angle.

The gap during the summer season (July and parts of August 2012) caused by the instrumental problem. The second gap during spring time (March and April 2013) caused by the problem in the motor which adjusted the scatterometer antenna angle, so that during this time the RCS is available only at 45° incidence angle (Figure 4.4-lower panel).

4.2.2 The research platform, FINO-2

The data used in this study are collected from the instruments mounted in the FINO-2 platform. The platform is situated in the western Baltic Sea, located 35 kilometers north of the island Rügen in the border triangle of Germany, Denmark, and Sweden. The coordinate of the platform is: $55^\circ 00' 24,94'' N, 13^\circ 09' 15,08'' E$. A plain view of the platform and its geographical location in the Western Baltic Sea is shown in Figure 4.5. The platform is in operation since May 2007 and has a total height of 100 meters above the water surface and water depth at the side of the platform is about 25 meters. In addition to our scatterometer which was mounted on the FINO-2 platform at the height of 25 meters above the sea surface, several other sensors are mounted for measuring the wind speed and direction, air temperature, air pressure, solar radiation, atmospheric humidity, and precipitation.

The equipment settled on the platform² are:

- Measuring device for determining the CO₂ flux
- Radar antenna on 25 meters height above the sea surface
- Boom in the southeast corner of the platform with meteorological sensors
- Waverider buoy in about 150 meters distance

²More information about the platform are available at www.fino2.de.

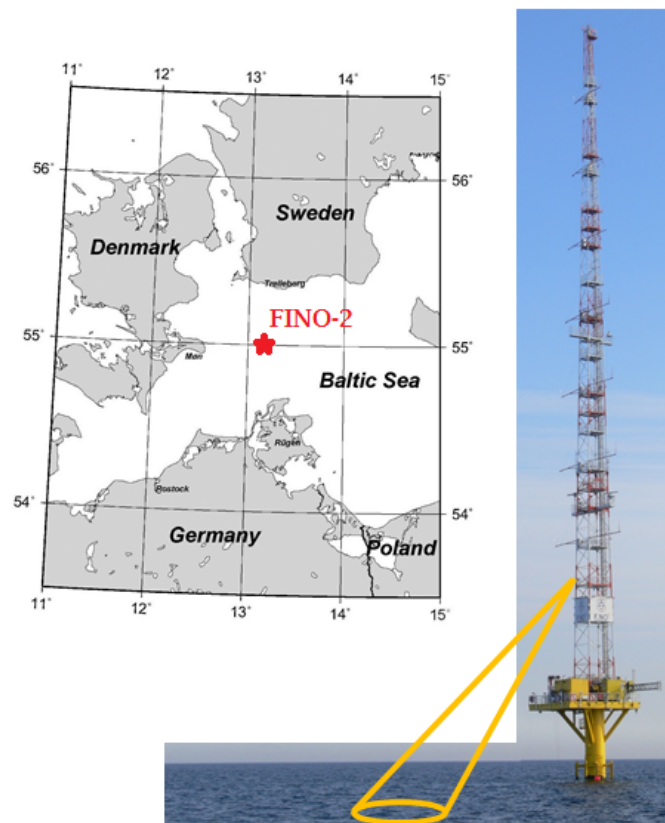


Figure 4.5: Photograph of the research platform FINO-2, which hosts the scatterometer (Multi³Scat) at a height of 25 m above the sea surface. FINO-2 is located 35 km north of the island Rügen in the Western Baltic Sea, border triangle of Germany, Denmark, and Sweden, (Pictured by Mayk Fischer).

4.3 Auxiliary Data

To quantify all relevant forcing and components of the sea surface roughness and gas transfer velocity, additional data like wind speed and direction, air and water surface temperature, wave height, CO₂ flux, the partial pressure of the CO₂ in the air and water, are required. The gas transfer velocity calculation from observations will be described in Section 6.1. Table 4.6 presents the auxiliary data used in this study including the timetable of observations for each data set. The detailed information regarding the measurements methods, instruments, and intervals are described in the following sections.

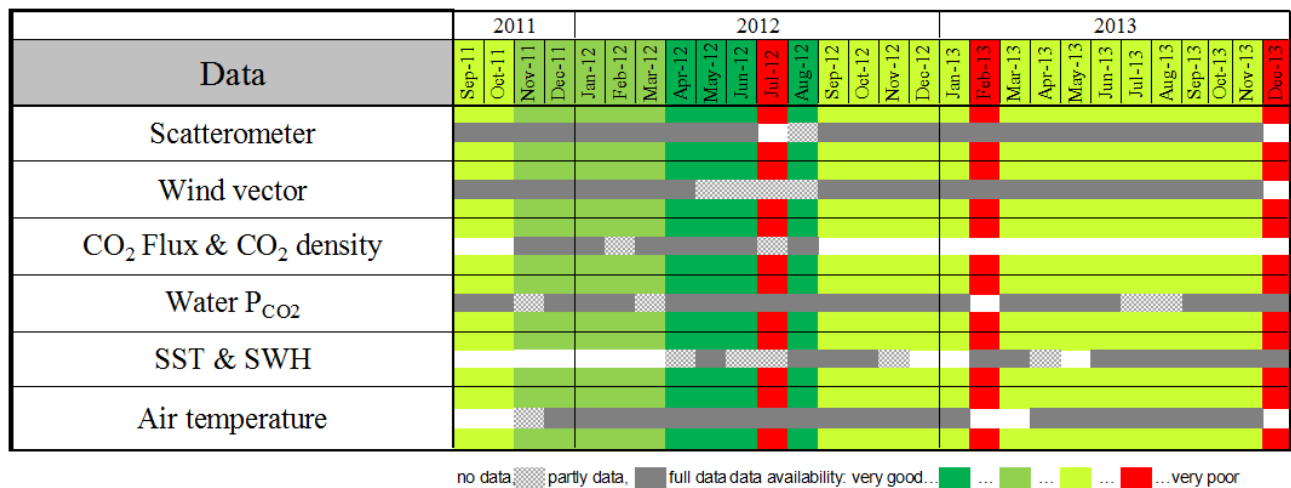


Figure 4.6: Time table of the auxiliary data measured in/near the FINO-2 platform and used in this study. The light gray boxes correspond the months with not completed observations due to the instrumental failure, and the white boxes are the months with no observation. The green colored boxes indicate months with all data sets available, and the red colored boxes are the the months with less data sets.

4.3.1 Wind

Wind speed and direction were recorded continuously by 8 anemometers mounted on the platform at every 10 m, from 30 m to 100 m heights. The wind speed is extrapolated to 10 m height using the measured wind speed at different heights, wind profile. The recording interval is 5 minutes. The wind speed changes from 1 m/s to 21 m/s and the dominant wind direction is westerly. Figure 4.7 summarizes the statistical distribution of the wind speed and direction. The histogram of the wind speed reveals occasional high values of wind speed, reaching 20 m/s and the highest number of the measurements during the moderate wind speed between 5 to 10 m/s. For the presented data, the overall mean wind speeds are 7.8 m/s and 7.4 m/s, and the standard deviations are 3.5 m/s and 3.7 m/s for years 2012 and 2013, respectively. The mean wind speed and the related standard deviation are shown in Figure 4.7 with vertical lines.

4.3.2 Air temperature

Air temperature is measured by temperature sensors (pt100) at different heights (every 10 m height) from 30 m to 100 m height with 10 minutes interval. Temperature measurements are available for 27 months from September 2011 to November 2013 in parallel to the scatterometer measurements. The temperature varies between -10°C to 25°C (Figure 4.9, fourth panel).

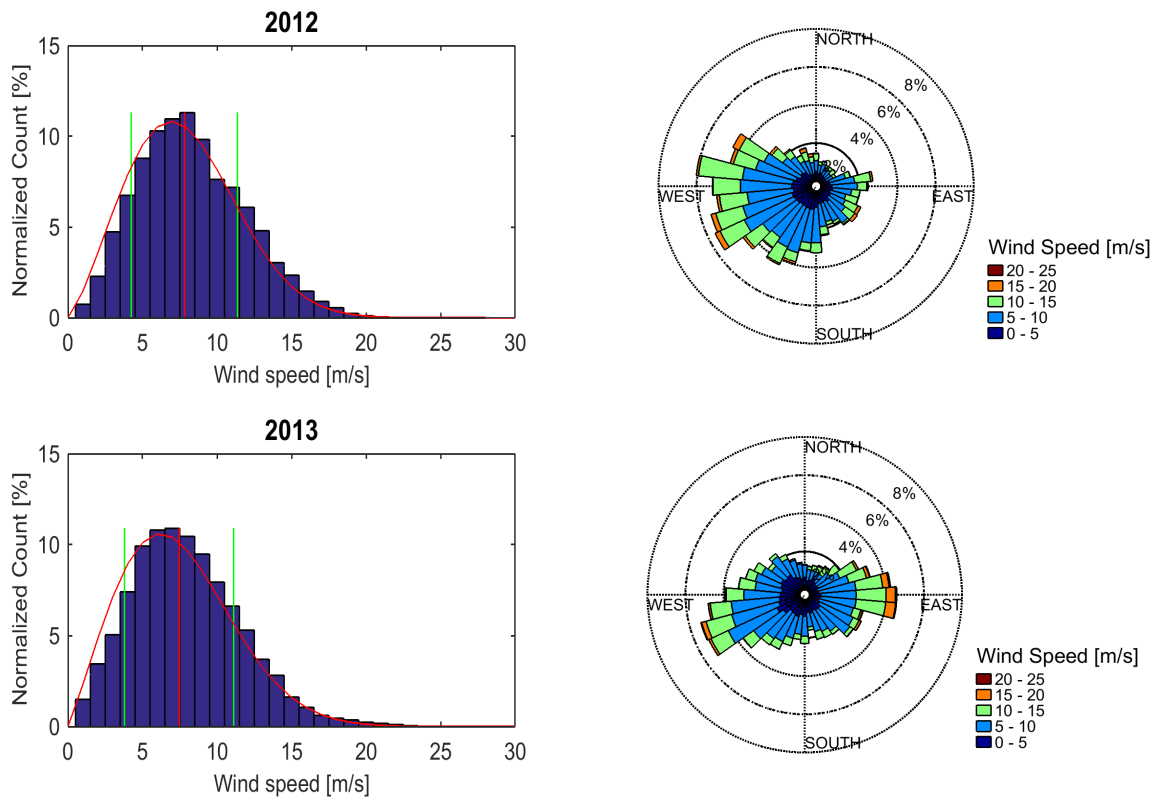


Figure 4.7: Wind speed distribution and wind direction for 2012 (upper panel) and 2013 (lower panel). The maximum number of wind speeds are in the range of moderate wind 5 m/s to 10 m/s and the dominant wind direction is westerly. The y-axis shows the percentage of the number of data with respect to the total number at each interval. The number of the data points are normalized with the sum of the values. The vertical lines indicate the mean value (red) and the standard deviation (black). The red line fit the distribution using Weibull distribution coefficients.

4.3.3 Buoy data

The water surface temperature and significant wave height are measured by a buoy (Directional Waverider MKIII). The buoy was about 150 meters away from the platform and measured the water temperature at the upper 50 centimeters depth every 30 minutes. The buoy measured wave height for wave periods of 1.6 to 30 s with resolution 0.01 m and measured water temperature with resolution 0.05°C. Figure 4.8 reveals high value of significant wave height, reaching 3.5 m in 2012 and more than 4 m in 2013 and the maximum number of the samples in the range of 0.5 to 1 m.

Figure 4.9 shows the entire time series of the data measured during our experiment; the wind speed and direction, air and water temperature and significant wave height as well as radar backscatter (one setup is shown as a sample).

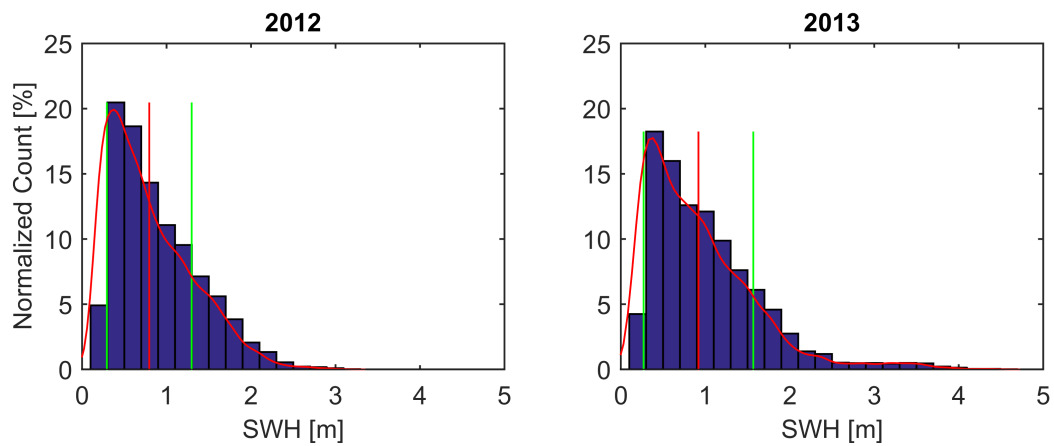


Figure 4.8: Significant wave height distribution from buoy, 150 meters away from the platform (55° N, 13° E), for 2012 (left panel) and 2013 (right panel). The y-axis shows the percentage of the number of data at 30 minutes interval. The vertical lines indicate the mean value (red) and the standard deviation (green). The red line fit the distribution using Kernel distribution.

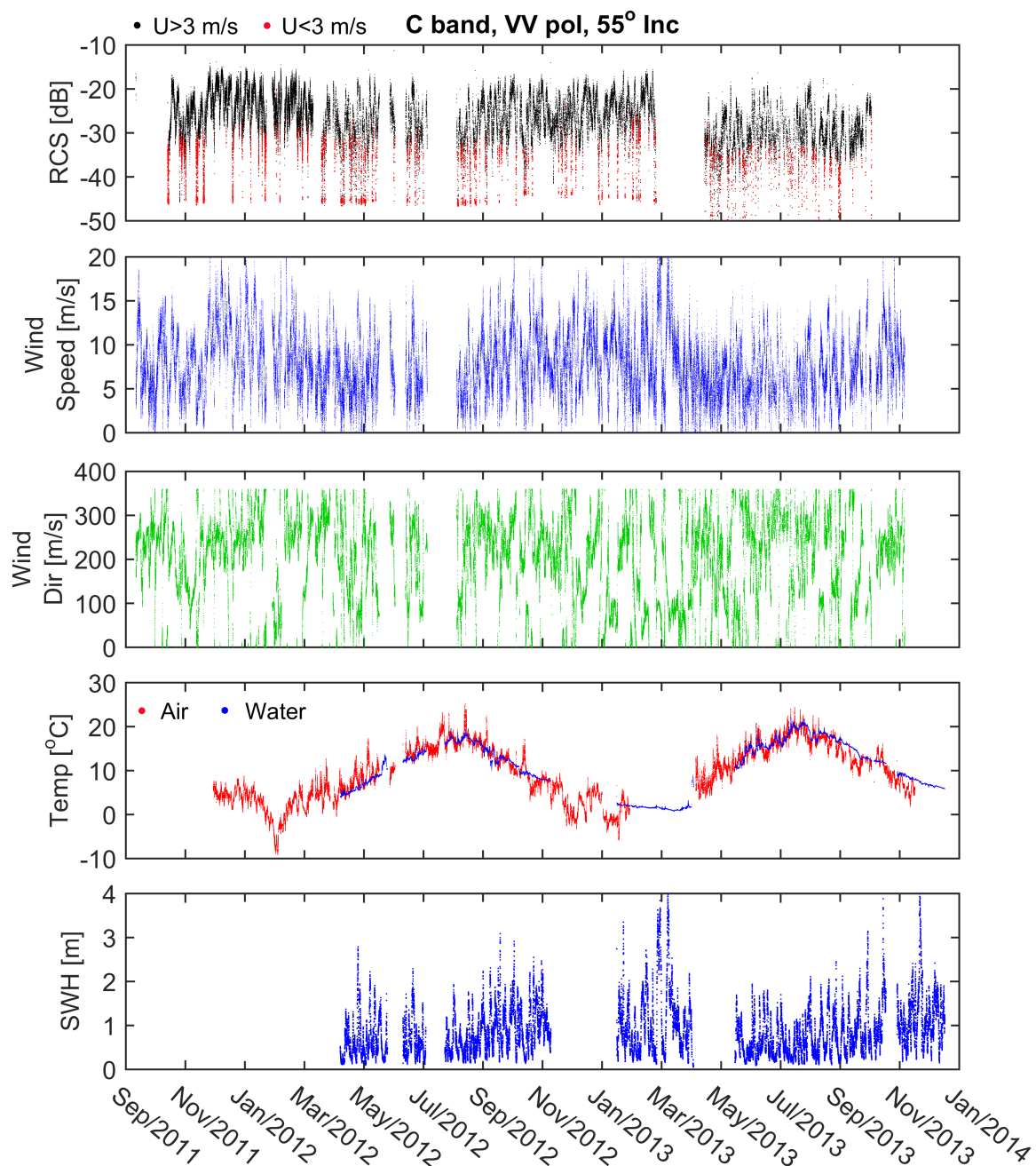


Figure 4.9: Time series of the data measured at FINO-2 platform. Radar backscatter at 5.3 GHz, VV pol, 55° Incidence angle (top). The black dots corresponds the backscattering in wind speed above 3 m/s and the red dots are the backscattering in wind speed below 3 m/s . Wind speed and wind direction over the measurements period (second and third, respectively). Water temperature measured by buoy placed about 150 m away from the platform (blue dots) and air temperature extrapolated to the temperature at 10 m height (red dots) (forth). Significant wave height measured by buoy (bottom).

4.3.4 CO₂ observations in FINO-2

Besides the meteorological instruments and a scatterometer, the eddy correlation setup consists of 3-component sonic anemometers (USA1) and open-path infrared gas analyzers (LICOR 7500) for CO₂ and H₂O were installed at a 9 m long boom south of the FINO-2 platform in two heights, at 6.8 m and 13.8 m above the sea surface from November 2011 till August 2012. Figure 4.10 shows the boom and the instrumentation at both heights. Open-path infrared gas analyzers were used to measure densities of carbon dioxide and water vapor in turbulent air structures and to provide measurements with a temporal resolution of 10 Hz. With the eddy covariance technique, these data are used in conjunction with sonic anemometer air turbulence data to determine the fluxes of CO₂ and H₂O over 30 min intervals. More details about the measurements and instruments are described in the paper published by [Lammert and Ament \[2015\]](#). Here we describe briefly the data processing method.

In order to start the EC processing, some pre-conditioning steps must be considered in advance. The objective of applying these steps is to obtain flux calculations as closely as possible to the real flux happening in the field.

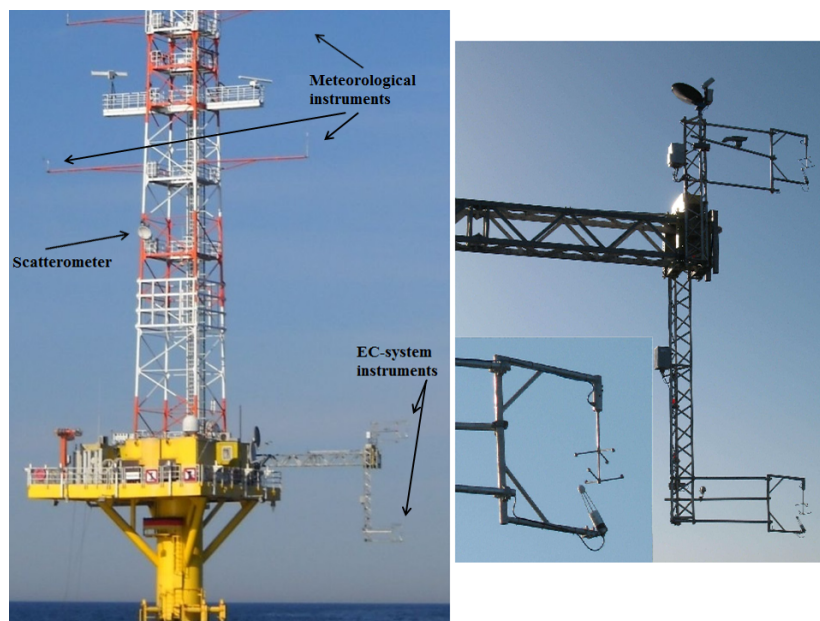


Figure 4.10: The platform with the boom and the eddy correlation setup including the gas analyzer and sonic anemometer at both heights, 6.8 m and 13.8 m (left). The picture source: Sonstiges Schiff, IMO:16563, by Toron; www.vesseltracker.com. The close view of the complete setup at both height (right), and more detail of the distance between the gas analyzer and the anemometer (small picture). The picture from [Lammert and Ament \[2015\]](#).

The data points which show a large deviation from neighboring data points (Spikes), assumed to have no physical meaning, therefore should be removed. They create due to the instrument and electronic noises and reduce the quality of the raw data.

To exclude the influence of platform on the measurements, the data are filtered in the case of northern wind directions, between 285° and 35° . The coordinate should be rotated in case of the sonic anemometer to separate u, v, and w wind components, and so vertical wind could be perpendicular to mean flow. The distance between the instruments used for this measurement (the anemometer and the gas analyzer), causes time interval between each instrument observations. The gas analyzer is installed below the sonic anemometer with a minimum possible distance (20 cm) considering a large possible sector without flow distortion (Figure 4.10). Eddy probability passes one of the instruments first and goes to the second one after a few second delays. This time interval must be removed. For this purpose, it is necessary to match the time series from the sonic anemometer and the gas analyzer by shifting the delay scan-by-scan. Then it is possible to find and remove the maximum deviation of the time series.

Overlapping the diurnal cycle with the turbulent motion time scale, changes in meteorological conditions and sensor drift produce low-frequency fluctuations which are against the assumption of stability in which the measurements are performed. To remove the low-frequency information, high-pass filtering, namely linear de-trending is used to subtract the mean values from instantaneous values to compute the fluxes. The fluctuations (X_t) with respect to the regression line can be obtained by subtracting the signal (x_t) from the instantaneous mean ($at+b$); $X_t = x_t(at + b)$. The slope, a, and the intercept, b, are determined from the linear regression line. More detail information about the eddy covariance data processing and filtering can be found at [Aubinet et al. \[2012\]](#).

Eventually, Webb-Pearman-Leuning correction (WPL correction) is used to compensate for fluctuations in the density of CO_2 , H_2O and other gases resulting from fluctuations in gas temperature and water vapor content [[Webb et al., 1980](#)].

The estimation of CO_2 flux is given based on multiplying the perturbations of carbon dioxide and the vertical wind velocity, and applying Reynolds averaging. The raw eddy-covariance fluxes of CO_2 were calculated over 30 min intervals from the fast sensors and were given by equation 4.1

$$F_{\text{CO}_2} = \overline{w'\rho'_{\text{CO}_2}} \quad (4.1)$$

where w is the vertical wind component (m/s) and ρ_{CO_2} is the mass density of CO_2 (g/m^3). The over-bar denotes mean, and the prime a perturbation from the mean.

The time series of CO_2 flux and concentration in the air, measured at FINO-2 platform

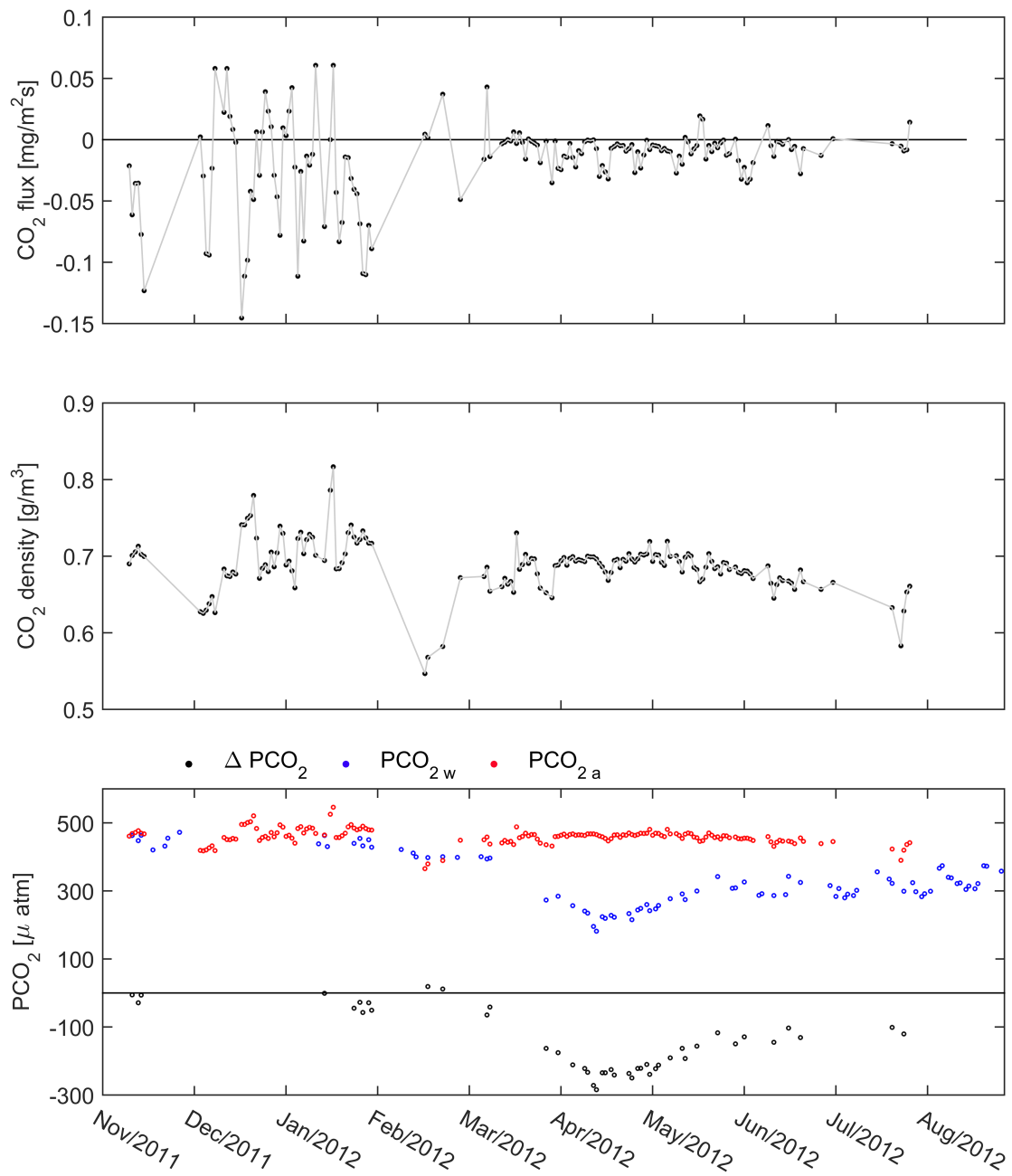


Figure 4.11: Seasonal cycle of daily averaged CO_2 flux, atmospheric CO_2 mass density and partial pressure in the air and water surface. Observations at the FINO–2 platform from November 2011 till August 2012. The flux and mass density of CO_2 are directly measured at the platform by eddy covariance method. The water P_{CO_2} is measured on a cargo ship close to the platform.

are shown in Figure 4.11 together with the water side P_{CO_2} measurements.

The water side P_{CO_2} measurements are performed on a cargo ship along a transect between Helsinki in the Gulf of Finland and Lübeck/Gdynia in the southwest of the Baltic Sea

[Schneider et al., 2014]. The P_{CO_2} measurements are performed by equilibration of surface water with air and detection of the equilibrium CO_2 concentration in air by IR spectroscopy.

The CO_2 flux shows seasonal cycle with lower valued during the summer in comparison to the flux measured during the winter. It is seen that the CO_2 flux varies between $0.05 \text{ mg/m}^2\text{s}$ up to $-0.015 \text{ mg/m}^2\text{s}$. Daily mean of atmospheric CO_2 density shows slight seasonal cycle with higher values during winter (0.8 g/m^3) and lower values during summer (0.6 g/m^3). It is assumed to be caused by the differences in the air density between the seasons. The water P_{CO_2} shows clear seasonality with low value during the spring which is up to $200 \mu \text{ atm}$ below the atmospheric level. During the winter time, the partial pressure difference reaches to minimum values close to zero due to the effect of biological productivity during the different seasons.

CHAPTER 5

Multi³Scat observations of sea surface

To study the air-sea interaction processes such as gas transfer, the boundary layer where all the exchanges between the ocean and atmosphere occur, is important. In the boundary layer, the combination of the surface physical properties such as wind, waves, and wave breaking, control the near surface turbulence and influence the air-sea gas exchange rate [Hwang and Fois, 2015; Hwang, 2005]. The sea surface roughness is a major contributor of radar backscattering from the sea surface [Hwang and Fois, 2015]. The response of the microwave backscatter to the surface roughness properties depends on the radar observation parameters (frequency, polarization, and incidence angle) and surface parameters (wind, surface roughness, and dielectric properties of the sea water).

To quantitatively better parameterize the gas transfer velocity using the radar scatterometer, first, we need to understand the surface properties which influence the radar response. To do this, observations collected in the Western Baltic Sea for 27 months period from September 2011 to November 2013 will be used to gain more insight into the sea surface roughness characteristics.

This chapter aims to evaluate the Multi³Scat system, which is new. This will be done by performing data quality assessment and evaluating the data against the scattering theory and models described in Chapter 3. In a first step (Section 5.1), the radar backscatter at different radar frequency, polarization, and incidence angle settings individually are tested and the strength and weakness of each radar observation parameters with regards to ocean surface roughness properties are evaluated.

Examples in the context of the different scatterometer observation parameters comparison are provided by Long et al. [1999, 1996]; Colton et al. [1995]; Rufenach [1995]; Keller et al. [1989a]; Donelan and Pierson [1987]; Plant et al. [1985] and others. Here, observations at various radar parameters for long time scale, provide us a unique measurement spectrum, and enable us to compare the backscatter from the full spectrum and make inferences about frequency and polarization dependencies which is not studied before. In a next step (Section 5.2), the combination of radar observation parameters (frequency, polarization,

and incidence angle) with respect to the parameters influence sea surface roughness such as wind speed, wind direction, atmospheric stratification, and significant wave height helped us to gain insight into the sea surface roughness characteristics at the scale of interest for gas transfer estimation and furthermore, an improvement in the gas transfer estimation from the scatterometer observation could be achieved.

5.1 RCS dependence on Frequency, Polarization, and Incidence angle

5.1.1 Incidence angle dependence

To evaluate the angular dependence of the Multi³Scat observations of the sea surface with respect to the scattering theory (see Section 3.2), we test the radar backscatter dependence to the incidence angle changes. Figures 5.1 and 5.2 display the averaged radar backscatter as a function of incidence angle at S-band and X-band radar frequencies (The related figures at L-band and C-band are shown in Appendix A.1). The theory of the angular dependence of the radar backscatter (see Figure 3.3, the region of our measurements), justifies using the interpolation between the three incidence angles. Therefore, the trend lines are used to connect the averaged value of the radar backscatter over three incidence angles with respect to the Bragg scattering theory. The radar backscatter are time-averaged over observations period, providing a single value for each incidence angle.

For a detailed analysis, we consider a specific range of wind speeds; to separate low wind and calm sea surface from high wind and rough sea surface. The average value of the radar backscatter at every radar observation parameters are calculated and presented for the wind ranges from 5 m/s to 7 m/s for low to moderate wind (circle) and from 15 m/s to 17 m/s for high wind speed (plus). We also performed the same analysis for different wind directions; upwind, downwind, and crosswind ($\pm 20^\circ$), shown in separate panels.

To quantitatively discuss how the data are spread around the average value, the standard deviation of each points in Figures 5.1 and 5.2 in the upwind direction are summarized in Table 5.1. The data are more spread at 55° incidence angle and low wind condition. The standard deviation varies between 2.0 dB to 4.5 dB depends on the polarization, incidence angle, and wind condition.

The angular dependence of the averaged radar cross section determined by the Multi³Scat observations confirms the existing theory (see Figure 3.3 and 3.2). The difference between VV and HH RCS increases at shallow incidence angle ($\theta = 55^\circ$). Moreover, is the difference

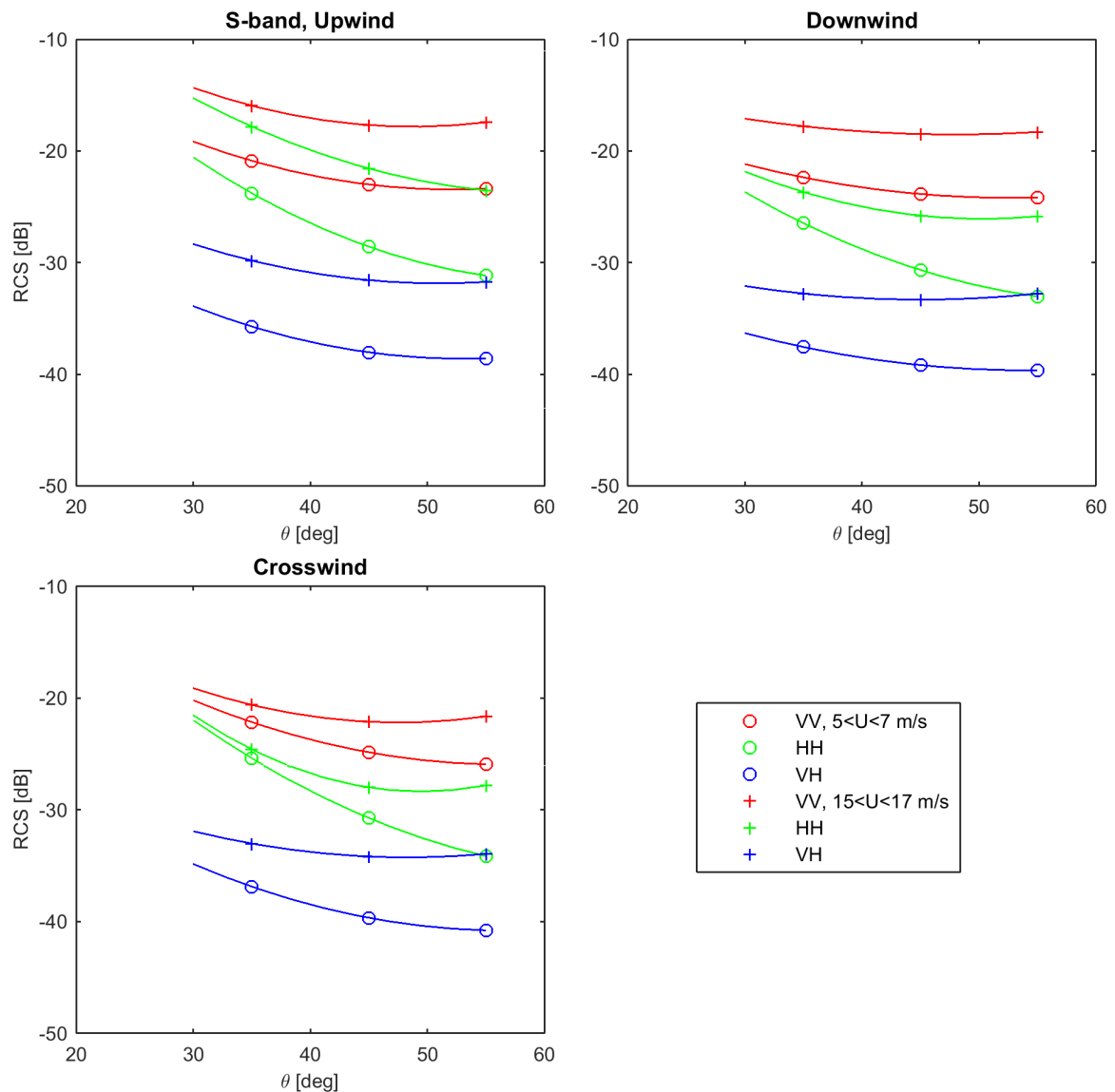


Figure 5.1: S-band radar cross section measured by the Multi³Scat as a function of incidence angle, for wind speed ranges $5 - 7$ m/s (o) and $15 - 17$ m/s (+), at different polarization combinations, VV (red), HH (green), VH (blue), and different wind directions, Upwind (upper left), downwind (upper right), crosswind (lower left), (radar frequency: 2.4 GHz, wavelength: 12.5 cm).

between high wind speed (corresponds to a rough sea surface) and moderate wind speed (corresponds to a calm sea surface), which increases at 55° incidence angle.

The radar backscatter at higher wind speed is stronger than at lower wind speed. This result is noticed at all radar frequencies and polarizations. Comparing the different frequencies, the stronger radar backscatter is seen at higher frequency bands. Remarkable is the averaged difference between the high wind backscatter and low wind backscatter. The dif-

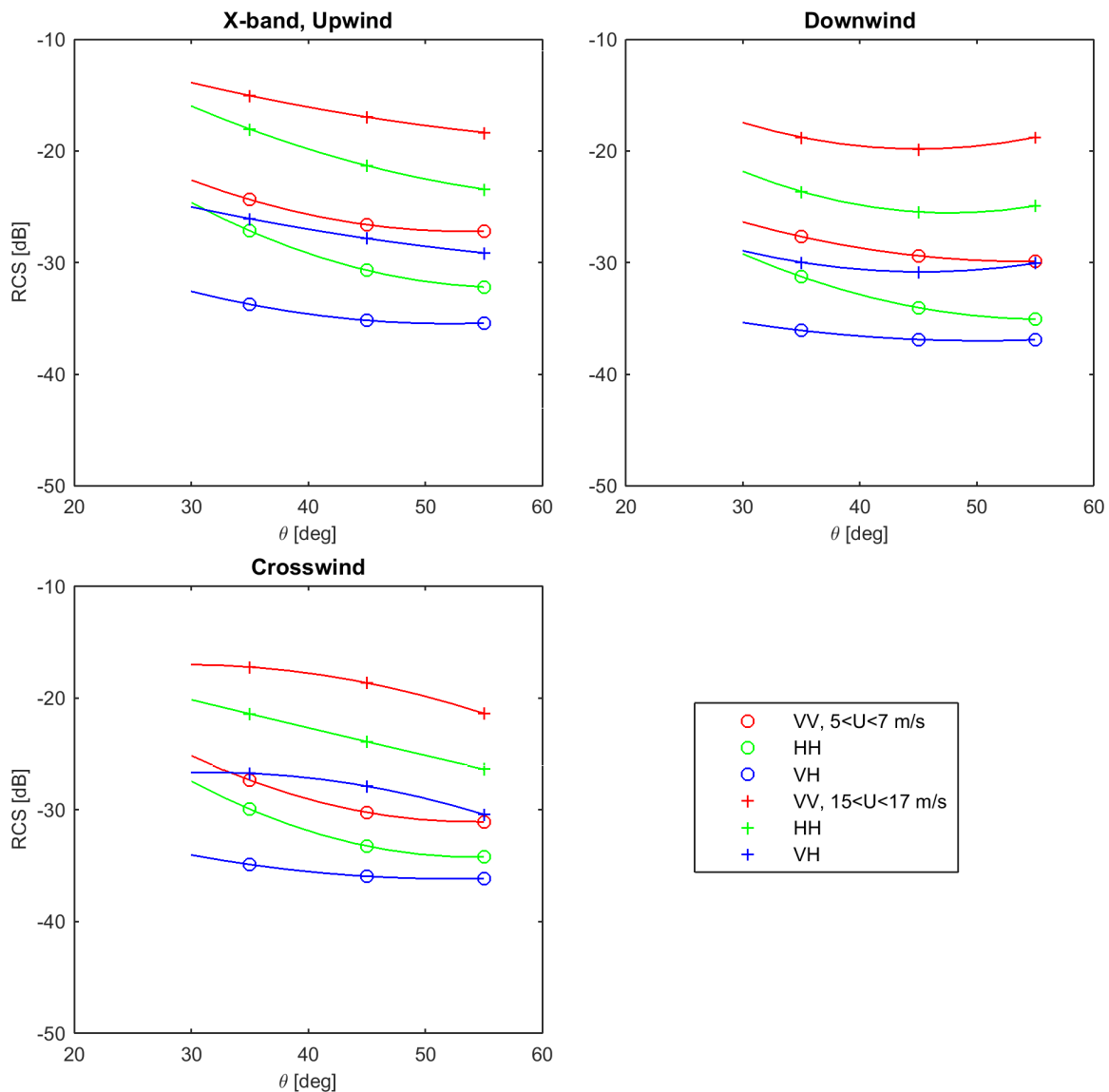


Figure 5.2: Same as Figure 5.1 but for X-band RCS (radar frequency: 1.0 GHz, wavelength: 30 cm).

ferences are larger in the high-frequency band than in L-band (see Figure A.1). The slope of the angular dependence is similar at all frequencies.

The radar backscatter clearly shows the larger intensity in vertical polarization (VV), and the smaller intensity in cross polarization (VH/HV). Moreover is the slope of the trend line, which is same in VV and VH-RCS. The different trend line slope in horizontal polarization (HH) caused by the different characteristics of the HH-RCS (the orientation of the electrical field of the EM wave) to measure the sea wave parameters. This implies a higher sensitivity of HH polarization to the angular variation than that of VV polarization, even though the

Table 5.1: Standard deviation (in [dB]) of the angular dependence of RCS measured by the Multi³Scat in different polarizations and incidence angles for S- and X-band microwave frequencies.

Wind	Polarization	Incidence angle	S-band	X-band	
Low wind($5 < U < 7m/s$)	VV	35°	2.5	2.6	
		45°	2.9	2.8	
		55°	3.0	2.9	
	HH	HH	35°	2.5	2.9
			45°	3.1	3.4
			55°	3.5	3.6
		VH	35°	3.9	3.7
			45°	4.4	3.9
			55°	4.4	4.0
High wind($15 < U < 17m/s$)	VV	35°	2.2	2.1	
		45°	2.5	2.2	
		55°	2.4	2.3	
	HH	HH	35°	2.0	2.3
			45°	2.5	2.8
			55°	2.9	3.0
		VH	35°	3.6	3.1
			45°	4.0	3.2
			55°	3.9	3.3

contribution of the Bragg waves in VV-RCS is higher than that of HH polarization. The HH polarization RCS also shows a higher sensitivity to the incidence angle changes at low wind speed rather than that of high wind speed. At high wind speed, the amplitude of the waves is high enough to produce strong radar backscatter at shallower incidence angle. At low wind speed, the waves are shorter with lower amplitude compare to the waves at high wind speed, So that at shallower incidence angle the radar backscatter is lower than that of at steeper incidence angle. Table 5.2, as an example, summarizes the slope of the curves related to Figures 5.1 and 5.2 in upwind direction.

The cross-polarization data also show a downward trend with increasing incidence angle but with rather a small variability at S-band and C-band for a given sea state, which means that the data are essentially independent of incidence angle. However, the strength of the cross-pol signal is less than co-pol signals and it might be influenced by the noise level. We did attempt to subtract the noise component, which could be important for low signal-to-noise-ratio cross-pol observations, however, it did not influence many of the data and we filtered those data points. Comparing the wind directions (different panels), the

radar backscatter at crosswind shows different behavior than upwind and downwind. The backscatter intensity is higher at upwind and downwind than at crosswind. Because the strong backscattering happens when the waves are faced toward or away from the radar look direction. The difference between the low wind and high wind RCS can not be found in L-band crosswind RCS.

To test the above experiments, we calculate the radar cross section from CMOD5 model function presented in Section 3.5.2. The input of the model is wind speed and direction, azimuth direction, and incidence angle and the output is the normalized radar cross section (NRCS). Because the output from Multi³Scat is not calibrated, the comparison with the CMOD5 model results can not be based on the absolute value but based on the dependencies and variation.

Figure 5.3, in addition to the RCS measured by the Multi³Scat, shows the C-band vertical polarization NRCS from CMOD5 model with black trend lines under the same wind condition as for the Multi³Scat RCS. For all wind speeds and directions, the CMOD5 model shows a higher intensity than the Multi³Scat. The bias between measured and modeled data are caused mainly by the calibration and normalization however, it might be caused by the other parameters. The downward trend is noticed for the results of CMOD5 same as for the Multi³Scat observations.

Remarkable is a different trend line slope for the CMOD5 model results (-0.28) compare to that of the Multi³Scat results (-0.13), meaning the sensitivity of the observed RCS by Multi³Scat to the angular variation is less than that of the model (see Table 5.2). More than different slope relative to the angular dependence is the different root mean square which is noticed at different wind conditions. At low wind speed the RMSE between the Multi³Scat and CMOD5 is about 1 dB more than at high wind speed, meaning that the Multi³Scat RCS can reflect more accurate insight information about the sea surface characteristic than the model. The impact of the combination of the interface parameters might not be accurately considered in the model, resulting these differences. The statistics of the Multi³Scat RCS and CMOD5-retrieved RCS with the slopes of the angular dependence are summarized in Table 5.2.

Table 5.2: Slope of the angular dependence of RCS measured by the Multi³Scat and CMOD5-retrieved RCS and the related statistics at different wind conditions.

		Slope	RMSE [dB]	Correlation
Low wind($5 < U < 7m/s$)	Multi ³ Scat	-0.21	7.52	0.64
	CMOD5	-0.36		
High wind($15 < U < 17m/s$)	Multi ³ Scat	-0.13	6.54	0.65
	CMOD5	-0.28		

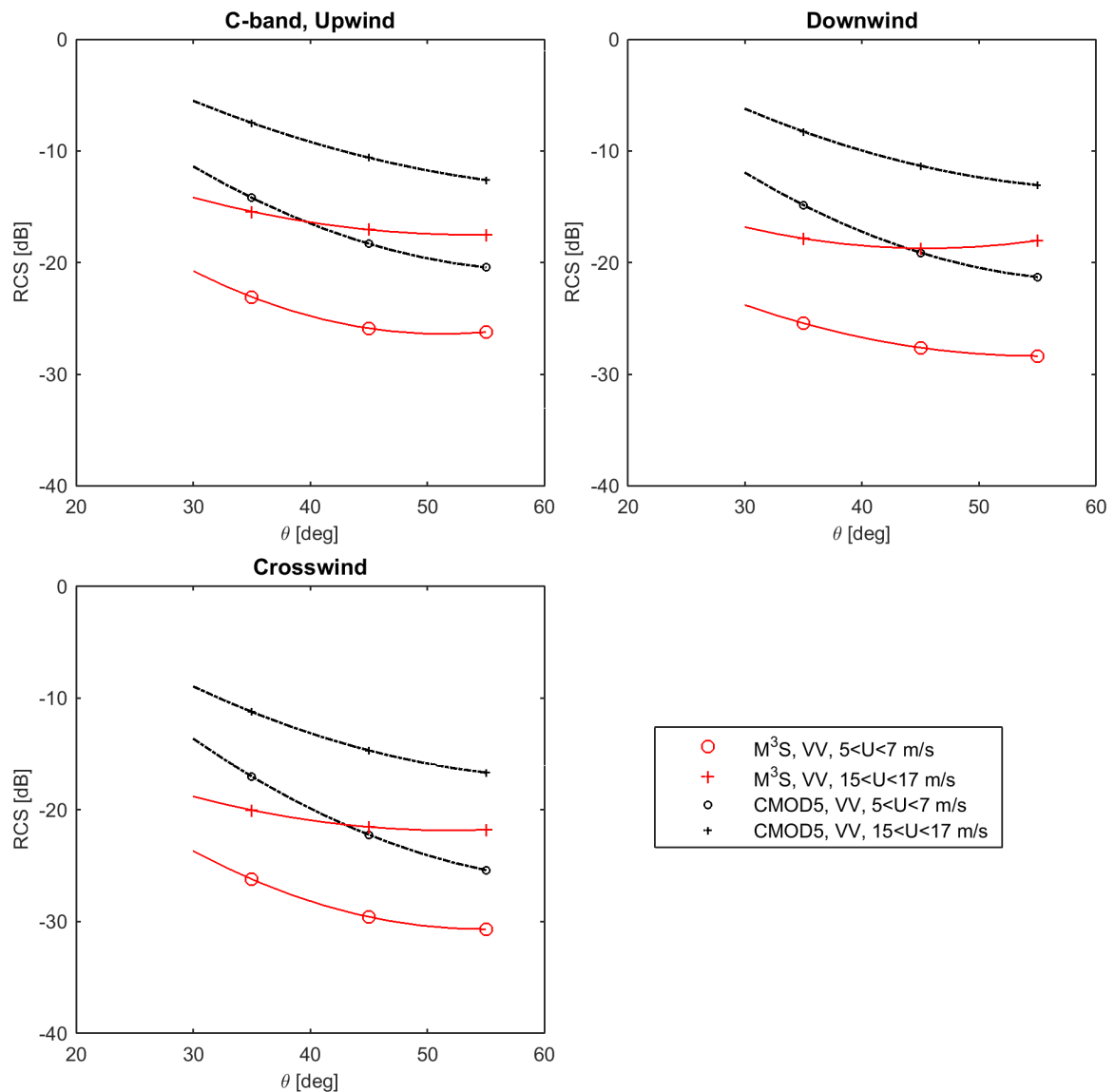


Figure 5.3: C-band, VV polarization radar cross section measured by the Multi³Scat as a function of incidence angle in comparison with CMOD5-NRCS at the same radar observation parameters, for wind speed ranges $5 - 7$ m/s (o) and $15 - 17$ m/s (+) and different wind directions, Upwind (upper left), downwind (upper right), crosswind (lower left), (radar frequency: 5.3 GHz, wavelength: 3.0 cm).

The correlation between the data sets are shown in Figure 5.4 for one year of the measurements, in steep (35°) and shallow (55°) incidence angles and upwind direction. Each data point corresponds to the averaged value over 1 day of measurements. The correlation between the data sets is about 0.66 in steep incidence angle and 0.80 in shallow incidence angle, however, a bias between the data sets shift the scatters to the right side of the diagonal line, meaning that CMOD5 overestimates the sea surface roughness. The averaged bias

between observations and CMOD5 NRCS of about 5 dB in 55° incidence angle will be considered to produce a calibrated RCS from the C-band Multi³Scat. The calibrated RCS will be used in addition to the RCS for gas transfer estimation and will be discussed further.

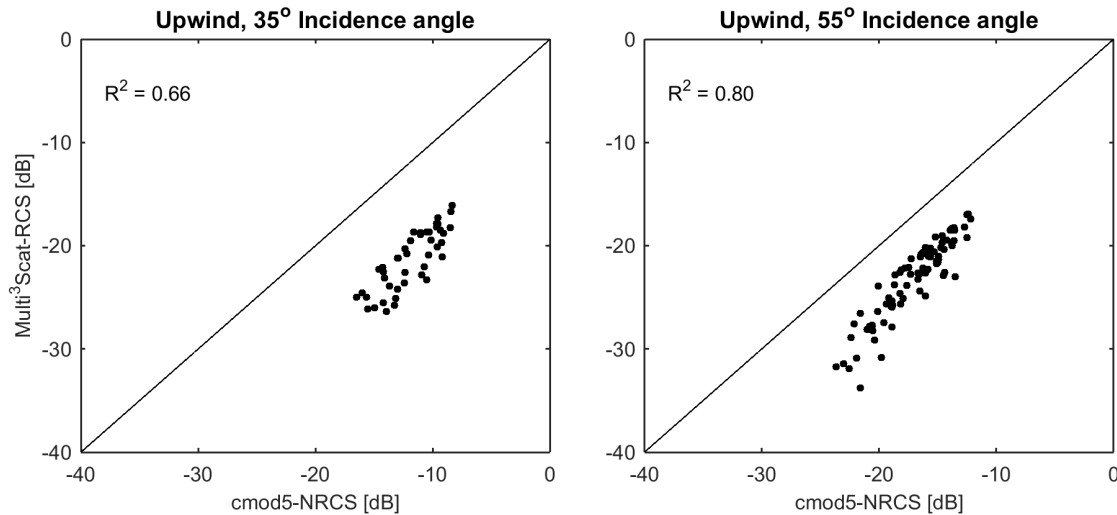


Figure 5.4: Multi³Scat RCS versus CMOD5 RCS in upwind direction, 35° incidence angle (left), and 55° incidence angle (right) over one year of measurements. Each data point corresponds to the averaged over 1 day of measurements.

5.1.2 The effect of different polarizations

The Multi³Scat measured both vertically and horizontally polarized RCS. The electromagnetic interaction of the radar signal with the ocean surface is different at different polarizations; depends on the surface/interface parameters (wind and waves). Therefore, polarimetric differences of the radar backscatter can provide us more detailed information of the sea surface roughness.

Following the theory described in Section 3.4, the radar backscatter consists of the contribution of the scattering from the tilted surface roughness component in Bragg resonance and the non-Bragg scattering from the steep waveform associated mainly with the wave breaking. The vertical polarization of the radar backscatter is dominated by Bragg scattering and provide the information of the sea surface roughness [Plant, 1990; Valenzuela, 1978]. The surface roughness reflected in VV polarization includes the combination of the component of wind generated roughness and wave breaking [Hwang and Fois, 2015]. However, the contribution of the Bragg resonance is more in VV polarization, thus, the wave breaking impact in VV polarization is less than that of HH and VH polarizations [Kudryavtsev et al., 2003].

The HH and VH polarizations include a higher degree of wave breaking contributions from non-Bragg part of the signal. They are more sensitive to wave breaking rather than to Bragg scattering. So that, the difference between VV and HH polarization is used as a method to extract the quantitative information about the surface roughness and wave breaking properties [Kudryavtsev et al., 2003]. It can be shown by polarization ratio of the radar backscatter ($PR = \frac{VV}{HH}$) (equation 3.5).

Moreover, the polarization ratio is not sensitive to the calibration factor which is an important issue when considering the radar backscatter from the different instruments (eg. a tower mounted scatterometer such as Multi³Scat and a spaceborne scatterometer such as ASCAT). The calibration factor will be disregarded in polarization ratio when the receiver chains for both channels (V and H) are equivalent.

The differences between VV and HH polarization of RCS is already discussed in Section 5.1.1. Here, we study the polarization ratio of the radar cross section at different radar geometry (incidence and azimuth angles) and surface properties (wind and waves). Figure 5.5, displays the results of PR analysis at different frequencies, two ranges of wind speeds (5 m/s to 7 m/s and 15 m/s to 17 m/s), and wind directions (upwind and downwind).

To compare the experimental data with CMOD5 model, and since CMOD5 does not provide the NRCS in HH polarization, this value is obtained through incorporation of a polarization ratio model proposed by Hwang et al. [2010] for C-band radar frequency with basic idea that: $\sigma_0^{HH} = \frac{1}{PR} \sigma_0^{VV}$, where σ_0^{VV} is CMOD5 model defined previously. For X-band radar backscatter, Shao et al. [2016] introduced a PR model using the TerraSAR-X and TanDEM-X dual-polarization data which relates the polarization ratio to the incidence angles and wind speed. Those PR models for C- and X-band radar backscatter are as below:

$$\begin{aligned}
 PR(U, \theta) &= A(\theta)U_{10}^{a(\theta)} \\
 A(\theta) &= A_1\theta^2 + A_2\theta + A_3 \\
 a(\theta) &= a_1\theta + a_2
 \end{aligned} \tag{5.1}$$

Table 5.3 shows the polynomial coefficients A_1, A_2, A_3, a_1, a_2 , using the least squares method. The fitting results of Equation 5.1 compared with the PR from observations by Multi³Scat are shown in Figure 5.5 for C- and X-band. The other polarization ratios presented in Figure 5.5 are from the studies by Vachon and Wolfe [2011] (equation 5.2) and Thompson et al. [1998] (equation 5.3) as a function of only incidence angle (θ) and can be written as below:

$$PR(\theta) = 0.283 \exp(2.452\theta) + 0.350 \tag{5.2}$$

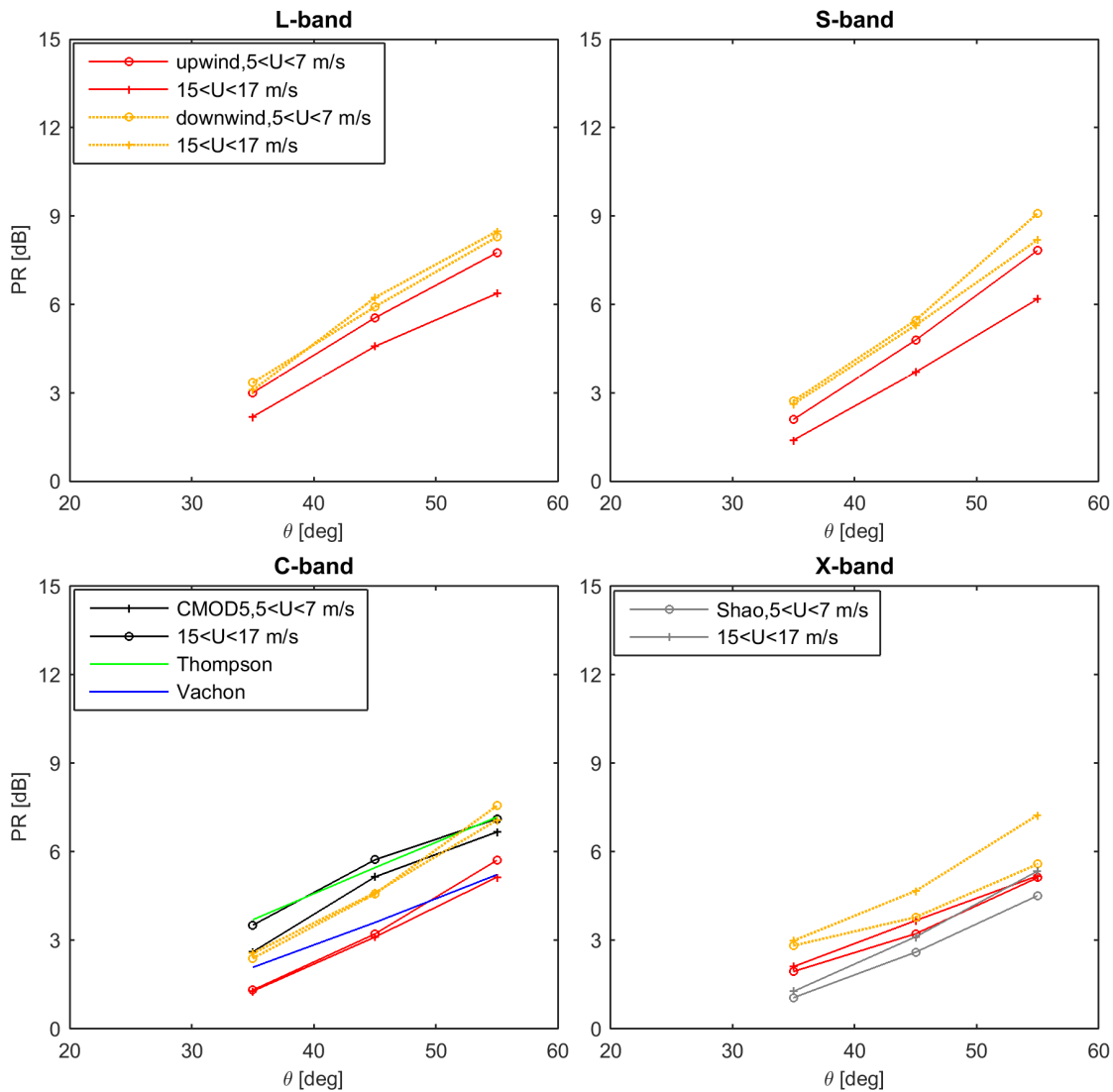


Figure 5.5: Averaged polarization ratio of radar cross section as a function of incidence angle, at four microwave frequencies (different panels show different frequency band), the Multi³Scat observations at two different wind speed ranges, 5 m/s to 7 m/s (o) and 15 m/s to 17 m/s (+), upwind direction (red) and downwind direction (light red). Comparison with CMOD5 model results (black curves), Thompson et al. [1998] (gray), Vachon and Wolfe [2011] (blue) at C-band, Shao et al. [2016] (gray) at X-band, under the same wind condition.

Table 5.3: C-band and X-band polarization ratio model coefficients (5.1).

Coefficients	A_1	A_2	A_3	a_1	a_2
C-band	0.0015	-0.0339	1.33	-0.0011	-0.0072
X-band	0.0011	-0.0615	1.9581	0.0082	-0.2308

$$PR(\theta) = \frac{(1 + \alpha \tan^2 \theta)^2}{(1 + 2 \tan^2 \theta)^2}, \alpha = 0.6. \quad (5.3)$$

where α is a constant which is defined empirically.

From Figure 5.5, remarkable is an upward trend at all wind conditions and radar settings. The PR value about 6 dB to 9 dB for L- and S-band and about 5 dB to 6 dB for C- and X-band at 55° incidence angle for all wind conditions are noted. This implies the differences between VV and HH radar backscatter at shallow incidence angle. At shallow incidence angle, the scattering from the resonance surface waves is less (the scatterometer senses the smaller wavelengths, Table 3.1, equation 3.2). The VV polarization of the radar backscatter is dominated by the Bragg scattering which here is weak. The HH polarization is more sensitive to the waveform and wave breaking [Kudryavtsev et al., 2003]. Therefore, using the PR will help to quantitatively study the surface roughness and wave breaking component of the sea surface.

The tendency of the PR at different frequency bands is similar but with less slope at a higher frequency band (X-band panel Figure 5.5). This corresponds smaller differences between VV and HH radar backscatter, rather than that of lower frequency bands, with regards to the weighting contribution of the Bragg resonance and wave breaking at higher microwave frequency; here the wave breaking effect is less in HH polarization in comparison to the lower frequency bands. Another reason for the differences between VV and HH polarizations could be the influence of mean square slope of long tilting waves on radar cross section which are carrying the shorter capillary waves Kudryavtsev et al. [2003]; Romeiser et al. [1997]. This impact is higher in HH polarization than in VV polarization and is more sensed at higher wind speed due to the larger waves, and would be sensed better at low microwave frequencies. Here, S-band and C-band PR can better display the differences between VV and HH as a consequence of waveform (tilt effect) and wave breaking impact and might be the better choices for gas transfer estimation.

Moreover, the difference between low wind and high wind PR increase at the higher incidence angle, from less than 0.5 dB reaching more than 1 dB. In upwind direction only at L- and S-band PR shows different value in low to high wind and at higher microwave bands and upwind direction, low wind and high wind PR shows very close values. Our results agree well with Shao et al. [2016] shown in the X-band panel of the figure 5.5, meaning that, polarization ratio can be used to quantify the non-Bragg parts of the signal associated with the wave breaking.

From Figure 5.5, our results shows lower values of PR compare to CMOD5 model. The difference in the sensitivity of observed PR to incidence angles at different wind speed ranges is very close to the model outputs. The similar tendency of our observation with the models is used as a quality assessment of our PR analysis. This leads us to express the polarization ratio as a function of incidence angle from Multi³Scat observations in different radar frequencies,

$$PR(\theta) = A.exp(B\theta) \quad (5.4)$$

with A, B constant coefficient, are shown in Table 5.4.

Table 5.4: Coefficient polarization ratio as a function of incidence angles for different microwave frequency bands based on the observed data used in this study (5.4).

Radar frequency band	A	B
L-band	0.314	0.048
S-band	0.199	0.055
C-band	0.280	0.044
X-band	1.470	0.035

5.2 Radar cross section dependence on wind and wave parameters

5.2.1 Wind speed influence

The dependence and sensitivity of the Multi³Scat observation to the interface parameters (wind and waves) is important for the purpose of our study. To develop a parameterization for gas transfer estimation in the air-sea interface, we need to evaluate the sensitivity of the Multi³Scat observation with respect to the parameters important in gas transfer study.

Wind speed dependence of radar cross section

The influence of wind is investigated using observations by Multi³Scat. Figure 5.6 displays RCS trend in VV polarization in each microwave frequencies with wind speed. Bragg scattering increases with the wind speed due to the enhanced resonant roughness component, and long-scale roughness caused by high wind speed decrease the specular return which results in higher radar backscatter at higher wind speed. The dependence on wind speed is shown in all radar observation settings (frequency, polarization, incidence angle). Vertical polarization shows higher intensity than horizontal and cross polarizations at all wind speed.

It can be seen from the figure that the sensitivity of the radar backscatter to wind speed increase at higher microwave frequency. To provide a quantitative assessment of the sensitivity analysis, the slope of the RCS-wind dependence is computed. The RCS is wind-averaged over one year of observations, providing values for every 0.5 m/s wind scale. Figure 5.7 display the variation of the slope of the RCS-wind dependence with respect to the microwave

frequency and for different polarizations. The slopes are presented in Table 5.5. A smaller slope corresponds to less sensitivity of the radar backscatter with wind changes.

From both Figure 5.7 and Table 5.5, it is noticed that the RCS at higher microwave frequency band is more sensitive to the wind speed changes than the lower frequencies.

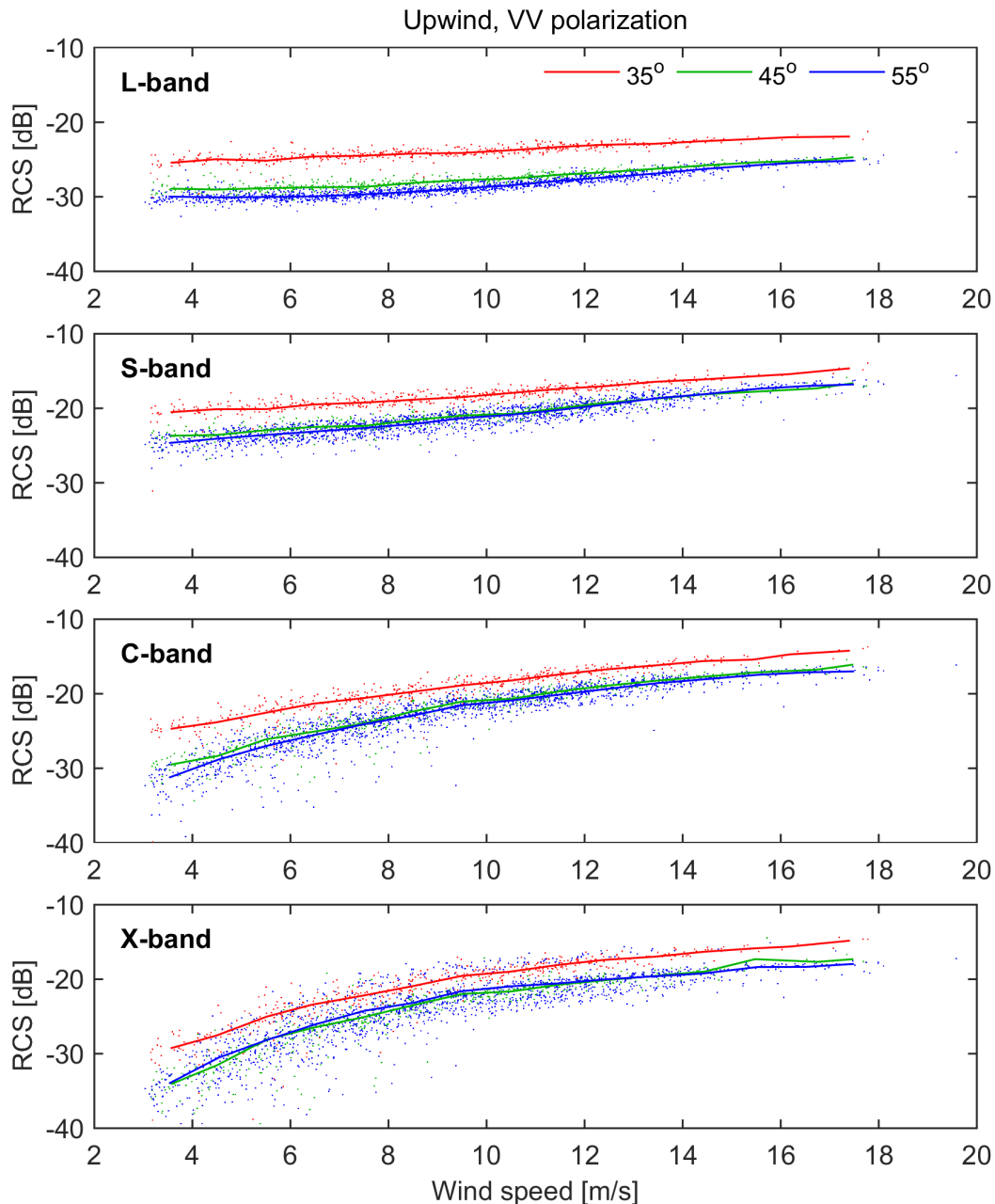


Figure 5.6: Radar cross section in dB in VV polarization as a function of wind speed in m/s , at four microwave frequencies (L-, S-, C-, X-band respectively from upper panel to lower panel), upwind direction and three incidence angles (35° (red), 45° (green), and 55° (blue)). Each data point corresponds to an average over 1-hour measurement period and the lines show wind-averaged radar cross section for the windows of $0.5m/s$ wind speed.

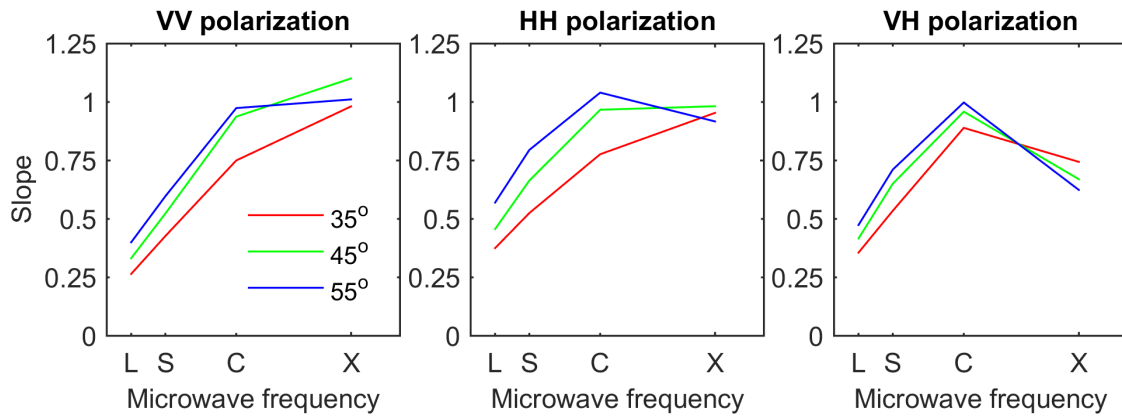


Figure 5.7: The slope of the RCS-wind dependence shown in the Figure 5.6 as a function of microwave frequency band. Each panel displays the slopes at different incidence angles (35° (red), 45° (green), and 55° (blue)) for specific polarization; VV polarization (left), HH polarization (middle), and VH polarization (right).

Table 5.5: The slope of the radar cross section-wind dependence for different radar observation settings (frequency, polarization, and incidence angle).

Radar frequency band		VV	HH	VH
L-band	35°	0.26	0.37	0.35
	45°	0.33	0.45	0.41
	55°	0.40	0.56	0.47
S-band	35°	0.42	0.52	0.53
	45°	0.52	0.66	0.65
	55°	0.59	0.78	0.71
C-band	35°	0.75	0.80	0.88
	45°	1.02	1.04	1.01
	55°	0.97	1.01	0.99
X-band	35°	1.08	1.01	0.76
	45°	1.24	1.04	0.69
	55°	1.09	0.95	0.65

Regarding the incidence angle, steeper incidence angle clearly shows less sensitivity to the wind speed changes, however, 45° and 55° incidence angles show different behavior; at lower frequency bands 55° incidence angle RCS is more sensitive to the wind speed changes and at higher frequency bands is less sensitive to the wind speed changes than that of the 45° incidence angle.

The X-band radar backscatter, however, shows a fall off in HH polarization and even stronger in VH polarization. Regarding the information in Table 3.1, X-band radar backscatter senses the shorter wavelength stronger than the lower frequency bands. At high wind speed, the sea surface is very rough with large waves and wave breaking which can not be

completely sensed by the X-band radar backscatter. Therefore, the variation of the X-band RCS from the low wind to high wind is less than the lower microwave frequency. This result is valid in HH and VH polarizations, however, in VV polarization the X-band RCS shows the highest sensitivity to the wind speed changes (5.5 and 5.6). It means that X-band is proper frequency band for Bragg scattering mechanism but not for the wave breaking properties. Figures 5.8 and 5.9 display the same experiments as in VV polarization wind speed dependence but in HH and VH polarizations.

Cross polarization at higher radar frequency shows the same sensitivity to wind speed for all incidence angles, meaning that the cross polarization signals are weakly dependent on the incidence angle. This suggests the possibility of sea surface roughness estimation from cross-polarizations, without the knowledge of local incidence angles and tilting effect [Vachon and Wolfe, 2011]. However, VV polarization also shows the same sensitivity to incidence angles from 45° to 55° but it could be seen a stronger backscatter at 35° incidence angle with the different trend from low wind to high wind speed and shows the dependence of the VV polarization to the incidence angle.

The signal saturation which happens at high wind speed radar scatterometry is not manifest in these figures because of the limited range of wind speed in the area of our measurements, but the loss of the wind sensitivity toward high winds is noticed with nonlinear trends especially at higher microwave frequencies (C- and X-band). This signature indicates the signal saturation under higher wind speed at co-polarizations while cross-polarization signals do not suffer from the signal saturation under high wind speeds, and therefore can be used to retrieve sea surface roughness at high wind speeds.

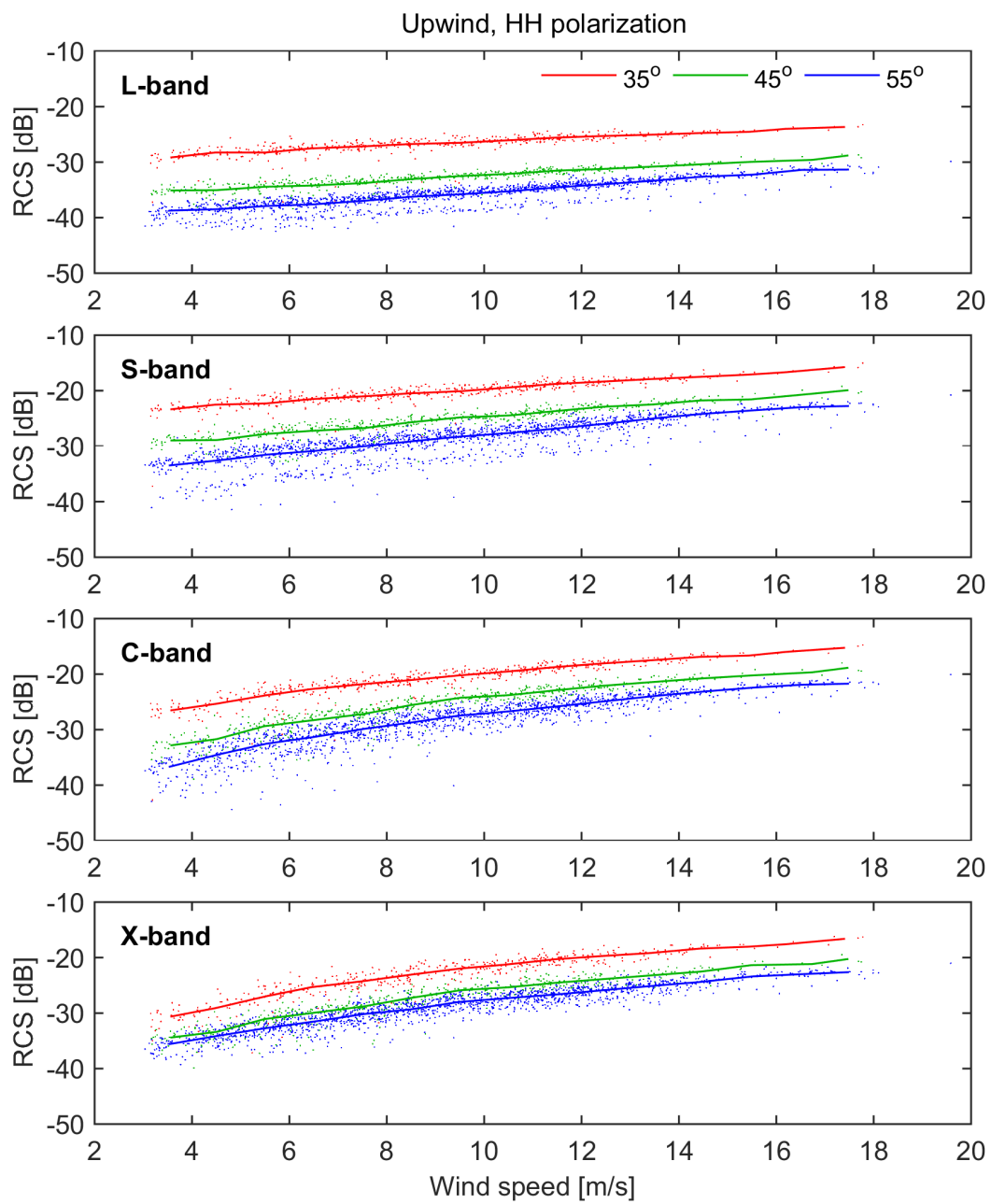


Figure 5.8: Same as Figure 5.6, but in HH polarization radar backscatter.

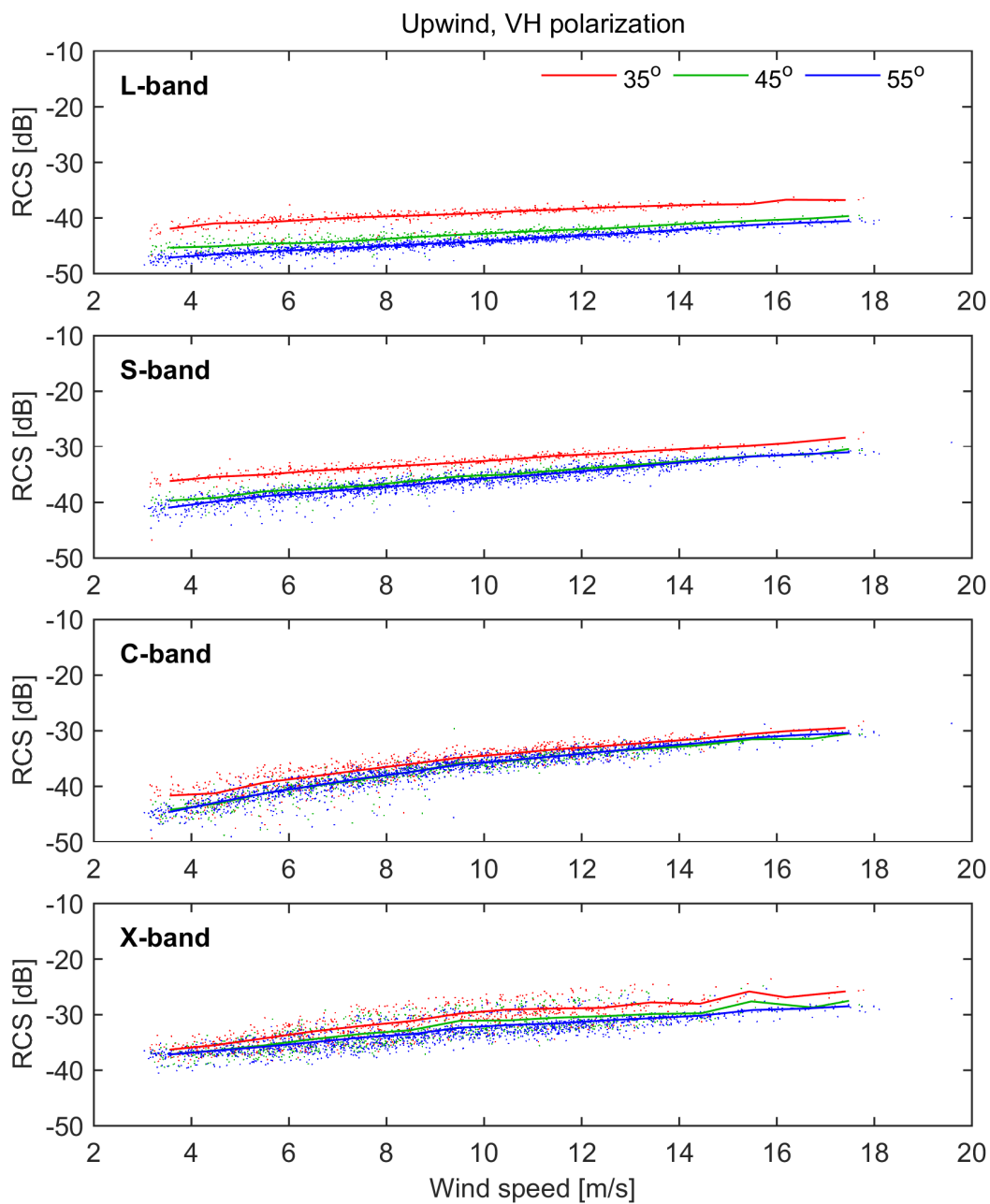


Figure 5.9: Same as Figure 5.6, but in VH polarization radar backscatter.

Wind speed dependence of polarization ratio

To investigate the influence of wind speed on polarization ratio from the Multi³Scat observations, we make an analysis of PR behavior with wind speed changes at different radar observation settings (frequency, polarization, and incidence angle). The sensitivity of the PR to wind speed changes can be further used for gas transfer analysis, whereas the PR is not influenced by the calibration factor, therefore, the results can be compared with the same

results of the other instruments.

Here, we present the results of the analysis in the upwind direction (Figure 5.10). The same analysis in downwind direction is shown in Appendix A.5. In agreement with the PR dependence to incidence angles, this Figure displays the variation of the PR with respect to the wind speed changes. From Figure 5.10, a downward trend is remarkable for lower microwave frequencies (L-band and S-band).

The decrease in PR value at high wind speed is a consequence of the non-Bragg scattering influence on HH polarization which is caused by the wave breaking and steep waveforms

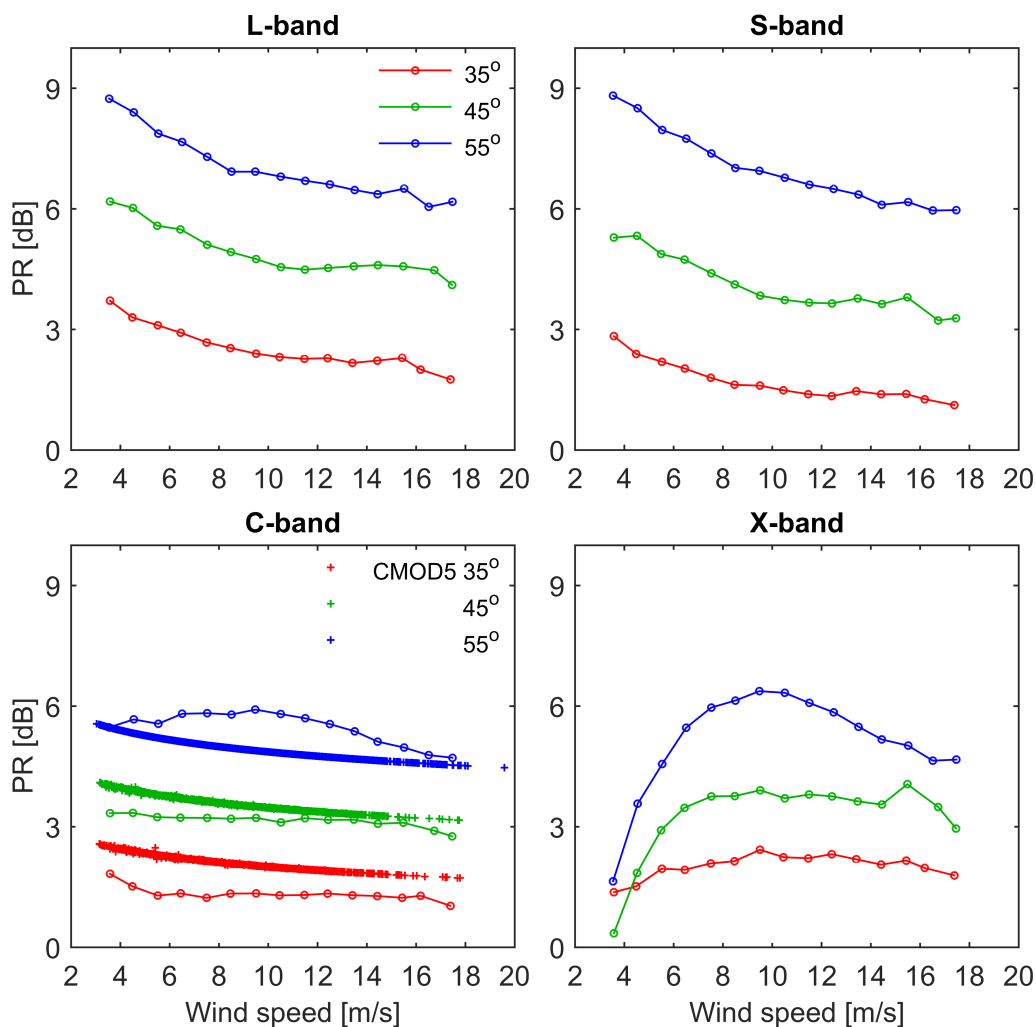


Figure 5.10: Polarization ratio in dB as a function of wind speed in upwind direction from the Multi³Scat observations (circles), at four different frequency bands (L-, S-, C-, and X-band; corresponds to each panel) and three incidence angles (35° (red), 45° (green), and 55° (blue)). CMOD5-PR (calculated in combination with the PR model of Hwang et al. [2010]) at three incidence angles are shown in filled balls. Each data point corresponds to wind-averaged over 1 year of observation, providing values for every 1 m/s wind scale.

effect at high wind. These effects are weak in VV polarization and cause the PR downward trend at higher wind speed.

The C-band PR shows less sensitivity to the wind speed changes, and furthermore, X-band PR shows different behavior to the wind speed changes. Combining the results of Figures 5.10 and A.4, the reason for this behavior in X-band PR is caused by the variation of VV polarization RCS at X-band. Signal saturation at high wind speed affects VV polarization more than HH polarization, resulting in small PR at high wind speed. For C-band PR, at 55° incidence angle, a drop at high wind speed is noticed which does not exist for other incidence angles. This implies the effect of the weak Bragg resonance surface waves scattering at shallow incidence angle. At moderate incidence angle, however, the impact of the micro-breaking waves modify the radar backscatter in VV polarization. With increasing the wind speed, the micro-breaking waves change to the breaking waves of the large scale which are less visible in VV polarization. Referring the equation 3.2, VV polarization RCS at higher frequency bands (C-band and X-band) respond differently to the high wind speed. This effect is remarkable in PR analysis.

To assess the performance of our PR analysis, we compare the results of the Multi³Scat observations with the CMOD5 PR in combination with the model of Hwang et al. [2010] (depends on both θ and wind) (Figure 5.10, lower left panel). The Multi³Scat PR agrees well with PR model with correlation coefficients of 0.67, 0.40, and 0.44; and offset of 0.75 dB, 0.36 dB, and 0.45 dB for 35°, 45°, and 55° incident angles, respectively. From Figure 5.10 the PR model of CMOD5+Hwang shows larger values than Multi³Scat PR over the whole range of wind speed by about 0.5 dB for 35° and 45° incidence angles. This small differences between our results and previous studies of Hwang et al. [2010] and Zhang et al. [2010], confirms the quality of the Multi³Scat observations.

5.2.2 Effect of azimuth angle

The anisotropy of the radar backscatter is an important factor for the purpose of our study because a change in the wind direction does not affect the flux measurements but might affect the radar backscatter from the sea surface and must be validated for the Multi³Scat observations. The relative angle between the wind-wave propagation direction and the antenna viewing direction has a strong influence on the tilt modulation. With the wave crests moving parallel to the antenna viewing direction (downwind), modulation contribution is weak. This effect is more visible in HH polarization than in VV.

Upwind to downwind asymmetry is the consequence of hydrodynamic modulation of short waves which are carried by the longer underlying waves [Kudryavtsev et al., 2003;

Romeiser et al., 1997]. The upwind to crosswind asymmetry of the radar backscatter is due to the angular distribution of the wave height spectrum [Kudryavtsev et al., 2003]. The anisotropy of radar backscatter needs to be studied because of the disagreement between observations and model [Kudryavtsev et al., 2003; Romeiser et al., 1997]. First, we make an analysis of the RCS anisotropy (directional dependence) and then we will expand the analysis to PR anisotropy.

Azimuth dependence of radar cross section

Figure 5.11 shows the averaged C-band RCS measurements in VV, HH, and VH polarizations as a function of the wind direction. Each panel displays observation at different wind speed from 4 m/s to 14 m/s . The data are averaged over 1 year of observation, providing values for every 10-degree wind direction. To assess the performance of the anisotropy analysis by the Multi³Scat observations, the radar backscatter obtained from the CMOD5 model in combination with the Hwang PR function to calculate HH polarization is used. Here we show the results obtained from incidence angle 45° , however, the results for 35° and 55° are shown in Appendix A.3 and will be discussed.

As depicted in Figure 5.11, the modulation of the measured VV and HH-RCS with the wind direction shows a similar trend in the CMOD5 results. The two maxima are in upwind and downwind and the two minima are in crosswind directions. The vertical black line in the figure indicates the upwind direction. The bias between the Multi³Scat observations and CMOD5 model results is caused by the calibration factor.

From the Multi³Scat observations, an increase in the directional dependence is noticed from low wind to high wind speed. The upwind-crosswind asymmetry increases with increasing the wind speed which is more clear in the Multi³Scat observations rather than that of the model results. The upwind to downwind asymmetry at C-band, 45° is weak, however, there is a small asymmetry at high wind speed (less than 1dB). Observations at higher wind speed are not shown because, in higher wind speed ranges, there is not enough data to firmly conclude on the behavior of the upwind-downwind and upwind-crosswind asymmetry. Our observation fully confirms the theoretical prediction shown in Robinson [2004] at 13.9 GHz-RCS, discussed in Section 3.5.1 (Figure 3.4).

Azimuth dependencies of the radar backscatter at different incidence angles are shown in Figure 5.12 for C-band radar backscatter. The same experiments for the other microwave frequencies (L-, S-, and X-band) are shown in Appendix; Figures A.6, A.7, and A.8. Here, L-band RCS at low wind speed shows no dependence on azimuth changes at all incidence angles.

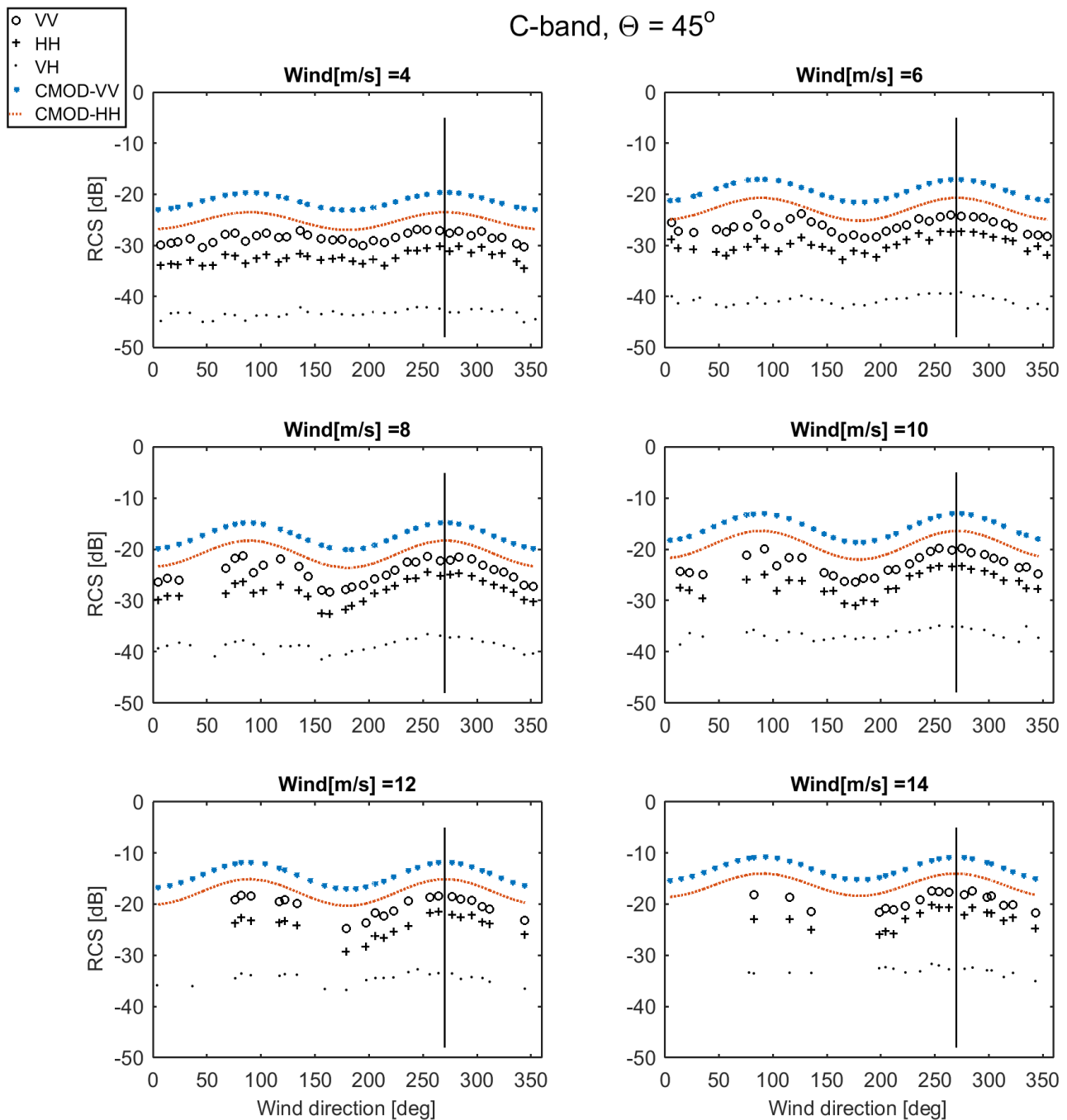


Figure 5.11: C-band radar cross section in VV (circle), HH (plus), and VH (dot) polarizations, as a function of the wind direction, for the incidence angle of 45° in different case of wind speed from 4 m/s to 14 m/s (± 1 m/s). Each data point corresponds to the averaged value over 10 deg wind direction for the duration of 1-year observations. The CMOD5 model results are plotted as blue filled circles and CMOD5+Hwang PR model in HH polarization is plotted as red dots. The vertical bar indicates the upwind direction.

At high wind speed, the RCS dependence on azimuth is more clear especially at higher incidence angles (55°). Comparing the different frequencies, higher microwave band shows stronger upwind-crosswind asymmetry at all incidence angles and wind speeds. Except at L-band, RCS anisotropy at low wind speed is weak in 35° incidence angle for all microwave frequencies.

At low wind speed, the observed upwind-crosswind asymmetry increases with incidence angle, however at high wind speed the directional dependence are statistically nearly equal for all incidence angles. This change is slightly larger in VV polarization than in HH polarization. As described by [Mouche et al., 2006], the reason for this effect is that the polarized part of the backscatter which is controlled by the Bragg resonance dominates the upwind-crosswind asymmetry and is visible in VV polarization-shallow incidence angle radar backscatter. At high wind speed, the wave breaking contribution in the total signal is more than Bragg resonance, effect small changes in upwind-crosswind asymmetry with incidence angle changes.

The behavior of the cross polarization scattering with the azimuth direction looks different from the co-polarizations (dots in Figure 5.11). A stronger modulation with the wind direction is shown by co-polarization compared to that of the cross polarizations. No matter what is the wind speed, incidence angles, or radar frequency, the cross polarization shows relatively small wind direction dependencies when compared to the peak to peak modulation of VV and HH polarizations.

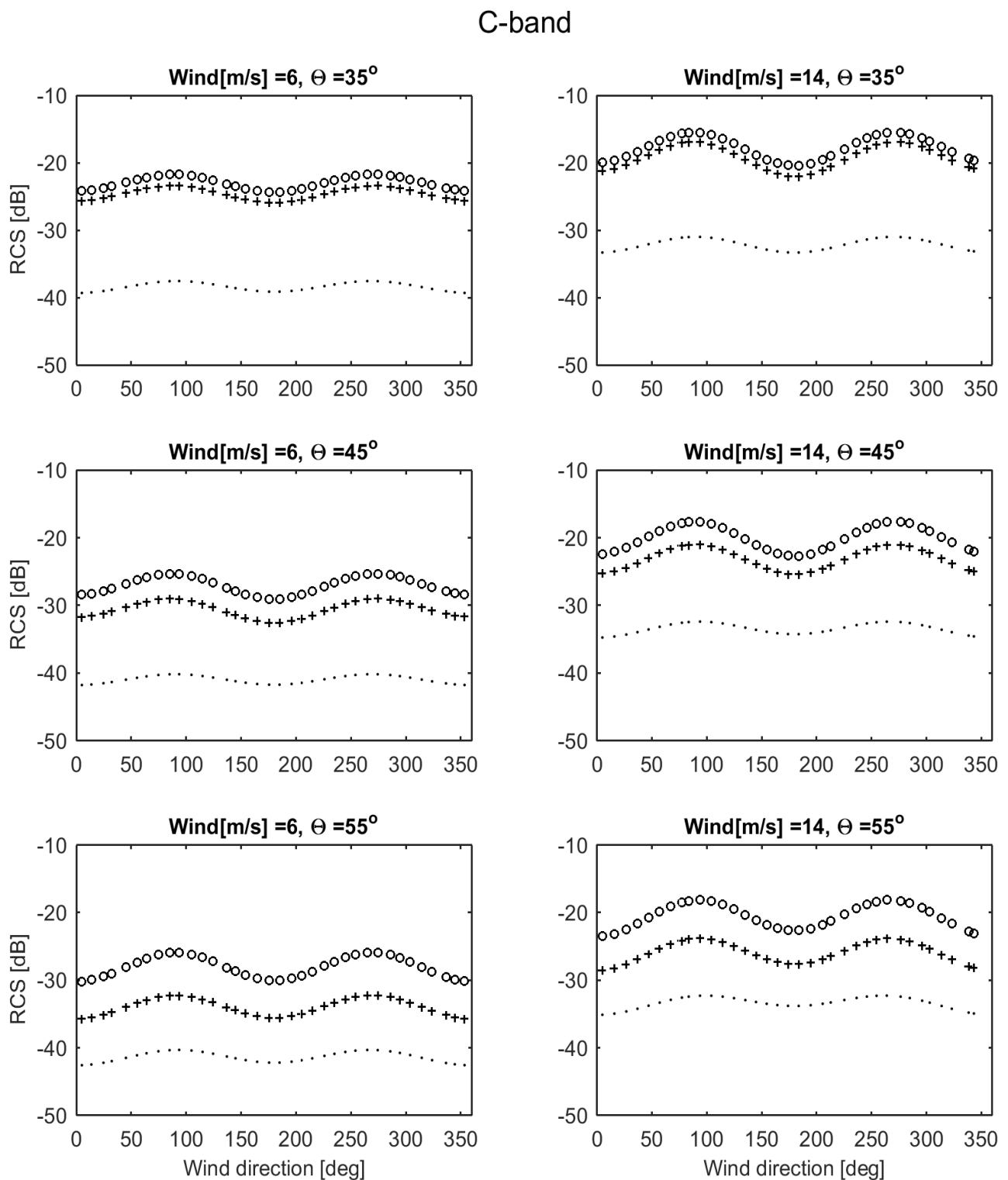


Figure 5.12: Directional signature of C-band radar cross section in VV (circle), HH (plus), and VH (dot) polarizations, for incidence angles of 35° (upper panels), 45° (middle panels), and 55° (lower panels) in two cases of wind speed 6 m/s (left column) and 14 m/s (right column).

Azimuth dependence of polarization ratio

The different upwind-downwind and upwind-crosswind asymmetry of the VV and HH RCS lead to a directional dependence of the polarization ratio. The anisotropy of the polarization ratio at different radar settings and wind speed is shown in Figures 5.13 (for C-band) and 5.14 (for L-, S-, and X-band). We clearly observe the modulation of polarization ratio with wind direction. The maximum value of PR is observed in downwind direction, the second maximum is found in upwind direction and the minimum values are found in crosswind direction. This is different from the directional dependence of RCS, which shows a similar maximum for both up and downwind.

From Figure 5.13 C-band PR shows a strong upwind-downwind and upwind-crosswind asymmetry at low wind speed, showing the strength of the C-band HH to quantify the surface roughness of the different scale especially at low wind. The directional dependence of L-band PR at low wind speed is weak. At high wind speed, directional dependence is clear for all microwave frequencies however X-band shows the clearest trend. For all wind speeds, PR shows a stronger dependence on azimuth direction in steep incidence angle (35°). The directional dependence of the polarization ratio may explain the anisotropy of non-Bragg scattering parts of the total radar backscatter (see Section 3.1, equation 3.5). Therefore, the upwind-downwind asymmetry of PR implies the impact of the non linear wave-wave interaction on non-Bragg parts of the sea surface.

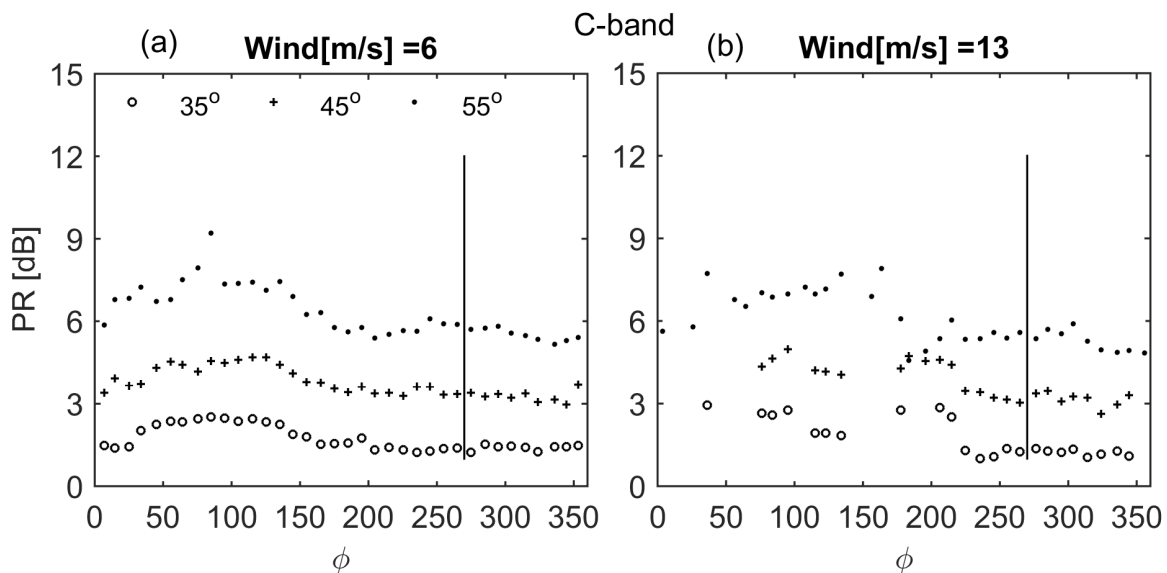


Figure 5.13: Directional dependence of C-band polarization ratio, for incidence angles of 35° (circle), 45° (plus), and 55° (dot) in two cases of wind speed a) 6 m/s and b) 13 m/s . The vertical bar indicate the upwind direction.

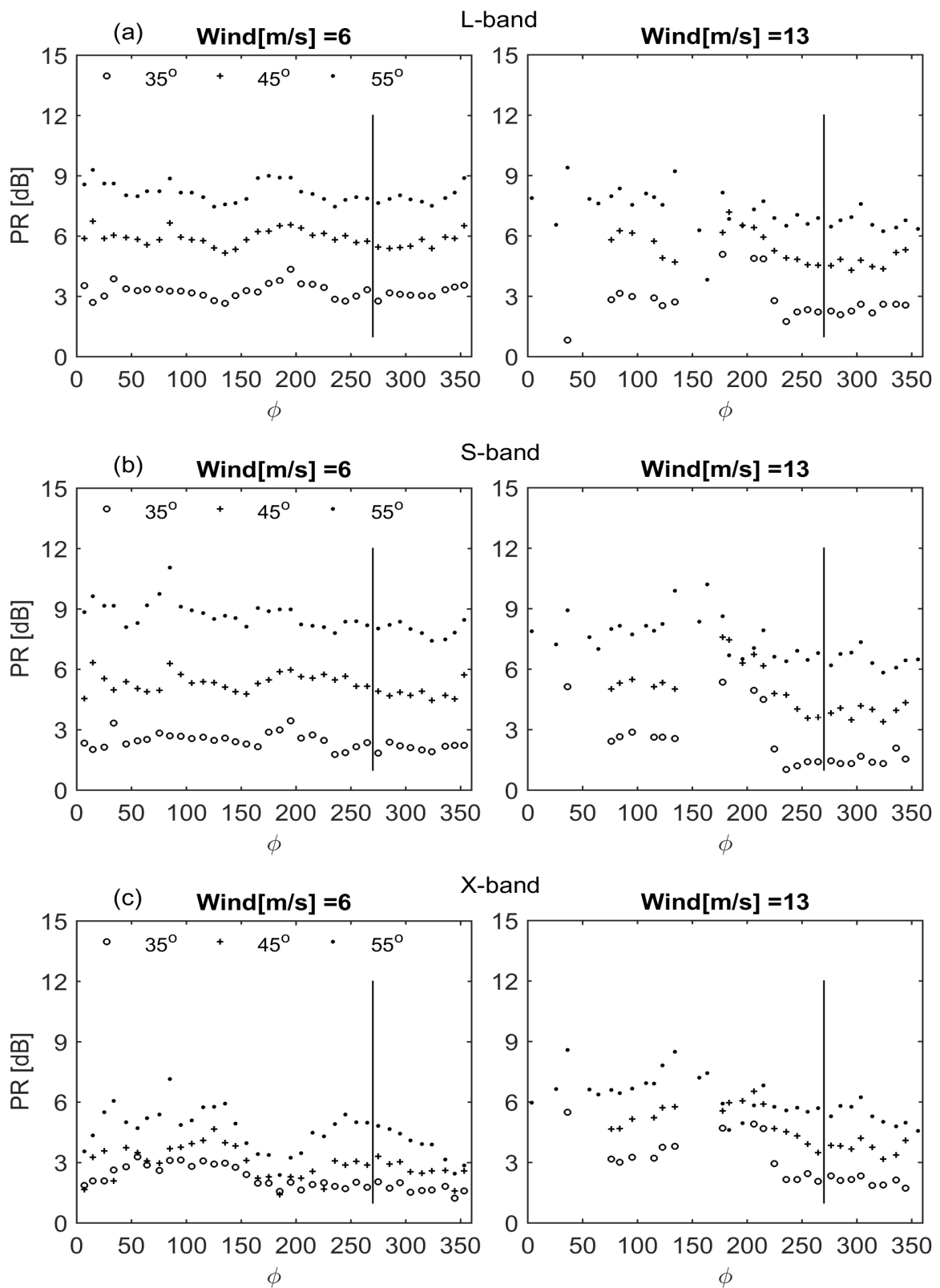


Figure 5.14: Directional dependence of a) L-band, b) S-band, and c) X-band polarization ratio, for incidence angles of 35° (circle), 45° (plus), and 55° (dot) in two cases of wind speed 6 m/s (left panel) and 13 m/s (right panel). The vertical bar indicate the upwind direction.

5.2.3 Effect of atmospheric stability

We examine the radar cross section variation in presence of different atmospheric stratification. Long-term in-situ observation makes it possible to study the influence of atmospheric stability on radar backscatter from the sea surface. The atmospheric stability is considered unstable when the air minus sea surface temperature is negative (negative air-sea temperature difference corresponds to air colder than water) and considered stable when positive value for air minus sea surface temperature is noted. In unstable condition, vertical mixing caused by turbulence turn the wind profile to more uniform with height. This process changes the stress on the sea surface and thus gives rise to higher surface roughness, thereby causing stronger radar backscatter. Figure 5.15 shows the radar backscatter dependence on air-sea temperature difference at different microwave bands and different wind speed. Higher frequency shows more sensitivity of radar backscatter to air-sea temperature difference and shows stronger radar backscatter at the unstable atmospheric condition. However, the impact of the air-sea temperature difference on radar backscatter is noticed during low wind speed. The higher microwave frequency is more sensitive to air-sea temperature difference at all wind condition. The same analysis is done for different radar polarization and VV polarization shows the strongest sensitivity to temperature difference changes.

In order to detect the impact of the atmospheric stability on radar backscatter sensed by Multi³Scat, the difference between Multi³Scat and CMOD5-retrieved radar backscatter on seasonal timescale are displayed in Figure 5.16. The curves show the daily averaged RCS difference over two years at different months. Positive value means that the CMOD5 value is larger than the Multi³Scat observation. The data are time-averaged over the measurements period, providing one value every day.

Remarkable is the systematic bias ranging from 5 dB at 55° to 10 dB at 35° between two data sets which varies at different months. However, the tendency of the two data sets is similar. The standard deviation (STD) and root-mean-square-error (RMSE) in time over the period of the measurements are computed (also for each month). The seasonal variation of the difference between model and observation is assumed to be due to the influence of the other environmental parameters on the sea surface roughness which modify the radar backscatter measured by Multi³Scat and can not be completely explained by the model. In January the wind speed is the dominant factor controlling the sea surface and radar backscatter from both observation and model, therefore reduce the bias. In May the atmospheric condition is stable, makes a calm sea surface in presence of low wind. In this condition, surface films can influence the radar backscatter from Multi³Scat which can not be considered in model and enhances the bias. However, in September, the unstable atmospheric

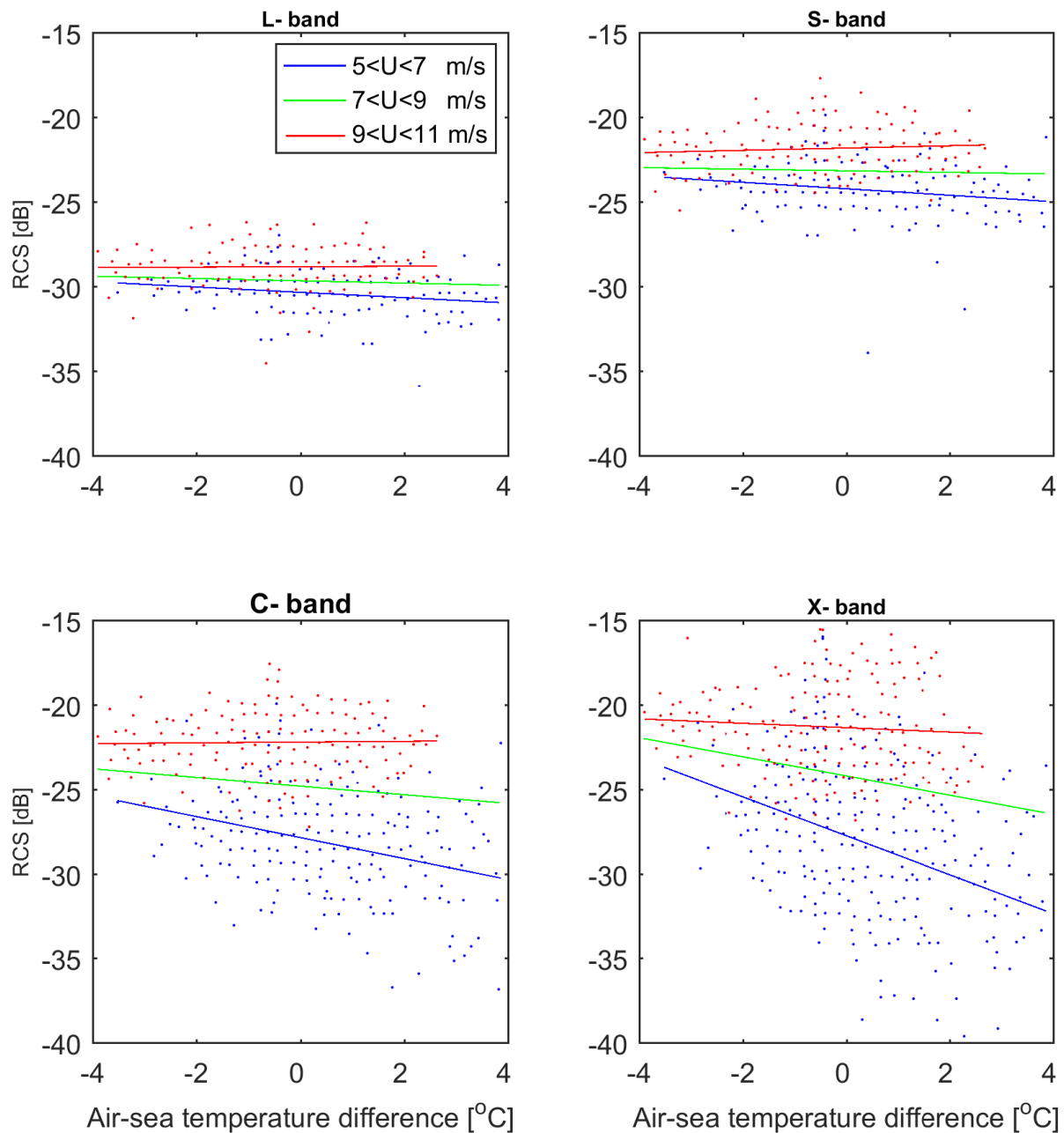


Figure 5.15: The impact of the atmospheric stratification on C-band radar backscatter in VV polarization, upwind direction, and wind speed ranges of 5 m/s to 7 m/s in blue, 7 m/s to 9 m/s in green, and 9 m/s to 11 m/s in red. Different panel presents different microwave frequencies. Negative air-sea temperature difference corresponds to the unstable atmospheric condition and positive air-sea temperature difference indicates the stable atmospheric condition.

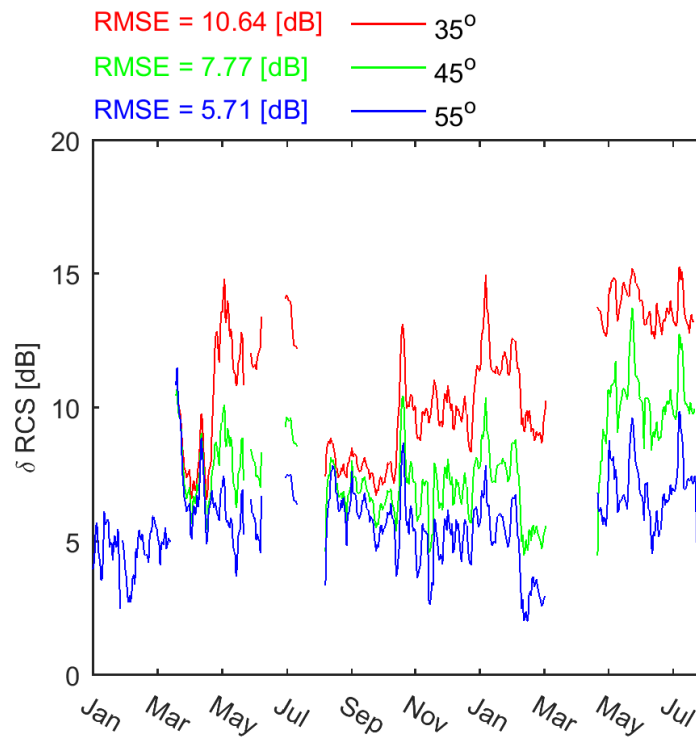


Figure 5.16: Seasonal variation of the daily averaged radar cross section difference between the Multi³Scat observations and CMOD5 value over two years (from January 2012 to August 2013), for different incidence angles; 35° (red), 45° (green), and 55° (blue).

condition makes a complex system in the interface, enhance the surface turbulence and reduces the bias. A detailed analysis of this difference at individual months with respect to the atmospheric stability is presented in Appendix A.4 (see A.4).

The bias between observations and model output is less at a shallower incidence angle (55°) than at steeper incidence angle (35°); about 5 dB for all months. As shown in Figure 5.3, the radar backscatter calculated by CMOD5 is in close agreement with our observation for incidence angle 55° with the bias less than 5 dB, but it significantly overestimates the radar backscatter at small incidence angles.

Figure 5.17 displays the radar backscatter as a function of wind direction at different atmospheric conditions; unstable (red circles) and stable (blue circles). The data points are averaged over 10 degrees wind direction and in the wind speed ranges between 5 m/s to 7 m/s. This wind speed range is considered as a consequence of the output of Figure 5.15. A difference about 2 dB is noted in upwind and downwind direction. However, in crosswind direction the values of unstable and stable atmospheric conditions are very close. From Figure 5.17, we conclude that the impact of the atmospheric stability in radar backscatter from the sea surface observed by Multi³Scat in low to moderate wind speed, upwind and

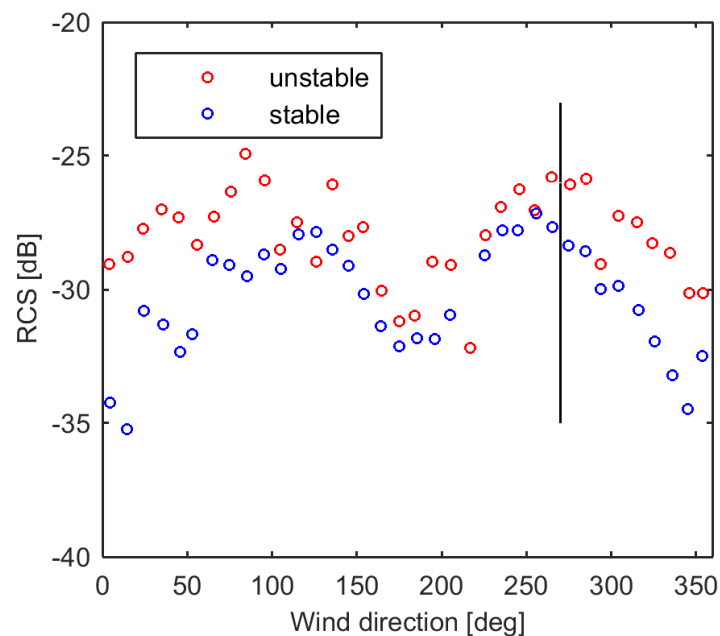


Figure 5.17: C-band radar backscatter as a function of wind direction at unstable (red) and stable (blue) atmospheric conditions.

downwind direction, and higher microwave frequencies (C- and X-bands).

5.2.4 Wave parameters impact on radar backscatter

The significant wave height, H_S is a parameter used to describe sea state. H_S is directly determined from the standard deviation of the spatial-temporal wave elevation which characterizes the state of the sea surface. Furthermore, significant wave height is correlated to the wave breaking through its relationship to wave steepness, thus the correlation between the RCS and PR with wave parameter help to an in-depth analysis of the influence of surface wave and wave breaking on radar backscatter. To make inference about the radar parameters at different surface roughness scale, we repeated the analysis that was done for wind speed but for wave parameter. Thus, we estimate the deviation of RCS and PR at different radar observation setting with respect to H_S . Figure 5.18 represents the relation between RCS and significant wave height in HH-RCS and upwind direction. Each panel represents the different radar frequency with respect to wave parameter. A good correlation 0.80 is calculated for this relationship. Regarding the sensitivity analysis, L-band radar cross section shows a smaller slope in all incidence angles, however the sensitivity to the wave parameter increase

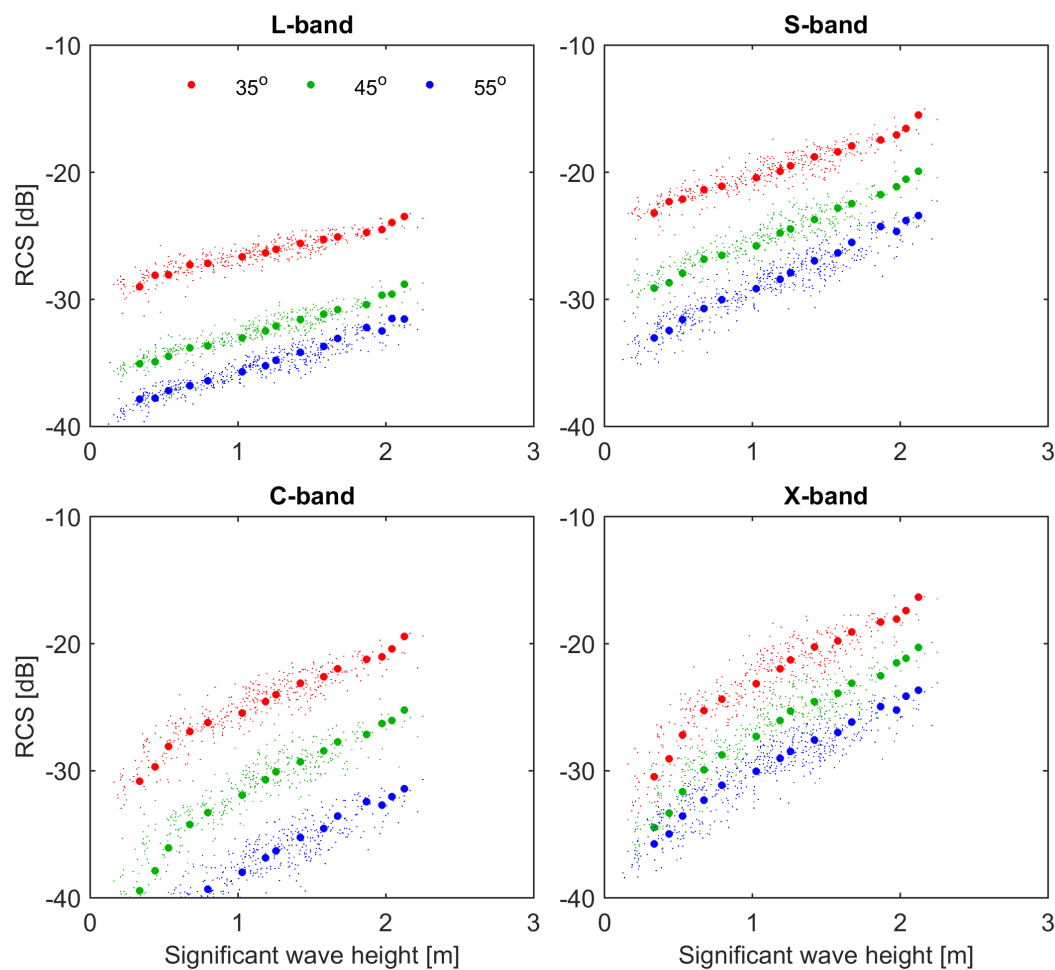


Figure 5.18: Radar cross section versus significant wave height in upwind direction, horizontal polarization, and incidence angles 35° (red), 45° (green), and 55° (blue). The small dots show the observations and the circles show the averaged values over 20 centimeters of wave height.

at higher microwave frequencies. Comparison between different polarization combinations show that cross polarizations sensitivity to significant wave height is incidence angle independent especially at higher frequency bands (C- and X-band) and its regression coefficient is greater than that of the co polarizations.

The directional dependence of the radar backscatter with respect to low wave height and high wave height at different radar settings are investigated. We compare the impact of the different wave height on radar backscatter at moderate wind speed (10 m/s to 11 m/s). Figure 5.19 shows the representative example for C-band. The comparison in Figure 5.19 shows about 1-2 dB differences from low significant wave height to high significant wave height which is more clear at 45° incidence angles. The upwind-downwind and upwind-crosswind anisotropy are clearly noticed in HH-RCS of about 4 dB. This difference is more

clear in HH-RCS and increases at X-band radar backscatter.

From Figure 5.19 the strong dependence of PR on significant wave height might be explained by the impact of larger waves and wave breaking on the RCS, meaning that the signature of the wave height is visible in non-polarized parts of the signal which is dominated by the wave breaking. This result is visible in HH-RCS more than the other polarizations.

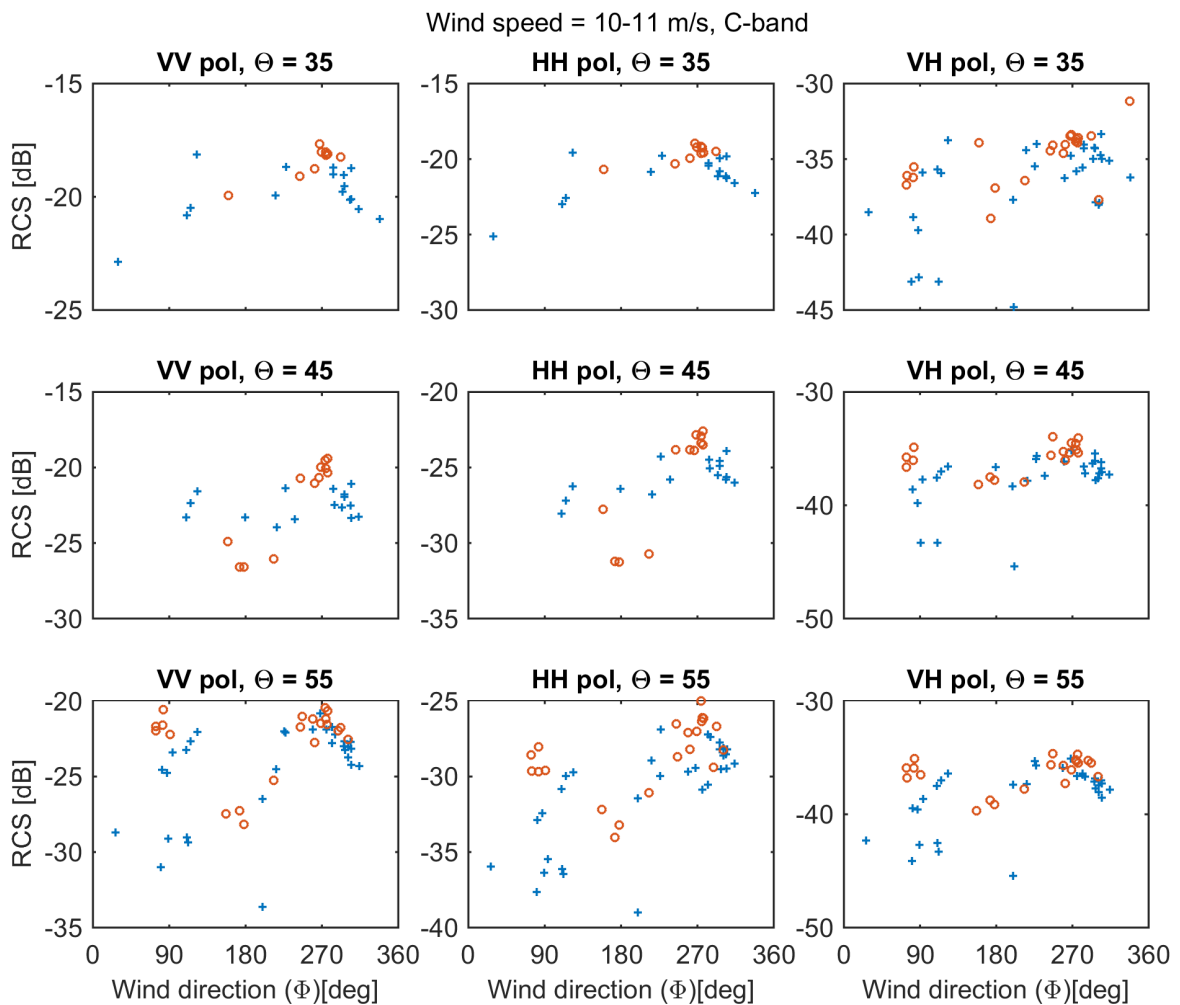


Figure 5.19: Directional dependence of RCS in low significant wave height (blue plus) and high significant wave height (red circle), at 35° (upper panels), 45° (middle panels), and 55° (lower panels), in VV-RCS (left), HH-RCS (middle), and VH-RCS (right).

5.3 Concluding remarks

The combination of different radar observation settings (frequency, polarization, and incidence angle) provides us a unique measurement spectrum (from 20 to 515 rad/m or 1 to 30 cm) in the scale relevant for gas transfer study. Comparing the backscatter from full spectrum allowed us for the first time to statistically discuss the sea surface roughness of different scales in the Western Baltic Sea. Especially, observations over long period of time, helped us to discuss the temporal statistics of the sea surface roughness in presence of the different surface/interface conditions.

The quality of the radar cross section (RCS) is assessed with respect to the scattering theory, and the results of C-band RCS are compared with the C-band geophysical model function (CMOD5).

The larger underlying gravity waves do not directly influence the microwave scattering over the ranges of wavenumber 20 to 515 rad/m Hwang [2005] and Bock et al. [1999]. However, they carry the shorter capillary waves and modulate the amplitude and frequency of the Bragg scatterers based on the tilt patches of scatterers. This significant characteristic of the scatterometer backscatter is identified by using the combination of radar backscatter at different incidence angles.

The different sensitivity of HH polarized RCS to the angular variation especially at low wind condition, is noticed from the trend line slope in HH polarized RCS comparing to that of VV polarized. It is caused by the different aspect of the combination of HH-RCS and shallow incidence angle to sense the low wave amplitude at low wind speed. At low wind speed, the waves are shorter with lower amplitude compared to the high wind condition, which leads to a stronger reduction in the backscatter intensity when the incidence angle increase. The average difference between high wind to low wind angular dependence in HH-RCS is about 7 dB and in VV-RCS is about 2 dB. The cross-polarization RCS show a downward trend with increasing incidence angle but with rather a small variability at S-band and C-band for a given sea state, which means that VH-RCS are essentially independent of incidence angle.

A different trend line slope is noticed between CMOD5 and Multi³Scat RCS, meaning the different sensitivity of the Multi³Scat RCS to the angular variation than that of the model. It shows that RCS at different incidence angle senses the different scale of the surface roughness modified by the impact of other interface parameters rather than wind speed. The combination of these parameters can not be considered in the CMOD5 RCS.

The non-Bragg parts of the signal which is dominated by the contribution of wave breaking and steep waveforms are studied using polarization ratio ($PR = \frac{VV}{HH}$). [Kudryavtsev et al.,

2003; Romeiser et al., 1997]. From the PR angular dependence, S-band and C-band RCS are considered as the proper radar frequencies for quantifying the impact of the wave breaking and steep waveforms.

For a more in-depth analysis of the behavior of different radar observation settings regarding the sensitivity of the RCS to wind speed changes, the slope of the RCS-wind dependence is studied with respect to the frequency changes at different polarizations. We noticed a different behavior of X-band radar frequency in HH and VH-RCS but not in VV-RCS. Higher microwave frequency is subject to changes by the impact of very short waves, which at high wind condition and very rough surface in presence of large scale wave breaking, leads to a different behavior of the backscatter intensity. The contribution of the wave breaking is more in HH and VH than in VV caused a falls off in the slope of the RCS-wind dependence only in HH and VH high-frequency band (X-band). This result will be further considered in gas transfer analysis.

Long-term observation with tower mounted scatterometer makes it possible to analyze the azimuthal dependence of the radar backscatter at different air-sea interface conditions. The variation of the radar cross section as a function of azimuth angle (angle between wind direction and radar look direction) is a characteristic explained by the anisotropy of the energy density of the short Bragg waves. Upwind to downwind asymmetry is the consequence of hydrodynamic modulation of short waves which are carrying by the longer underlying waves [Kudryavtsev et al., 2003; Romeiser et al., 1997]. The upwind to crosswind asymmetry of the radar backscatter is due to the angular distribution of the wave height spectrum [Kudryavtsev et al., 2003]. At high wind speed, the RCS dependence on azimuth is higher at higher incidence angles (55°). Comparing the different frequencies, higher microwave band shows a large upwind-crosswind asymmetry at all incidence angles and wind speeds. This change is slightly larger in VV-RCS than in HH-RCS, hence the polarized part of the backscatter which is controlled by the Bragg resonance dominates the upwind-crosswind asymmetry and is visible in VV polarization-shallow incidence angle radar backscatter [Mouche et al., 2006]. At high wind speed, the wave breaking contribution in the total signal is more than Bragg resonance, effect small changes in upwind-crosswind asymmetry with incidence angle changes.

The sensitivity of the radar backscatter to the atmospheric stability is studied using air-sea temperature difference as a stability parameter. The impact of the air-sea temperature difference on radar backscatter is noticed during low wind speed. However, the higher microwave frequency and VV-RCS shows more sensitivity to air-sea temperature difference at all wind condition.

We studied the sensitivity of the radar backscatter to the changes of the significant wave

height as a parameter describing the sea state. The moderate wind speed (10 m/s to 11 m/s) were used to study the behavior of radar backscatter in presence of low and high significant wave height. The experimental observations indicate that the difference between low and high significant wave height is about 1 dB to 2 dB at 45° incidence angle and this deviation increases in HH polarization and X-band microwave frequency. Cross polarization shows a better regression and more sensitivity to the wave height changes and less sensitivity to the different incidence angles. The cross polarizations data are essentially independent of incidence angle and wind direction. This suggests the advantage of cross-polarization signals regarding the sea surface roughness quantifying, without the knowledge of the wind direction and local incidence angle, and for sufficiently high wind speeds.

Confirmed here is that the Multi³Scat observations provide useful information on the sea surface signatures of the contribution of the different components influencing sea surface roughness and so that the air-sea gas exchange rate.

CHAPTER 6

Air-Sea CO₂ exchange and radar backscatter

In the previous chapter, we qualified the Multi³Scat observations in order to provide quantitative information on sea surface signatures due to the contribution of different components influencing sea surface roughness. The combination of different radar observation settings (frequency, polarization, and incidence angle) helped us to understand the surface properties which influence the radar response. The results can further be used to quantitatively better estimate the air-sea gas transfer velocity.

In the following, we apply the CO₂ flux observation from the eddy covariance method performed in the Western Baltic Sea to the existing algorithm and compute the gas transfer velocity. Furthermore, the CO₂ transfer velocity and flux are examined by combining in situ observations and scatterometer measurements of the sea surface roughness. The correlation between CO₂ transfer velocity and radar backscatter will result in a new parameterization of air-sea gas transfer velocity.

6.1 CO₂ flux and transfer velocity analysis

The daily averaged seasonal cycle of the CO₂ mass flux, the atmospheric CO₂ density, and the partial pressure of CO₂ in the air and seawater during the experiment in 2011 and 2012 are shown in Section 4.3.4 (see Figure 4.11). The time series of CO₂ flux has maximum value of 0.15 mg/m^2s which occurs during winter. The negative sign indicates the direction of the flux from the atmosphere to the ocean. The atmospheric CO₂ density and oceanic partial pressure of CO₂ clearly show a seasonal cycle which is caused by the difference in air density during different seasons, and biological productivity during the summer time, respectively. The atmospheric partial pressure of CO₂ does not change in comparison to that of the ocean. A strong CO₂ flux (shown in Figure 4.11) is detected during the winter in the presence of very weak air-sea P_{CO₂} difference, which means that in the case of high wind speed and rough sea surface (possible during the winter time), the flux is likely controlled by

surface wind speed and sea surface roughness. Here, we use time-averages over the period of the experiment, providing values of 1-hour data which helps to avoid of noise while with bin averaging we smooth the data to avoid spikes. However, the flux data presented in this study are filtered to remove the spikes due to system failure.

The first attempt is made to obtain the CO₂ transfer velocity directly from the CO₂ flux observation and CO₂ partial pressure difference by using the inverse of equation 1.1 (described in Section 2.2):

$$\kappa = \frac{F_{CO_2}}{\alpha \Delta P_{CO_2}} \quad (6.1)$$

The transfer velocity κ can be converted to the normalized transfer velocity κ_{660} by using the Schmidt number (calculated from the equation 2.6 Wanninkhof [1992], Section 2.3), as:

$$\kappa_{660} = \kappa \left(\frac{Sc}{660} \right)^{-0.5} \quad (6.2)$$

In order to filter and smooth the data to avoid spikes due to instruments failure, which influences the final results, we exclude the flux data over the range of averaged value \pm standard deviation. Because of the seasonal cycle of the CO₂ flux as well as the other data sets, we applied seasonal adjustment to filter the data. The averaged value \pm standard deviation is calculated for each month over the period of observation. We exclude the CO₂ flux data that were higher than the value of the average \pm standard deviation for further analysis.

During the winter time, a strong flux in the presence of very small partial pressure differences causes unrealistic huge transfer velocities caused by the fraction in the equation 1.1. We assume that during winter time, the CO₂ flux is mostly controlled by wind speed. Furthermore, besides the wind speed, the air-sea temperature difference during the winter is higher, which causes more turbulence in the air-sea interface (Figure 4.9). The density correction term for the CO₂ flux (see [Webb et al., 1980]) mainly depends on the ratio of turbulent fluctuations of CO₂ concentration to its mean concentration (see Section 4.3.4).

Because the CO₂ flux over the sea has small values in comparison to the other fluxes such as sensible and latent heat flux, it's turbulent fluctuations are also small; therefore, the CO₂ density correction can have the same value as the CO₂ turbulent flux [Garbe et al., 2014a]. The density correction by Webb et al. [1980] considered the first order correction. To exclude the uncertainty caused by the impact of first order Webb correction in the flux data, we exclude the CO₂ fluxes which were affected by sensible or latent heat fluxes that were higher than a factor of 10. The sensible and latent heat flux were measured in parallel with the CO₂ flux, and their flux velocities can be calculated by dividing the surface flux with the corresponding density. This method is used in the study by Weiss et al. [2007], which

was done in Arkona basin in the Baltic Sea.

Figure 6.1 represents the wind-averaged CO₂ transfer velocity over the 10-month period from November 2011 to August 2012, providing one single value for every 0.5 m/s wind speed. The transfer velocity is computed from Equation 6.1 using observations in the Western Baltic Sea (see Section 4.3). In Figure 6.1, 80 % of the transfer velocity values are below 10 m/s wind speed and in the y-axis the interval between 100 and 300 cm/h contains less than 5% of the values, which are mostly at moderate wind speed.

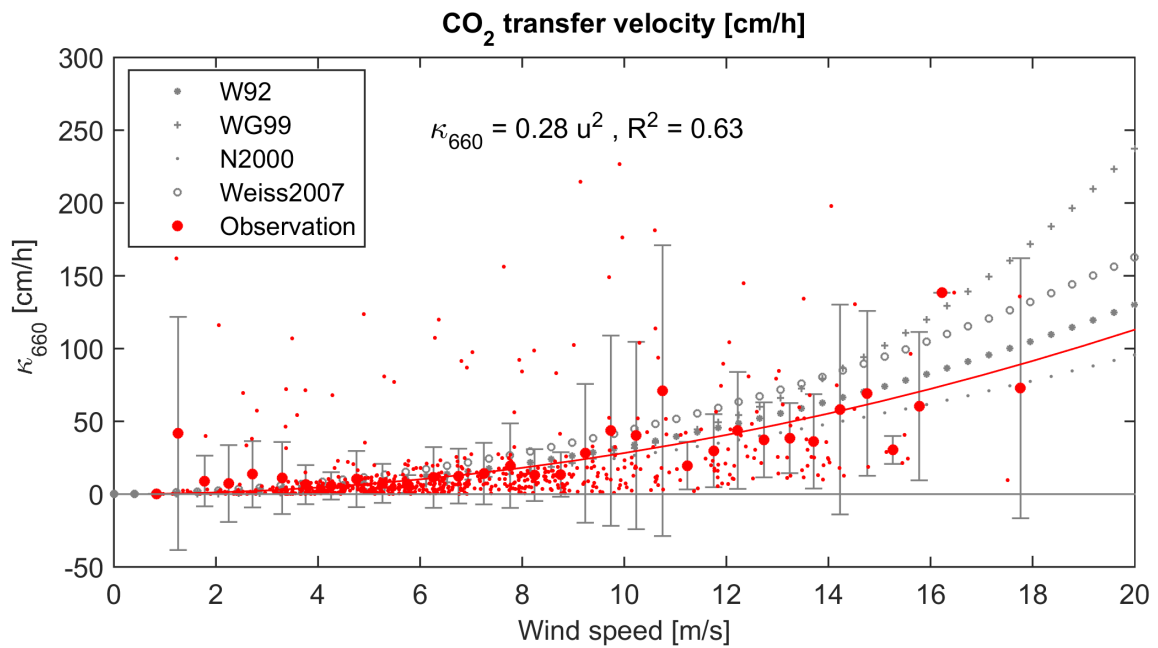


Figure 6.1: CO₂ transfer velocity [cm/h] normalized with Sc number versus wind speed, from direct eddy covariance measurements in the Western Baltic Sea (red dots). Averaged value of transfer velocity over 0.5 m/s classes of wind speed are shown in red filled circles. The error bars correspond to standard deviations of each window. The curves with gray patterns describe model results of Wanninkhof [1992] (star), Wanninkhof and McGillis [1999] (plus), Nightingale et al. [2000] (dot), Weiss et al. [2007] (circle).

From observations in the Western Baltic Sea (shown in Figure 6.1 with red dots), we fit the data using a quadratic dependence between the gas transfer velocity and wind speed with higher correlation factor rather than the other power function forms (the red line in the Figure 6.1) to obtain the empirical relation:

$$\kappa_{660} = 0.28U^2 [cm/h] \quad (6.3)$$

The correlation factor of our empirical relation is $r^2 = 0.63$, affected by the very scattered data points at moderate wind speed, very fewer data points at high wind speed and a moderate range of CO₂ flux at low wind speed during the winter time.

To assess the performance of our gas transfer parameterization, we compare it with the traditional transfer velocity parameterizations introduced in Table 2.1. From Figure 6.1, a similar trend and value for all the parameterizations is noticed for the wind speeds up to 10 *m/s*. The deviation between the different parameterizations starts from about a wind speed of 10 *m/s* and increases with wind speed, meaning that the most uncertainty in gas transfer estimation comes from moderate to high wind speed. The reason might be due to the influence of the other sea surface parameters we discussed in Chapter 5.

Comparing with the other models, the transfer velocity of our study at moderate wind speed shows a similar distribution as shown in Weiss et al. [2007]; however, at higher wind speed our data show the fitted value between the results of Nightingale et al. [2000] and Wanninkhof [1992]. From Figure 6.1, it is clear that for wind speed greater than 10 *m/s* there is a wide discrepancy as a result of different gas transfer parameterizations. The scaling factor of the gas transfer parameterization proposed from observations in the Western Baltic Sea (0.28) shows a close value to the scaling factor proposed by Takahashi et al. [2009] (0.26), and Wanninkhof [1992] (0.31).

To provide a statistical assessment, a Taylor diagram is presented in Figure 6.2. The diagram displays the correlation coefficient, the standard deviation, and the root-mean-square deviation of the different gas transfer models introduced in Table 2.1 relative to the gas transfer from observation. The same data which are used in Figure 6.1 are applied to the diagram. The correlation coefficient is shown with blue dashed lines. The standard deviation is represented by gray dashed lines, and green dashed lines correspond the root-mean-square difference. From the diagram, the gas transfer velocity of Nightingale et al. [2000] is closest to observations with a standard deviation of 16 *cm/h*, a root-mean-square difference of 10 *cm/h*, and a correlation coefficient of 0.89. The second closest is from the parameterization of Wanninkhof [1992] with a standard deviation of 22 *cm/h* and nearly the same root-mean-square difference and correlation coefficient as Nightingale et al. [2000]. For Weiss et al. [2007] and Wanninkhof and McGillis [1999] root-mean-square differences reach values of about 14 and 19, and standard deviations of 28 and 35, respectively.

In summary, the assessment based on time series of different wind-based parameterizations and computed gas transfer velocities from observations shows that the datasets are in good correlation, but large differences can be found which comes mostly during moderate to high wind speed. The disagreement between the parameterizations and observations can be caused by various factors and will be discussed further in detail.

The next attempt is made to reproduce the CO₂ flux on the basis of the equation 1.1, by using the measured P_{CO₂} and calculated solubility α (from Weiss [1974]), and using our transfer velocity parameterization 6.3.

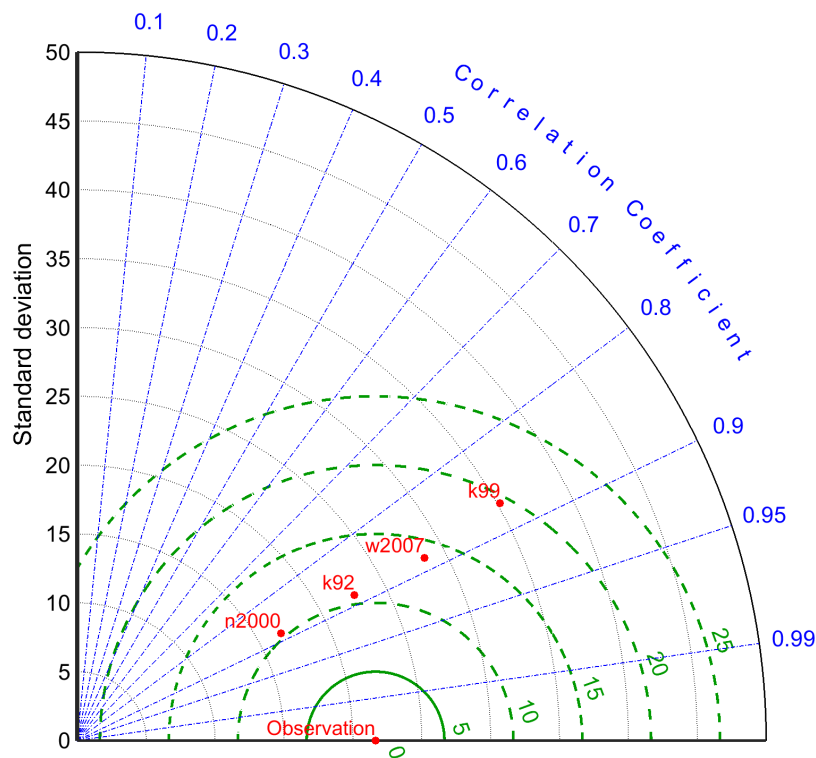


Figure 6.2: Taylor diagram of gas transfer models of Wanninkhof [1992] (k92), Wanninkhof and McGillis [1999] (k99), Nightingale et al. [2000] (n2000), Weiss et al. [2007] (w2007) compared to the gas transfer computed from observations in the Western Baltic Sea.

Figure 6.3 presents the comparisons between the CO₂ flux from observations in the Western Baltic Sea and the fluxes calculated using the transfer velocity-wind speed parameterizations introduced in Table 2.1 in combination with Equation 1.1 for the all observations (November 2011 to August 2012). The flux computed using Equation 1.1 has a unit of $\frac{\mu\text{mol}}{\text{m}^2\text{s}}$; therefore, for the rest of analysis, we convert the flux observation unit from $\frac{\text{mg}}{\text{m}^2\text{s}}$ to $\frac{\mu\text{mol}}{\text{m}^2\text{s}}$ to be comparable with the other studies. The CO₂ flux calculated by using the Nightingale et al. [2000] parameterization has better agreement with observations in both the mean and seasonal variability than the other parameterizations introduced in Table 2.1, with a root mean square error of $0.28 \frac{\mu\text{mol}}{\text{m}^2\text{s}}$.

From Figure 6.3, the stronger observed flux during winter in the presence of very small partial pressure differences is noticeably different compared to that of spring and summer, which have larger partial pressure differences. During winter, higher wind speed, unstable atmospheric stratification, and near surface turbulence control the CO₂ flux. The validation

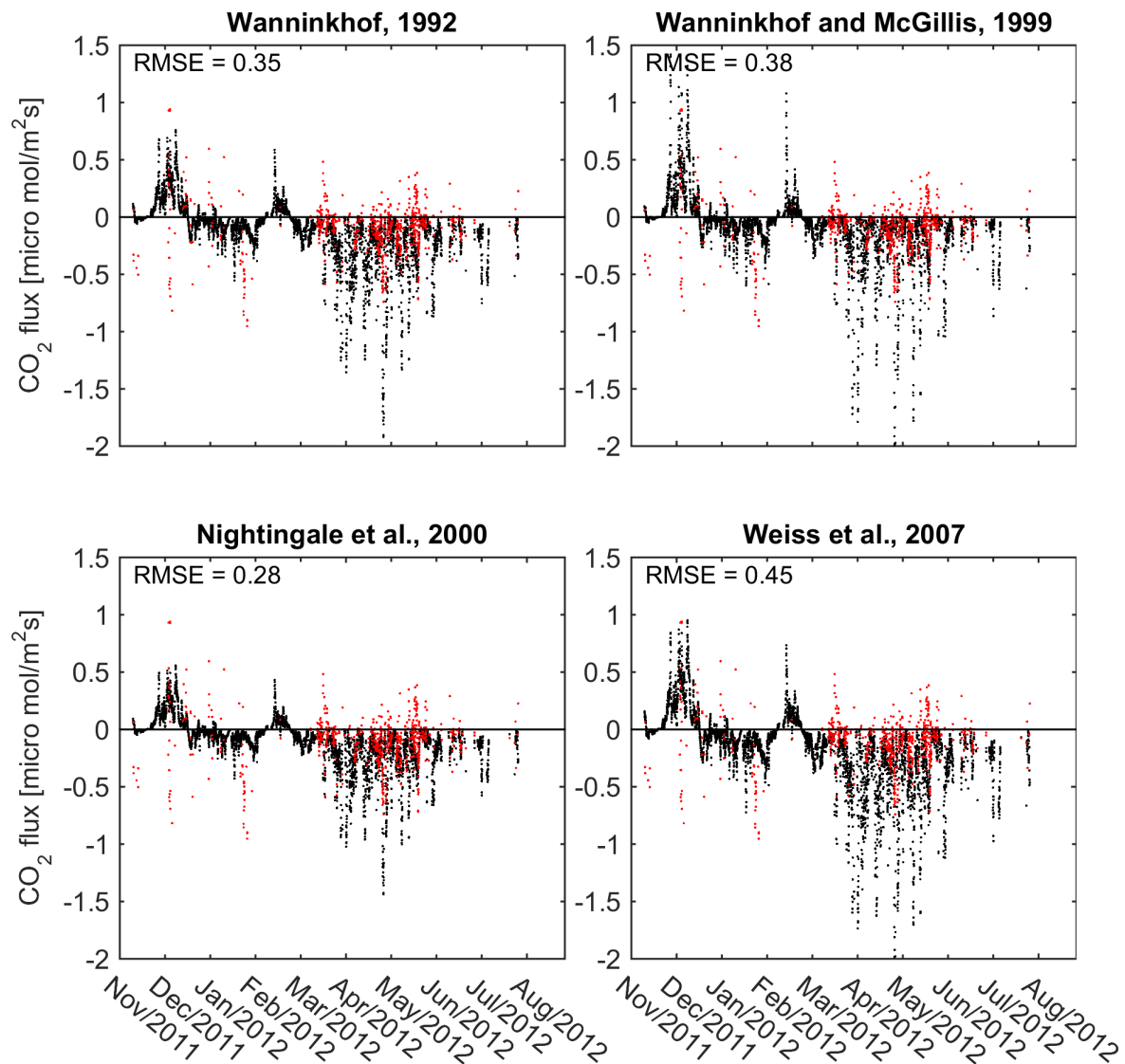


Figure 6.3: Temporal variation of the CO₂ flux from observations (red dots) and four different calculated CO₂ fluxes using the gas transfer parameterizations presented in Table 2.1 (black dots). The data are time-averaged over the period from November 2011 to August 2012, providing one value every hour. The statistical comparison between the datasets are shown by the root mean square error between observations and calculated flux. The closest flux to observations is from Nightingale et al. [2000] with an RMSE of 0.28 $\frac{\mu\text{mol}}{\text{m}^2\text{s}}$.

based on time series of the model parameterizations shows that the computed flux is more influenced by the partial pressure difference rather than by the wind speed and interface parameters. This fact results in the large computed flux during the warm seasons. The direction of the calculated flux is controlled by the sign of the partial pressure difference of CO₂; however, in observations, the vertical advection, surface wave breaking, and near surface turbulence control the flux direction. Therefore, considering the flux direction, correlation

between observations and calculated flux is very low.

In summary, seasonal variations of the CO₂ flux are controlled by biological and physical processes. In spring the surface water is affected by the impact of the atmospheric stability especially at low wind speed (see Section 5.2.3). In March, the surface P_{CO₂} drops as a result of the intensive primary production. The decrease in summer P_{CO₂} is neutralized by the temperature effect in increasing the P_{CO₂}. Therefore, the complex CO₂ flux variation in summer is due to the influence of the temperature in P_{CO₂} reduction. In winter, the effect of atmospheric stability in parallel with the high wind speed, dominate the effect of P_{CO₂} enhancement in the sea water and produce high CO₂ flux. A detailed investigation of the production season in the Baltic Sea was conducted by [Schneider et al. \[2009\]](#).

6.1.1 Seasonal variation of gas transfer velocity

Observations over one year let us discuss the seasonal variation of flux and moreover to compare the differences between observations and computed flux at different seasons, individually. Figure 6.4 (a and b), represent the gas transfer velocity computed from the flux observation in two time-scales; from October 2011 to April 2012 and from April 2012 to October 2012, respectively. The term "cold season" is hereinafter defined as the time-scale from October 2011 to April 2012, and the term "warm season" is defined as the time-scale from April 2012 to October 2012.

Because more data points are available in these two seasons, we combined the data in winter and autumn together as well as in spring and summer. The relation between the gas transfer velocity and wind speed from observations leads to a quadratic function between gas transfer and wind speed, with scaling factor of 0.11 and a correlation factor of $R^2 = 0.84$ in spring and summer (see Figure 6.4 b). Here, the fitted curve at high wind speed is lower than that of any other gas transfer parameterization introduced in Table 2.1. In spring the number of data points is higher than in other seasons and CO₂ flux is not scattered (see the error bars in Figure 6.4 b). In winter, the gas transfer velocity is related to the wind speed in a quadratic relationship with scaling factor 0.42, resulting from the large gas transfer velocity at moderate wind speed, and a low correlation factor of 0.34 due to the scattered data at all wind speeds (see Figure 6.4 a). The gas transfer velocity observations in winter are very close in value to the gas transfer velocities of the [Weiss et al. \[2007\]](#) parameterization.

Since the gas transfer velocity obtained from the models are representative only for the wind speed dependence, any other surface physical forcing can lead to a difference between model retrievals and observation gas transfer velocity. The difference caused by the influence of the combination of several factors such as near surface turbulence, surface waves, wave

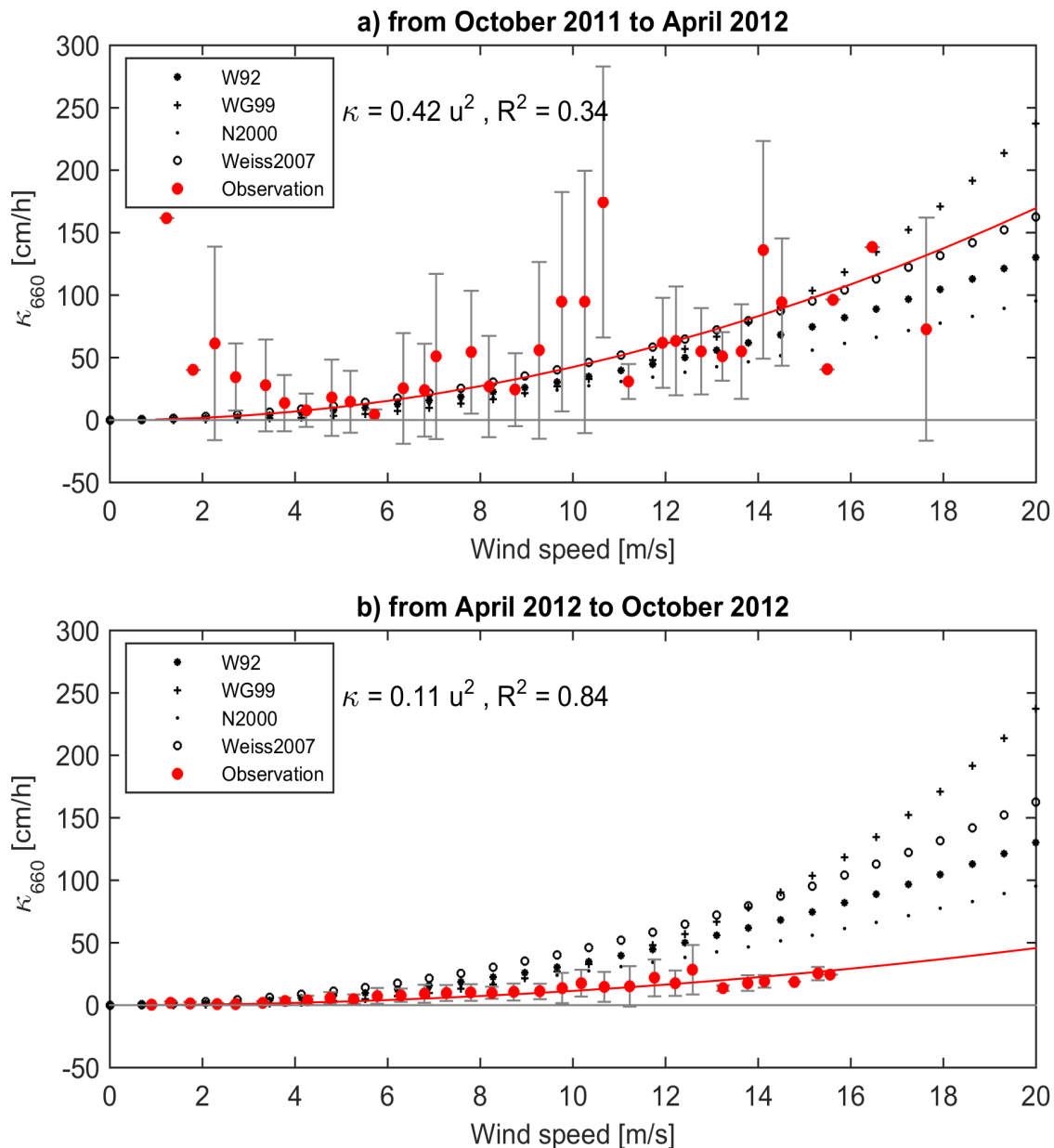


Figure 6.4: Averaged CO₂ transfer velocities [cm/h] normalized with Sc number versus wind speed of $0.5 m/s$ classes, using observations a) from October 2011 to April 2012 and b) from April 2012 to October 2012, using direct eddy covariance measurements in the Western Baltic Sea (red circles). The error bars correspond to standard deviations at each wind class. The curves with black patterns are the outputs of the parameterizations introduced in Table 2.1.

breaking, and surface films [Garbe et al., 2014b]. Moreover, as discussed in Section 5.2.3, the effect of an unstable atmospheric condition, which is dominated at low wind speeds, modifies the sea surface roughness scale and results in a difference between model and observational estimates of gas transfer velocity at low wind speed in winter (see Figure 6.4 a).

The scaling factor of the gas transfer-wind speed relationship in the summer is very close to that in spring, and the autumn value is close to that in winter, and the correlation factor is very low due to the low number of available data. Therefore, we reproduce the flux of CO₂ considering the seasonality of gas transfer velocities, the partial pressure difference of CO₂, and solubility. The reproduced CO₂ flux data are presented in Figure 6.5. High solubility and sea-water P_{CO₂} during the cold months in the presence of unstable atmospheric condition, cause the effect of near surface turbulence to enhance CO₂ flux during the cold months.

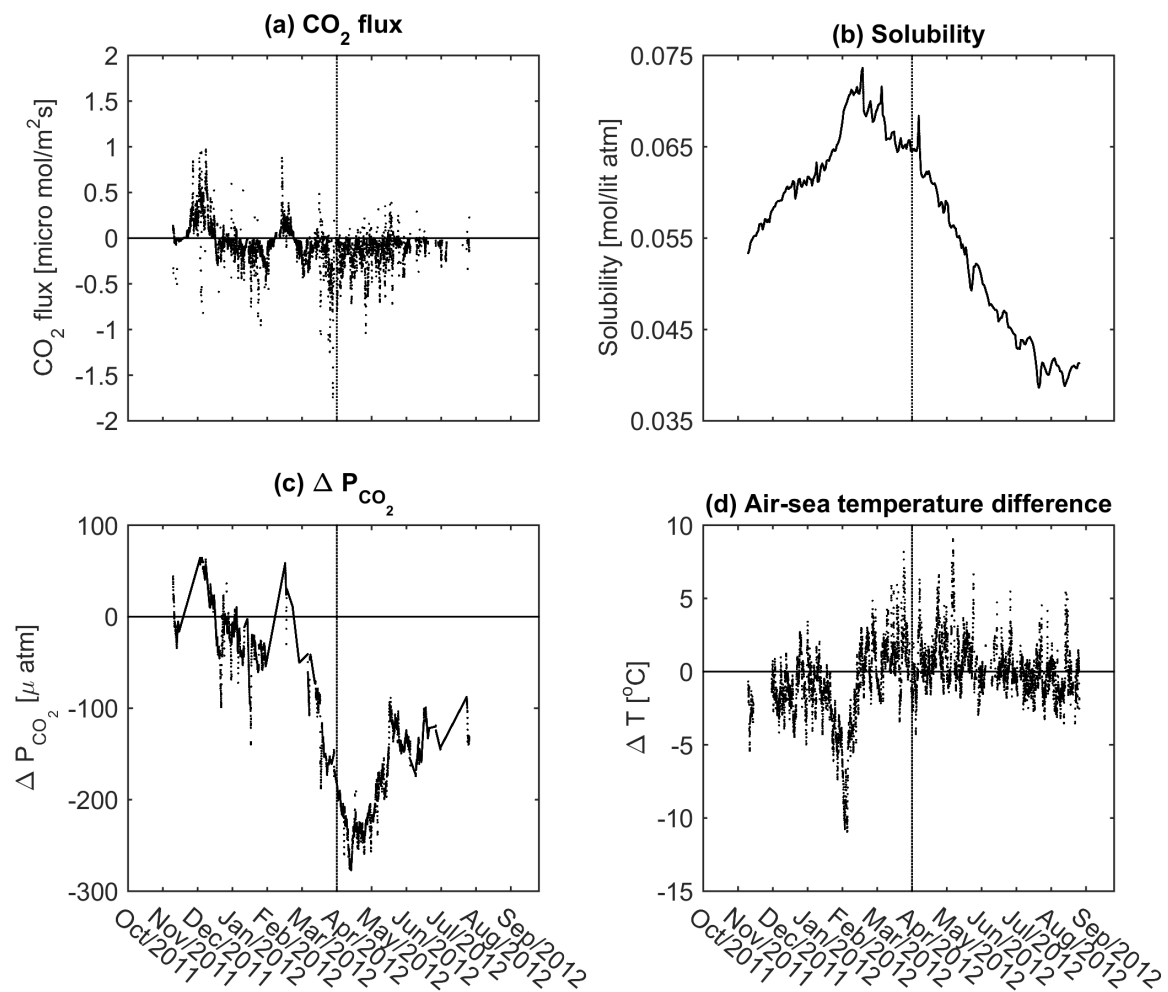


Figure 6.5: The reproduced CO₂ flux data (a) based on the seasonal variation of wind speed, solubility (b), partial pressure difference of CO₂ (c), and air-sea temperature difference (d). Vertical dashed line indicate the season changes with respect to the coefficients used to reproduce CO₂ flux from transfer velocity.

6.2 Flux estimation using Radar observations

A new approach for calculating air-sea CO₂ transfer velocities will be introduced. This correlates with the radar backscatter derived from the tower-mounted microwave scatterometer instead of wind speed only. In principle, this relationship correlates the gas transfer velocity with near surface turbulence and capillary-gravity surface waves. The mathematical basis of the relationship between radar cross section of the sea surface and capillary-gravity wave spectra is studied by Bogucki et al. [2010]; Hwang [2005]; Bock et al. [1999]; Phillips [1988]; Valenzuela [1978]. The reproduced gas flux from the scatterometer radar cross section of the sea surface will be statistically discussed and compared with observations and wind-based parameterizations in the next section.

6.2.1 Algorithm description

The relationship between radar cross section (RCS) from the Multi³Scat and in situ CO₂ transfer velocity in the Western Baltic Sea is obtained in two steps; first relating RCS to the mean square surface capillary-gravity wave slope and second relating mean square slope to the gas transfer velocity. The simple schematic of the algorithm is shown here:

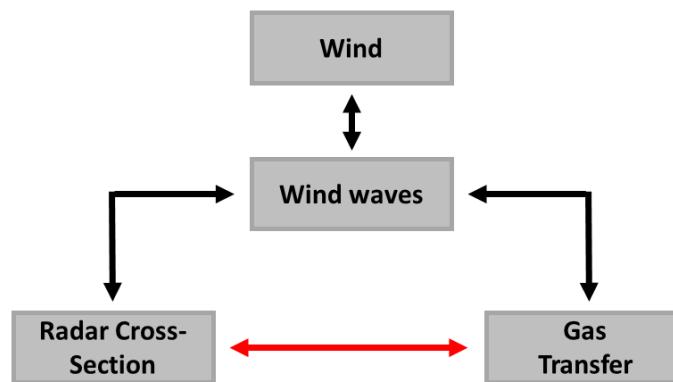


Figure 6.6: The simple schematic of the relationship between radar cross section and gas transfer velocity.

The direct relationship between gas transfer velocity and wind speed is debated in the literature. Elfouhaily et al. [1997] examine different relationships between the wind speed and the mean square surface wave slope. Bock et al. [1999] represent a linear relationship between gas transfer velocity and mean square surface wave slope.

In summary, from observations used in this study, we obtained a quadratic relationship between wind speed and gas transfer velocity (Equation 6.3). We examined the sensitivity

of radar backscatter from the sea surface (by the Multi³Scat) with respect to the surface parameters (wind and waves (observations in the Western Baltic Sea)) (see Chapter 5). From the combination of the radar observation settings (frequency, polarization, and incidence angle), we obtained a unique measurement spectrum, which capable us to make inferences about frequency and polarization dependencies using the full spectrum and furthermore, help us to gain insight into the sea surface roughness characteristics at the scale of interest for gas transfer estimation. In the next section, we examine the direct relationship between radar backscatter and gas transfer velocity both from observations in the Western Baltic Sea.

Scatterometer based gas transfer velocity

The final step of this study is to use the results of the previous sections to relate the upwind radar cross section of the sea surface to the gas transfer velocity. First, we present the correlation between radar data and CO₂ transfer velocity at different seasons (winter and spring), individually. Then we discuss the best parameterization to estimate gas transfer velocity using radar data.

Presented in Figures 6.7 and 6.8 are the relationships between radar backscatter and gas transfer velocity from observations over winter and spring, respectively. The data are averaged over the period from November 2011 to August 2012 for each season and with respect to the wind speed, providing one value every 1 *m/s* wind speed ranges.

There is a slight difference in the dependencies of the VV (red) and HH (blue) polarizations of radar backscatter to gas transfer velocity, which reflects the impact of wave breaking, steep waveforms, and Bragg surface waves on gas transfer velocity. The vertical error bars correspond to the deviation of the gas transfer data with respect to its averaged value.

We fit our data by using a power law dependence and we obtain the empirical relationship in VV and HH polarizations, C-band, radar cross section in upwind direction as below:

$$\begin{aligned}\kappa &= 10^{3.81} \cdot \sigma_{vv}^{1.1} \\ \kappa &= 10^{3.97} \cdot \sigma_{hh}^{0.9}\end{aligned}\tag{6.4}$$

here, σ_{vv} and σ_{hh} are upwind radar cross section in linear scale and κ is gas transfer velocity in *cm/h*. The parameterization in VV polarization yields $R^2 = 0.82$ and RMSE = 10 *cm/h*. The empirically determined coefficients of the RCS based gas transfer velocity from observations are shown in Table 6.1 for S-, C-, and X-band microwave frequencies, and VV, HH, and VH polarizations. The statistics of the relationships for each radar observation settings are summarized in Table 6.1.

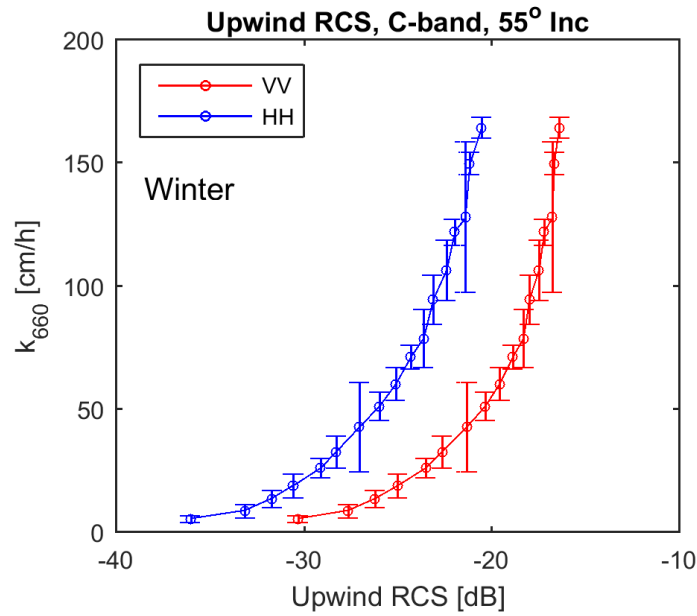


Figure 6.7: Upwind C-band RCS versus observed in situ CO_2 transfer velocity in winter. Data are averaged over the measurements period, providing one single value for every 1 m/s wind speed.

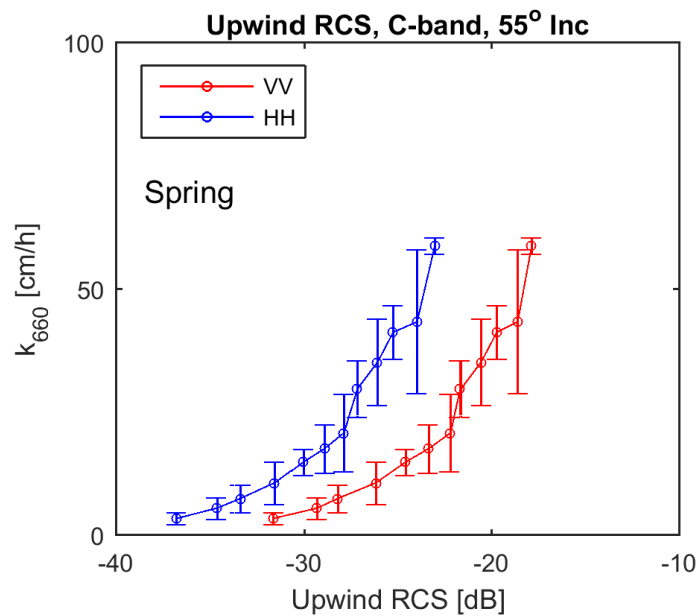


Figure 6.8: Same as Figure 6.7, but in spring.

Table 6.1: The empirically determined coefficients of the scatterometer retrieved gas transfer velocity from the experiments by the Multi³Scat at different radar frequencies and polarizations and their related statistics.

Setting		$\kappa = 10^A \cdot \sigma_{pp}^B$			
		A	B	RMSE [<i>cm/h</i>]	r^2
S-band	VV	4.096	1.3	10.02	0.82
	HH	4.267	1.0	10.21	0.82
	VH	5.333	1.1	9.73	0.83
C-band	VV	3.814	1.1	10.05	0.82
	HH	3.970	0.9	9.70	0.84
	VH	4.701	0.9	9.29	0.85
X-band	VV	3.953	1.1	10.24	0.82
	HH	4.065	0.9	9.51	0.84
	VH	5.411	1.2	9.38	0.85

Related to Table 6.1, is Figure 6.9 which presents the relation between gas transfer velocity and C-band radar backscatter at different polarizations over the measurements period (November 2011 to August 2012). The data are averaged over 1 *m/s* wind speed and the error bars correspond to the deviations from the mean value. The root mean square error (RMSE) of 9.29 *cm/h* is the smallest value from the cross polarization C-band radar backscatter with a correlation of 0.85. The HH polarization X-band radar backscatter with a RMSE of 9.51 *cm/h* and a correlation of 0.84 gives a good result in HH polarization. The advantages of VH polarization radar backscatter in quantifying the sea surface roughness properties without dependence on incidence angle and azimuth direction is discussed in Chapter 5. Also, the relative importance of the HH polarization in quantifying the impact of the wave breaking and steep waveforms (effect of tilting waves) are debated.

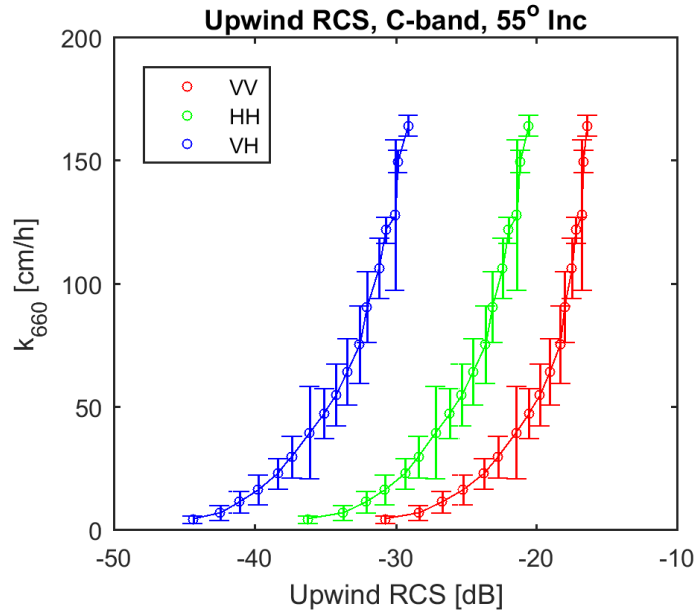


Figure 6.9: Upwind C-band RCS from Multi³Scat observations versus gas transfer velocity computed from the direct eddy covariance method, both in the Western Baltic Sea. The data are averaged over the period from November 2011 to August 2012, providing one data every 1 *m/s* wind speed. Red, green, and blue corresponds VV, HH, and VH polarization RCS, respectively.

From the statistics in Table 6.1, the estimated gas transfer velocity using the radar cross section yields smaller RMSE in HH polarizations in comparison to the VV polarizations. Referring to our discussion in Chapter 5, the cross polarizations are less sensitive to the signal saturation at higher wind speed than that of the co-polarizations, with less dependence on azimuth direction. Considering better correlation between RCS-based gas transfer velocities estimated from our cross polarization radar backscatter and observed gas transfer velocities, we fit our data to the following relation between gas transfer velocity and cross polarization C-band radar backscatter:

$$\kappa = 10^{4.70} \cdot \sigma_{vh}^{0.09} \quad (6.5)$$

To assess the performance of our RCS-based gas transfer parameterizations, Figure 6.10 presents the scatter diagram of the computed gas transfer velocity from our C-band parameterizations and observations. Moreover, we compare the RCS-based gas transfer velocity and wind-based gas transfer velocity of different models (see Table 2.1) with respect to wind speed. The RCS-based gas transfer velocity shows a good agreement with observations.

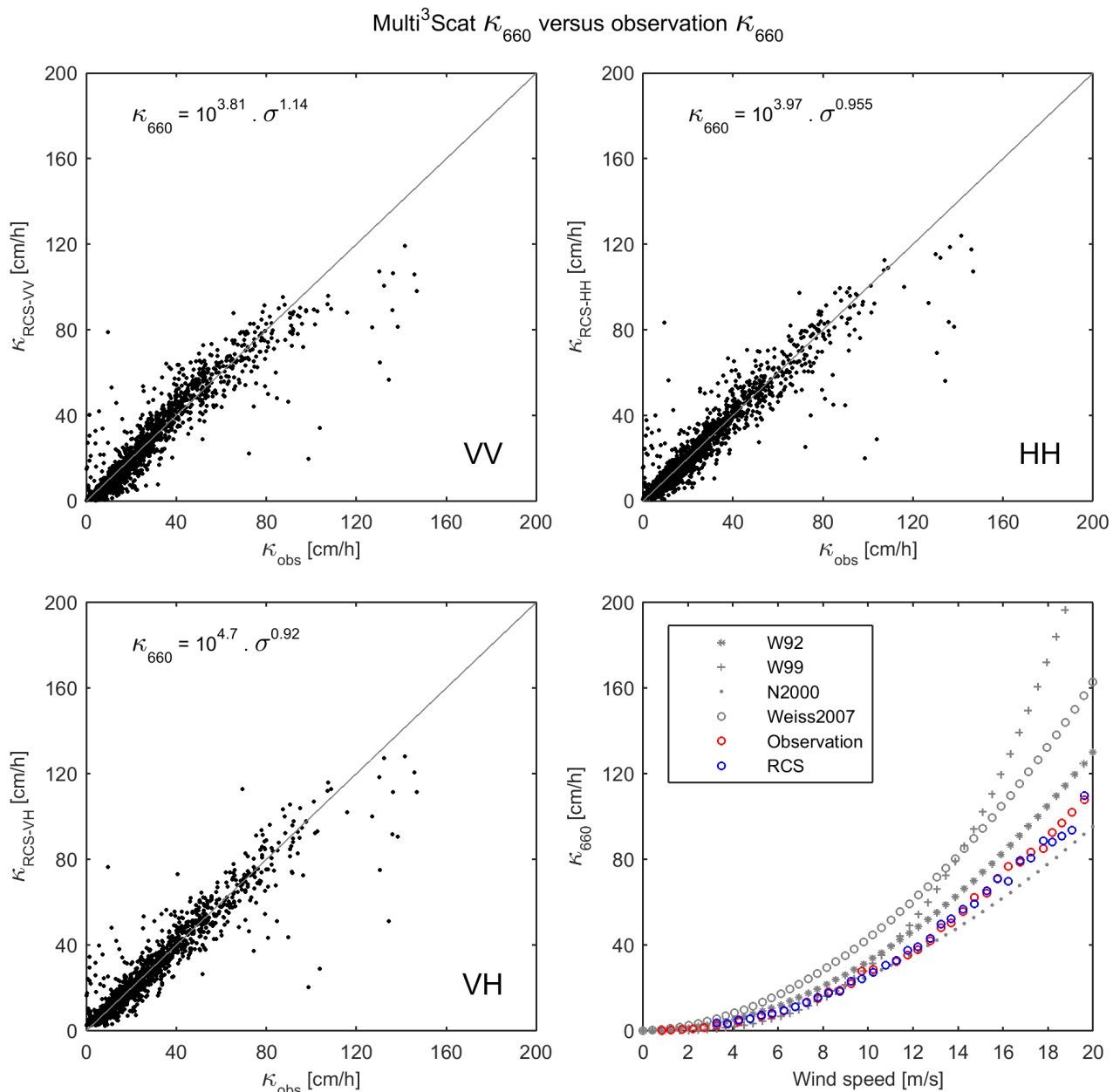


Figure 6.10: The RCS-derived gas transfer velocity versus observed gas transfer velocity. Different panels corresponds to the different radar polarizations; VV (upper left), HH (upper right), and VH (lower left). The lower right panel compares the radar-based, observational, and modeled gas transfer velocities with the averaged datasets of 0.5 m/s wind speed.

The surface/interface parameters (wind and waves) in the Western Baltic Sea are subject to seasonal changes, mainly driven by wind variation, and affecting the gas transfer velocity (see Section 6.1 and Section 4.3) [Schneider et al., 2014; Rutgeresson et al., 2009; Takahashi et al., 2009].

Therefore, we look at the seasonal variation of RCS-based gas transfer velocity from

the Multi³Scat observations (Equation 6.4 and 6.5), and compare them with transfer velocity from observations and models. The seasonality of the averaged amount of gas transfer velocity in the Western Baltic Sea is demonstrated in Figure 6.11 from November 2011 to August 2012. The figure shows in red the monthly averaged gas transfer velocity from observation (computed from observations and Equation 6.1) and in blue colors the monthly averaged computed gas transfer velocity from wind-based models of Nightingale et al. [2000] (shown as N2000; the closest to the observational value) and Weiss et al. [2007] (shown as W2007; the same study area). The gas transfer velocities using radar backscatter are shown in green colors.

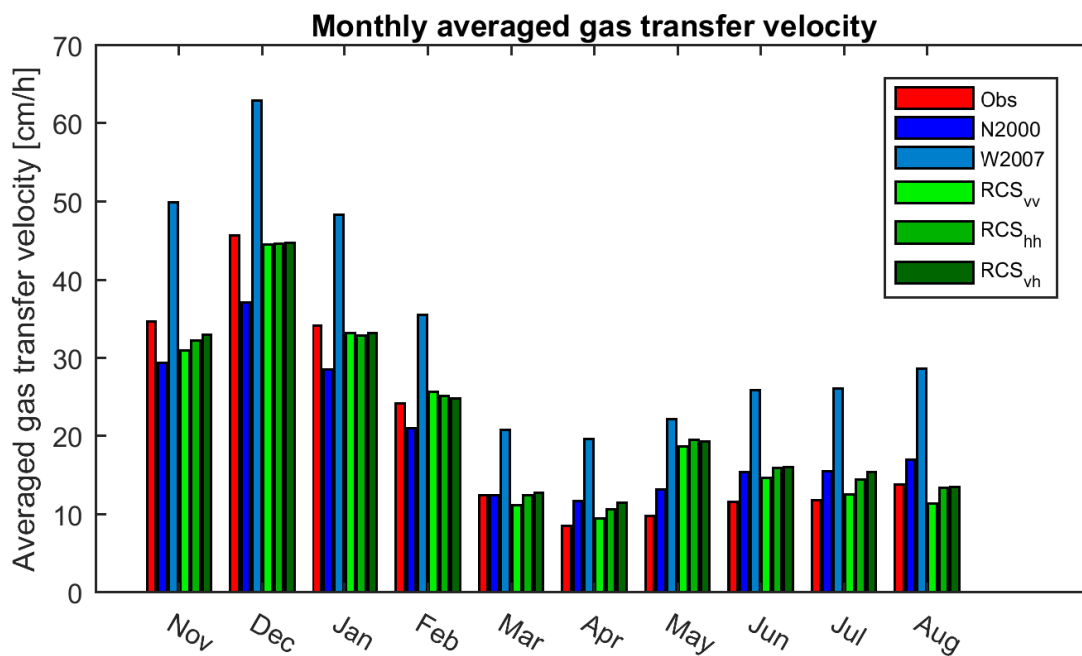


Figure 6.11: Seasonal variation of the averaged gas transfer velocity in the Western Baltic Sea. The panel shows in red observational gas transfer velocity, in blue and turquoise the wind-based gas transfer velocities of Nightingale et al. [2000] and Weiss et al. [2007], respectively, and in green colors the scatterometer-based gas transfer velocity.

From observations, the largest gas transfer velocity is found from November to January and the smallest in April. In April, even though the partial pressure difference of CO₂ is large, the influence of the stable atmospheric condition, low wind speed, and calm sea surface control the gas transfer velocity. The same variation is noticed from the RCS-based gas transfer velocity at all radar polarizations. Except in May, the RCS retrieved κ is larger than the observed values while for the rest of the months the RCS retrieved κ shows very

good agreement with observations. However, the wind-based model of [Nightingale et al. \[2000\]](#) produces smaller values than observations in all cold months and larger values than observations in all warm months, except March. The wind based model from [Weiss et al. \[2007\]](#) produces particularly large values at high wind speed. overall, the averaged value of gas transfer velocity using scatterometer data is about 26.95 cm/h and is close to the reported value for offshore seas.

We note that, in the cold season, during rough sea surface conditions and wave breaking HH-RCS and VH-RCS retrieved gas transfer velocity is better correlated with observations, and during stable atmospheric conditions and small scale wave breaking and surface roughness, VV-RCS correlates better with observations.

To see the influence of atmospheric stability on radar backscatter and gas transfer velocity, Figure 6.12 displays the relationship between RCS and κ at unstable (red circles) and stable (blue circles) atmospheric conditions. Explained in Chapter 5, the advantages of using VH polarization, which is weakly dependent on incidence angle and wind direction, allowed us to consider observations in all wind directions. It provides us more data points and better results. From Figure 6.12, the difference of about 1 dB is noted between observations in unstable and stable atmospheric conditions.

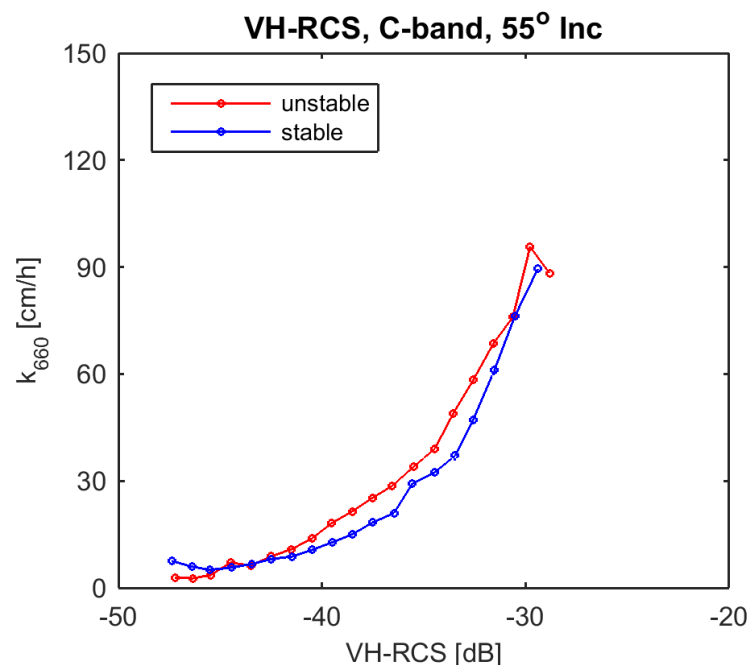


Figure 6.12: C-band VH-RCS and gas transfer velocity from observations in the Western Baltic Sea in presence of unstable (red) and stable (blue) atmospheric stability.

CO₂ flux retrieval from the scatterometer data

When calculating the air-sea CO₂ flux, the greatest uncertainties are from the transfer velocity [Yu et al., 2014; Rutgersson et al., 2009; Takahashi et al., 2009]. Here, we apply the gas transfer velocity retrieved from our Multi³Scat observations to the bulk flux formulation (Equation 1.1) and compute the CO₂ flux from the ΔP_{CO_2} observations.

The correlation between the two data sets, one directly from observations and the other calculated from the scatterometer observations of the sea surface is presented in Figure 6.13. The data are time-averaged from November 2011 to August 2012, providing one value every hour for CO₂ flux. Our new RCS-based parameterizations are obtained from upwind RCS, therefore the data points correspond to observations in the upwind direction. Our estimated flux shows a good correlation with observations, about 0.83, and a small offset about $0.027 \frac{\mu\text{mol}}{\text{m}^2\text{s}}$ for all observations. The averaged CO₂ flux of $0.23 \mu\text{molm}^{-2}\text{s}^{-1}$, estimated by using the new scatterometer based transfer velocity parameterization, results in a very close value to the observed value of $0.21 \mu\text{molm}^{-2}\text{s}^{-1}$.

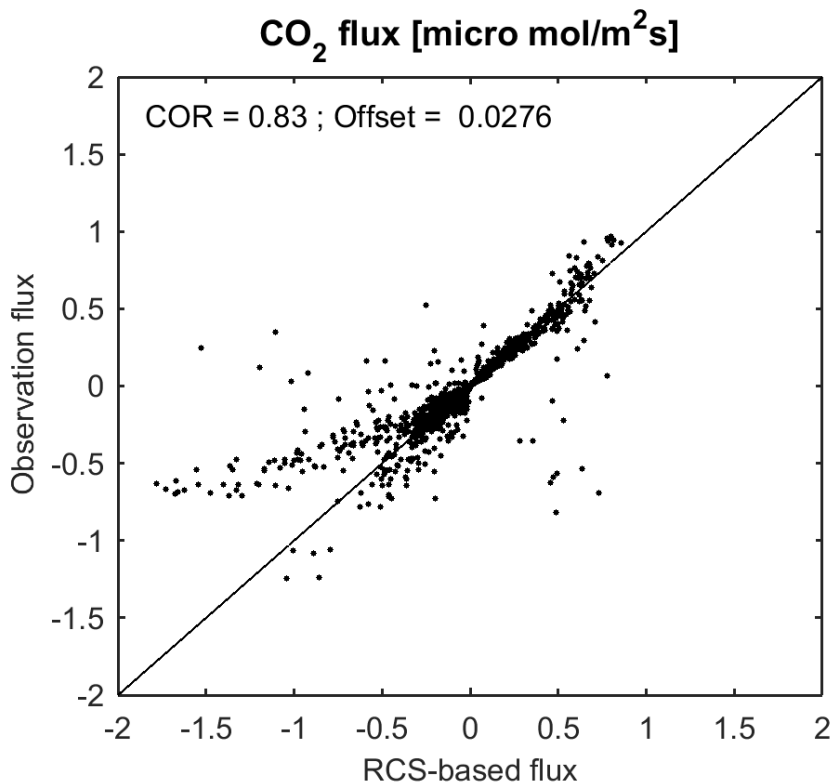


Figure 6.13: RCS-based CO₂ flux versus observations in the upwind direction. Statistics of the comparison are given in the panel.

For a more detailed analysis, we look at the seasonal variation of computed flux from Multi³Scat observations. Figure 6.14 displays in dark blue the CO₂ flux from the eddy covariance system (direct observation) and in yellow the computed flux from the Multi³Scat observations at C-band, VV polarization. The good agreement between the computed flux and observations during the cold season is noticed. However, during the warm season, the results are modified by the effect of large partial pressure differences of CO₂. In May, when the partial pressure difference has the largest value, the computed flux also shows the largest deviation from the RCS-based flux.

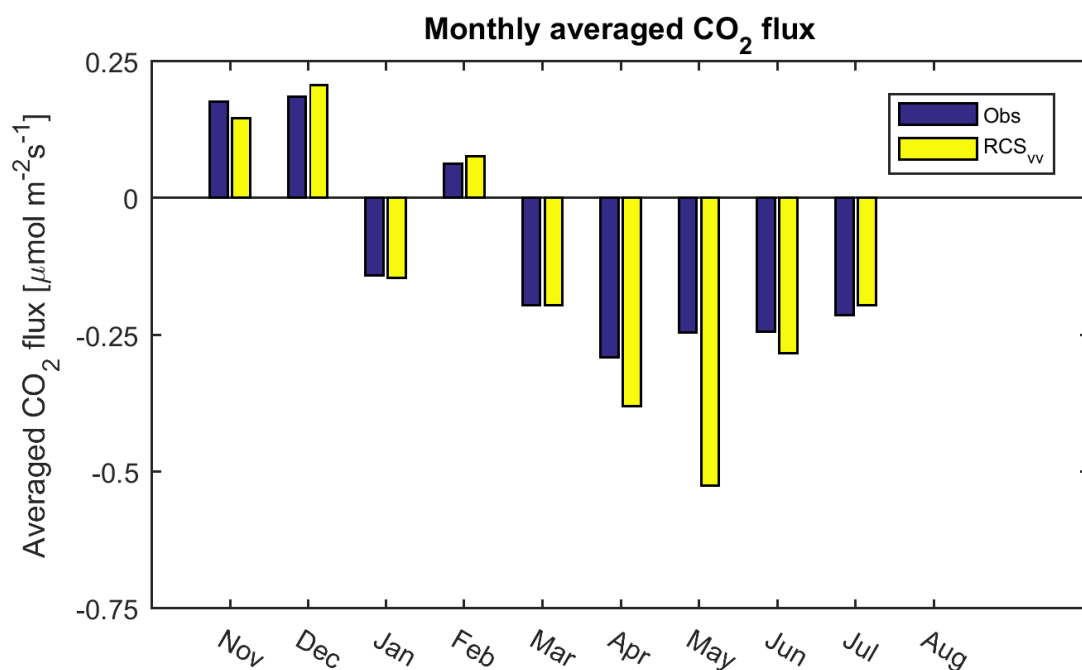


Figure 6.14: Seasonal variation of the averaged CO₂ flux in the Western Baltic Sea. The panel shows in dark blue the CO₂ flux from eddy covariance system (direct observation) and in yellow the RCS-based flux computed from Equation 1.1 using our RCS-based gas transfer velocity.

Flux estimation from modified radar backscatter using CMOD5 model

In Chapter 5, we discussed about the bias between the Multi³Scat C-band, VV polarization and CMOD5 model radar backscatter. We apply the averaged bias about 5 dB to our C-band RCS and we compare the computed flux from the modified radar backscatter with observations. The coefficients of the relation between the modified radar backscatter and gas

transfer velocity yield the relationship:

$$\kappa_{660} = 10^{3.45} \cdot \sigma_{vv}^{1.3} \quad (6.6)$$

The CO₂ flux obtained from the modified radar cross section using CMOD5 model results shows discrepancies from the radar cross section (Figure 6.15). The modified RCS-flux comparing to observations, underestimate the gas flux from October to March and overestimate it from March to July. Between October to March, the wind speed is high and atmospheric condition is mostly unstable, which enhance the near surface turbulence and produce more wave breakings. Comparing the results of this part with the results of radar backscatter from Multi³Scat, shows that Multi³Scat observations of the sea surface better estimate the gas transfer velocity observations. The bias between the Multi³Scat data and CMOD5 model varies temporally not only because of the wind vector but also as a consequence of the combination of the parameters modifying sea surface roughness.

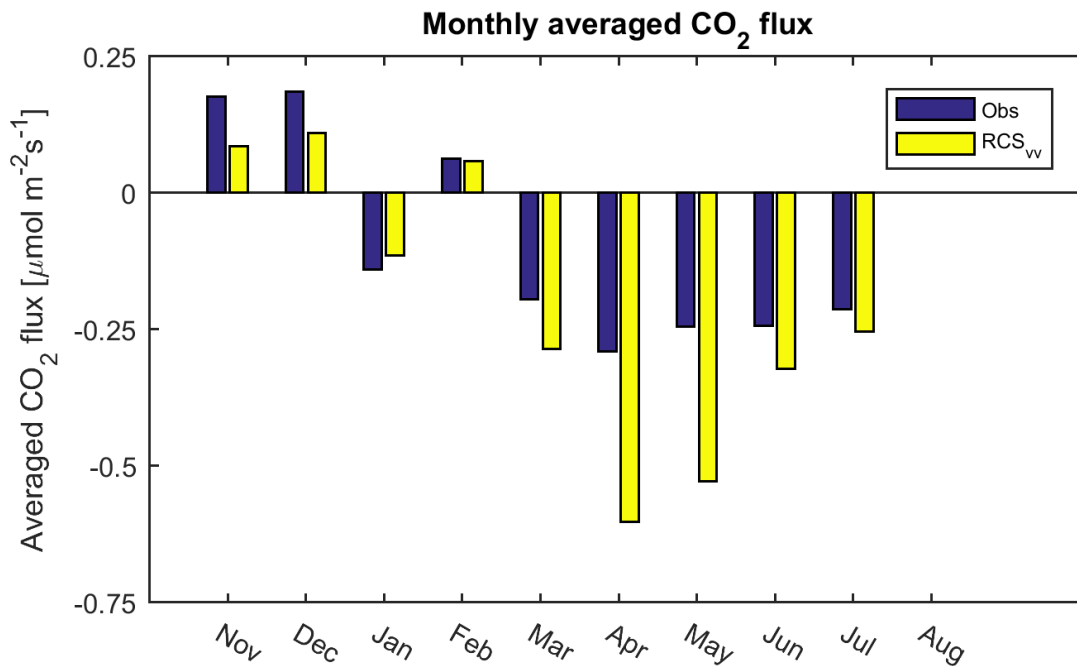


Figure 6.15: Same as Figure 6.14 but for modified radar cross section considering the bias between the Multi³Scat C-band, VV polarization and CMOD5 results.

6.3 Concluding remarks

This chapter aimed at improving the information on the air-sea CO₂ transfer velocity and flux collected in the Western Baltic Sea. From the eddy covariance method, CO₂ flux and mass density were collected from November 2011 to August 2012. The partial pressure of CO₂ in the air was calculated from CO₂ concentration, and in the sea water was measured from a ship passing the position at which the eddy covariance was performed (FINO-2 platform).

The data processing and filtering are applied to remove unwanted data caused by instrument failure. In addition to the first order density correction by [Webb et al. \[1980\]](#), we applied another correction method to remove CO₂ fluxes that are higher than the tenth order flux velocity of the sensible heat fluxes [[Weiss et al., 2007](#)].

From the observations in the Western Baltic Sea, gas transfer velocities range up to 120 *cm/h* at 20 *m/s* wind speed were obtained. The data were fit to the observed gas transfer velocities by using a quadratic dependence on wind speed. Long-term measurements allowed us to study the seasonal variation of gas transfer velocity. The seasonality analysis shows the same variation between winter and autumn and the same variation between spring and summer. The bias between observations and wind-based gas transfer velocity in cold seasons (winter and autumn) indicates the importance of short scale surface waves and near surface turbulence in addition to the wind on the gas transfer analysis. The scaling factor (wind speed power in the wind-transfer velocity parameterization) of the relationship between gas transfer velocity and wind speed is investigated seasonally for cold and warm seasons. This difference is the consequence of the seasonality of surface meteorological conditions such as wind, short waves, wave breaking, atmospheric stability, near surface turbulence, and many other factors which influence the sea surface roughness scale and therefore modify the rate of air-sea gas transfer.

Since the air-sea gas transfer velocity is significantly dependent on the sea surface roughness more than on wind speed alone [Barale and Gade \[2008\]](#), a method for including the influence of surface roughness of different scales on gas transfer velocity is proposed. This method is based on the assumption that the energy contained in the small-scale capillary waves is responsible for gas exchange [[Bock et al., 1999](#)]. Also, the radar backscatter from the sea surface observed by Multi³Scat is related to the energy dissipated by capillary waves [[Phillips, 1988](#); [Plant and Wright, 1977](#)]. These short scale surface waves are mainly driven by wind speed; however, they are influenced by the wind direction, nonlinear interaction between wave motion, longer underlying waves which carry them, surface films that suppress them, and breaking waves [[Garbe et al., 2014b](#)].

The correlation between the gas transfer velocity and radar cross section of the sea surface using Multi³Scat observations was investigated at different radar polarization settings. Quantitative assessments between the datasets by using the correlation of determination (R^2) and the root mean squared error (RMSE) is performed. The S-, C-, and X-band RCS show better RMSE and R^2 rather than L-band RCS. The correlation and RMSE between these three radar frequencies remained similar in value; however, the correlation between different polarization combinations vary. The cross polarization RCS-based gas transfer velocity shows a better correlation and a smaller RMSE against observations and models, and HH polarization RCS based gas transfer velocity also yields good correlation.

In order to provide better insight into the gas transfer velocity parameterization, seasonal variation of the averaged gas transfer velocity computed from Multi³Scat observations was analyzed and compared with observations and models. The slope of the relationship between κ and RCS, yields similar values for different reasons, indicating that the RCS is subject to seasonal changes to the same degree as the gas transfer velocity. The reason could be that the same surface parameters contribute to the variation of both RCS and gas transfer velocity. Therefore, radar cross section of the sea surface could be an appropriate parameter to estimate air-sea gas transfer velocity.

For a more in-depth analysis of the temporal variability of RCS-based gas transfer velocity, the monthly averaged computed gas transfer velocities were compared with monthly averaged observations for the entire measurements period from November 2011 to August 2012. A very good agreement between observations and RCS-based gas transfer velocities was found in all months, except in May, in which the radar backscatter overestimates the gas transfer velocity.

To conclude, the CO₂ flux was computed using RCS-based gas transfer velocity and CO₂ partial pressure difference, and compared with observations. The RCS-based flux shows a very good correlation with observations, 0.83, and a very small offset to observations, 0.027 $\mu\text{molm}^{-2}\text{s}^{-1}$. The averaged CO₂ flux of 0.23 $\mu\text{molm}^{-2}\text{s}^{-1}$, estimated by using the new scatterometer based transfer velocity parameterization, results in a very close value to the observed value of 0.21 $\mu\text{molm}^{-2}\text{s}^{-1}$.

CHAPTER 7

Conclusion and Recommendations

The increase of CO₂ concentration in the atmosphere by about 30% during the last century and the significance of the ocean as a major CO₂ sink are the main incentives of studying the air-sea CO₂ exchange in the ocean-atmosphere interface. In order to reduce the total error budget of the global carbon cycle model, quantitatively better air-sea gas flux estimates and more accurate air-sea gas exchange parameterizations are necessary. In this concern, the major problem comes from the uncertainty in air-sea gas transfer velocity estimation (by a factor of 2) caused by the limited understanding of the relationship between physical forcing and the gas transfer velocity [[Takahashi et al., 2009](#)].

The existing evidence shows that the gas transfer velocity is sensitive not only to wind speed but also to a variety of processes in the air-sea interface: atmospheric stratification, sea state and wave height, wave breaking, and surface films. Therefore, direct measurements of the sea surface roughness at centimeter scale, (the relevant scale for gas transfer velocity) from wind-driven waves is crucial.

In this section, we provide an overview of the main conclusions of this thesis as well as recommendations for further work.

7.1 Summary of the thesis and main conclusions

In this thesis, we studied the correlation between the air-sea CO₂ transfer velocity (κ) and short scale surface waves by using radar cross section (RCS) of the sea surface from a microwave scatterometer. The data used in this study are collected from a measurement campaign at the FINO-2 platform in the Western Baltic Sea from September 2011 to November 2013 [[Stammer, 2017](#)].

The scatterometer was mounted on the FINO-2 platform, at a height of 25 m above sea surface and measured the radar cross section for various radar observation settings (frequencies from 1 GHz to 10 GHz; polarization combinations VV, VH, HV, HH; incidence angles 35°, 45°, 55°), providing RCS at 5 minutes intervals. Each data point corresponds to the

averaged value over one-minute sampling per polarization and sampling frequency of 87.5 kHz.

The wind data and air temperature were collected from the sensors on the platform for the same observation period. The significant wave height (H_s) and sea surface temperature were measured by a buoy floating about 150 m away from the platform. The sea-water P_{CO_2} was obtained from measurements by a ship which passed the platform once a day. The CO_2 solubility was calculated using sea surface temperature and salinity.

The CO_2 flux was measured directly using eddy covariance methods for a period from November 2011 to August 2012. The Webb correction [Webb et al., 1980] was applied to remove the turbulent fluctuations of water vapor and temperature from the CO_2 flux data. Moreover, the CO_2 fluxes that were affected by a factor of 10 higher flux velocities of the sensible or latent heat flux were removed [Weiss et al., 2007]. With these observations, we computed the CO_2 transfer velocity.

On the ocean surface, surface waves are the roughness element. The small scale parts of the surface wave spectrum related to capillary-gravity waves modify the gas transfer rate. The length scales of the ocean surface roughness, in terms of the mean square slopes or with respect to the Bragg resonance wave components relevant to microwave remote sensing, are of sub-centimeter to meter wavelengths. The microwave radar backscatter from the sea surface is related to the energy dissipated by these capillary-gravity waves, making it feasible to estimate the gas transfer velocity using radar backscatter from the sea surface [Bock et al., 1999; Phillips, 1988; Plant and Wright, 1977].

To establish a mathematical relation between gas transfer velocity and radar backscatter from the sea surface, a two-step analysis is needed. First, it needs to relate the radar cross section of the sea surface to the mean square surface capillary-gravity wave slope. Second, it relates the mean square slope to the gas transfer velocity.

A quantitative analysis of the radar cross section dependence on surface/interface parameters is presented. The quality assessment was based on scattering theory and C-band geophysical model function (CMOD5). The radar backscatter is tested with respect to the radar observation settings (frequency, polarization, and incidence angle), and the strength and weakness of each radar observation parameters with regards to the ocean surface roughness properties are described. This analysis is related to the first goal of our thesis: to **Test the Multi³Scat observations from the sea surface in the western Baltic with respect to their usefulness for air-sea CO_2 exchange studies.**

The highest sensitivity of HH polarized RCS to the angular variation, in comparison to the VV and VH, is concluded from the different trend line slope in HH polarized RCS. The HH polarization RCS also shows more sensitivity to the incidence angle changes at low

wind speed rather than at high wind speed. The higher wave amplitude at high wind speed enhances the radar backscatter at shallow incidence angle. At low wind speed, the waves are shorter with lower amplitude compare to high wind conditions, which leads to a stronger reduction in backscatter intensity when the incidence angle increases. The average difference between high wind to low wind angular dependence in HH-RCS is about 7 dB and in VV-RCS is about 2 dB. The cross-polarization RCS show a downward trend with increasing incidence angle but with rather a small variability at S-band and C-band for a given sea state, which means that VH-RCS are essentially independent of incidence angle.

The radar backscatter from CMOD5 and Multi³Scat match with each other in terms of variation. The resulting differences between the values and the trend line slopes of the CMOD5-RCS and the Multi³Scat-RCS can be attributed to the combined impact of the calibration factor and the environmental forcings which has not yet been explored in the CMOD5 RCS.

The non-Bragg parts of the signal can be discussed individually using polarization ratio ($PR = \frac{VV}{HH}$). The non Bragg part of the signal is dominated by the contribution of wave breaking and steep waveforms (tilt effect) [Kudryavtsev et al., 2003; Romeiser et al., 1997]. From the PR angular dependence, S-band and C-band RCS are considered as the proper radar frequencies for quantifying the impact of wave breaking and steep waveforms. The results of this part are used to relate the gas transfer velocity to the radar backscatter at proper radar observation settings.

Observations with various radar observation parameters on long time scales, provide us a unique measurement spectrum, and enable us to compare the backscatter from the full measurements spectrum and make inferences about frequency and polarization dependencies. The combination of radar observation parameters (frequency, polarization, and incidence angle) with respect to the parameters influencing sea surface roughness such as wind speed, wind direction, atmospheric stratification, significant wave height, and wave steepness help us gain insight into sea surface roughness characteristics at the scale of interest for gas transfer estimation.

For a more in-depth analysis of the sensitivity of RCS to wind speed changes for different radar observation settings, the slope of the RCS-wind dependence is studied at different polarizations and frequencies. Steep incidence angle shows less sensitivity to wind speed changes. However, we noticed a different behavior of the X-band radar frequency in HH and VH-RCS but not in VV-RCS. The X-band RCS shows a fall off in HH-RCS and a stronger falls off in VH polarization. Higher microwave frequency is subject to changes by the impact of very short waves which, at high wind conditions and very rough surface conditions in the presence of large scale wave breaking, leads to a different behavior of the backscatter

intensity. The contribution of the wave breaking is larger in HH and VH than in VV which causes a fall off in the slope of the RCS-wind dependence only in HH and VH high-frequency band (X-band). This result is achieved by combining different radar observation settings and will be further considered in the gas transfer analysis.

The sensitivity analysis is done for azimuthal dependence as a consequence of the anisotropy of the energy density of short Bragg waves. Upwind to downwind asymmetry is the consequence of hydrodynamic modulation of short waves which are carried by the longer underlying waves [Kudryavtsev et al., 2003; Romeiser et al., 1997]. The upwind to crosswind asymmetry of radar backscatter is due to the angular distribution of the wave height spectrum [Kudryavtsev et al., 2003]. At high wind speed, the RCS dependence on azimuth is higher at higher incidence angles (55°). Comparing the different frequencies, a higher microwave band shows more strong upwind-crosswind asymmetry at all incidence angles and wind speeds.

The RCS anisotropy at low wind speed is weak at 35° incidence angle, for all microwave frequencies except L-band. At low wind speed, the observed upwind-crosswind asymmetry increases with incidence angle, however at high wind speed the directional dependence are statistically nearly equal for all incidence angles. This change is slightly larger in VV-RCS than in HH-RCS, hence the polarized part of the backscatter, which is controlled by Bragg resonance, dominates the upwind-crosswind asymmetry and is visible in VV polarization-shallow incidence angle radar backscatter [Mouche et al., 2006]. At high wind speed, wave breaking contribution to the total signal is more than Bragg resonance, and effects small changes in upwind-crosswind asymmetry with incidence angle changes.

The cross polarizations data are essentially independent of incidence angle and wind direction. This suggests the advantage of cross-polarization signals regarding the quantification of sea surface roughness, without the knowledge of wind direction and local incidence angle, and for sufficiently high wind speeds.

The sensitivity of radar backscatter to atmospheric stability is studied using air-sea temperature difference as a stability parameter. The impact of the air-sea temperature difference on radar backscatter is noticed during low wind speed. However, the higher microwave frequency and VV-RCS shows more sensitivity to air-sea temperature difference at all wind conditions. This finding is used to improve the gas transfer estimation using radar backscattering.

Here, we confirm that sea surface parameters that play important roles in gas transfer analysis modify our Multi³Scat observations leading to a quantitative study of the surface roughness scale by Multi³Scat radar backscatter.

To achieve the second goal of the thesis, **finding the correlation between observations**

of radar backscatter and CO₂ transfer velocity by using wind stress as a proxy, we calculated the gas transfer velocity directly from radar data by using the coefficient of the relation empirically obtained from Multi³Scat experiments in the Western Baltic Sea. Based on our results, we introduced the RCS-based gas transfer parameterization for different radar settings. The optimal parametric equations are determined with reference to observations using correlation (R^2) and root mean squared error (RMSE). We introduced the RCS-based gas transfer parameterizations for different radar polarization combinations with RMSE about 9-10 *cm/h* and correlation coefficients of about 0.83. The cross polarization presented better results with a smaller RMSE, better correlation coefficient and also the advantages of the cross polarization; weak directional dependencies, no sensitivity to incidence angles and tilting effect, and no signal saturation at high wind speed. However, for the general usage of gas transfer parameterization, co-polarizations are more popular, especially for satellite scatterometry. In order to achieve the third goal of the thesis, to **Develop a parameterization to better estimate CO₂ exchange across the air-sea interface, which can further be used for satellite data**, we presented HH-RCS based gas transfer velocity results from our measurements. This takes into account that HH polarized radar backscatter is more sensitive to wind speed changes and also to the impact of breaking waves on the surface roughness scale.

Our new RCS-based gas transfer velocity is assessed against observations and the traditional wind-based gas transfer parameterizations of Weiss et al. [2007]; Nightingale et al. [2000]; Wanninkhof and McGillis [1999]; Wanninkhof [1992]. A better root mean square error and correlation coefficient are computed for RCS based κ (at X- and C- band, and in VH and HH polarizations). A more in-depth analysis of the seasonal variability of the gas transfer velocity verified the quality of our RCS-based gas transfer parameterization with monthly averaged values closer to observations compared with the other wind-based models. The impact of the atmospheric stability which was proofed in the radar backscatter from the sea surface, and the sensitive radar observation settings to the atmospheric stability changes is used to distinguish the gas transfer velocity at unstable and stable conditions. In comparison to the traditional wind-based gas transfer parameterizations, the newly improved scatterometer-based gas transfer parameterization shows a good correlation to the observation ($R^2 = 0.84$, RMSE = 9.7 *cm/h*), better than that of wind-based gas transfer parameterizations. The averaged value of gas transfer velocity using scatterometer data is about 26.95 *cm/h* and is close to the reported value for offshore seas.

We computed the CO₂ flux from the RCS-based gas transfer velocity and in-situ P_{CO₂}. The seasonal variation of the RCS-based flux shows a very good agreement with observation in cold seasons; however, in warm seasons the effect of P_{CO₂} in the bulk formulation caused

flux estimates that are too large. However, a strong flux during the warm season as a consequence of biological productivity that under-saturates the amount of CO₂ in the sea-water is expected. Here, more studies are required.

Since the impact of the contribution of the different components on radar backscatter is verified and radar-based gas transfer estimation does not need to be normalized with temperature and salinity (Schmidt number), it is possible to estimate the gas transfer velocity without accurate knowledge of sea surface temperature and salinity. The comparisons of derived gas transfer velocity from radar backscatter at microwave frequencies with field measurements and various investigations were directed towards achieving the last goal of the thesis, to **Test the new algorithm against eddy correlation estimates and against traditional wind-based flux estimates**. The averaged CO₂ flux of $0.23 \mu\text{molm}^{-2}\text{s}^{-1}$, estimated by using the new scatterometer based transfer velocity parameterization, results in a very close value to the observed value of $0.21 \mu\text{molm}^{-2}\text{s}^{-1}$.

An extension of this study constitutes the investigation of wave breaking by considering the infrared skin temperature and white caps coverage to verify our findings through different radar polarizations. [Bergeron et al. \[2011\]](#) compared the analysis using RADRASAT-1 SCANSAR images with CMOD5 results and confirmed a very good agreement between data sets. As our study discussed the correlation between the Multi³Scat observations and CMOD5, therefore SAR-images and space-borne scatterometer data can develop our new gas transfer parameterization in order to extract global gas flux using satellite scatterometer data.

Appendices

APPENDIX A

Radar Cross Section dependence on radar parameters and wind vector

Here, we present the Figures discussed in the previous chapters. This Appendix is including the dependence of the radar cross section on incidence angle and wind vector. Also the comparison between the Multi³Scat observation and CMOD5-retrieved radar cross section is represented.

A.1 Angular dependence of RCS

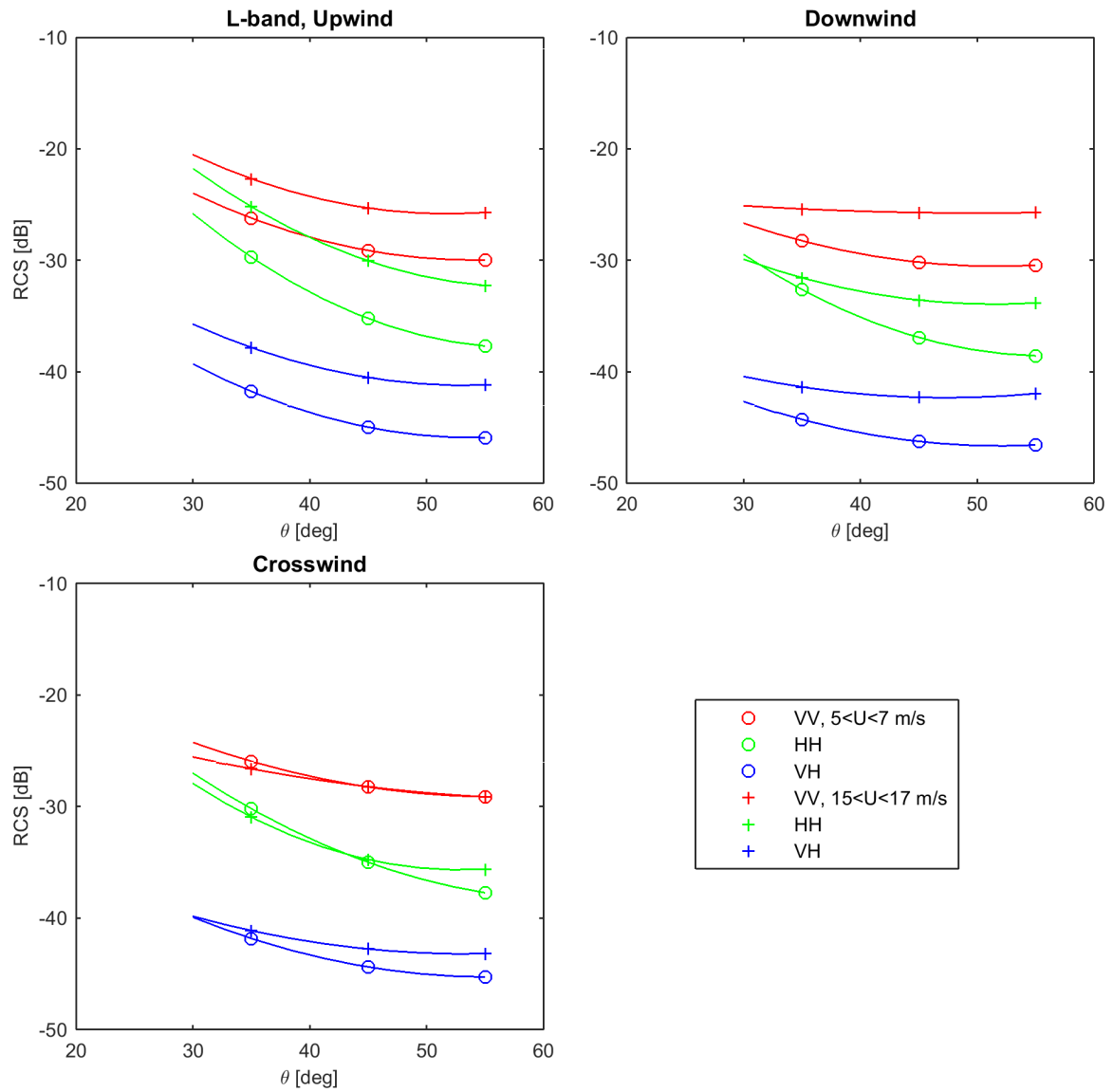


Figure A.1: L-band radar cross section measured by the Multi³Scat as a function of incidence angle, for wind speed ranges $5 - 7$ m/s (o) and $15 - 17$ m/s (+), at different polarization combinations, VV (red), HH (green), VH (blue), and different wind directions, Upwind (upper left), downwind (upper right), crosswind (lower left), (radar frequency: 1.0 GHz, wavelength: 30 cm).

110 Appendix A. Radar Cross Section dependence on radar parameters and wind vector

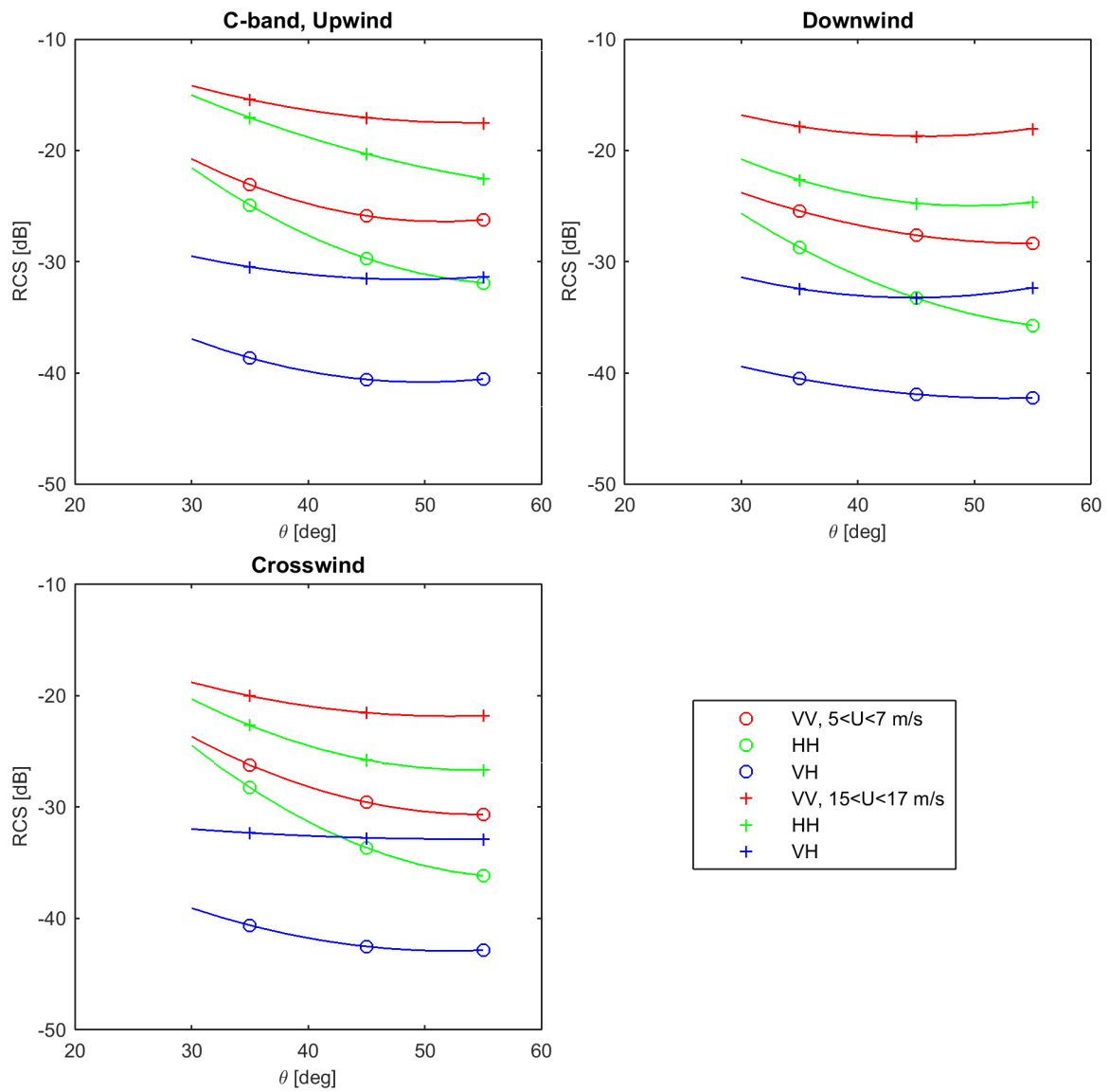


Figure A.2: Same as Figure A.1 but for C-band RCS (radar frequency: 5.3 GHz, wavelength: 3.0 cm).

A.2 RCS dependence on wind speed

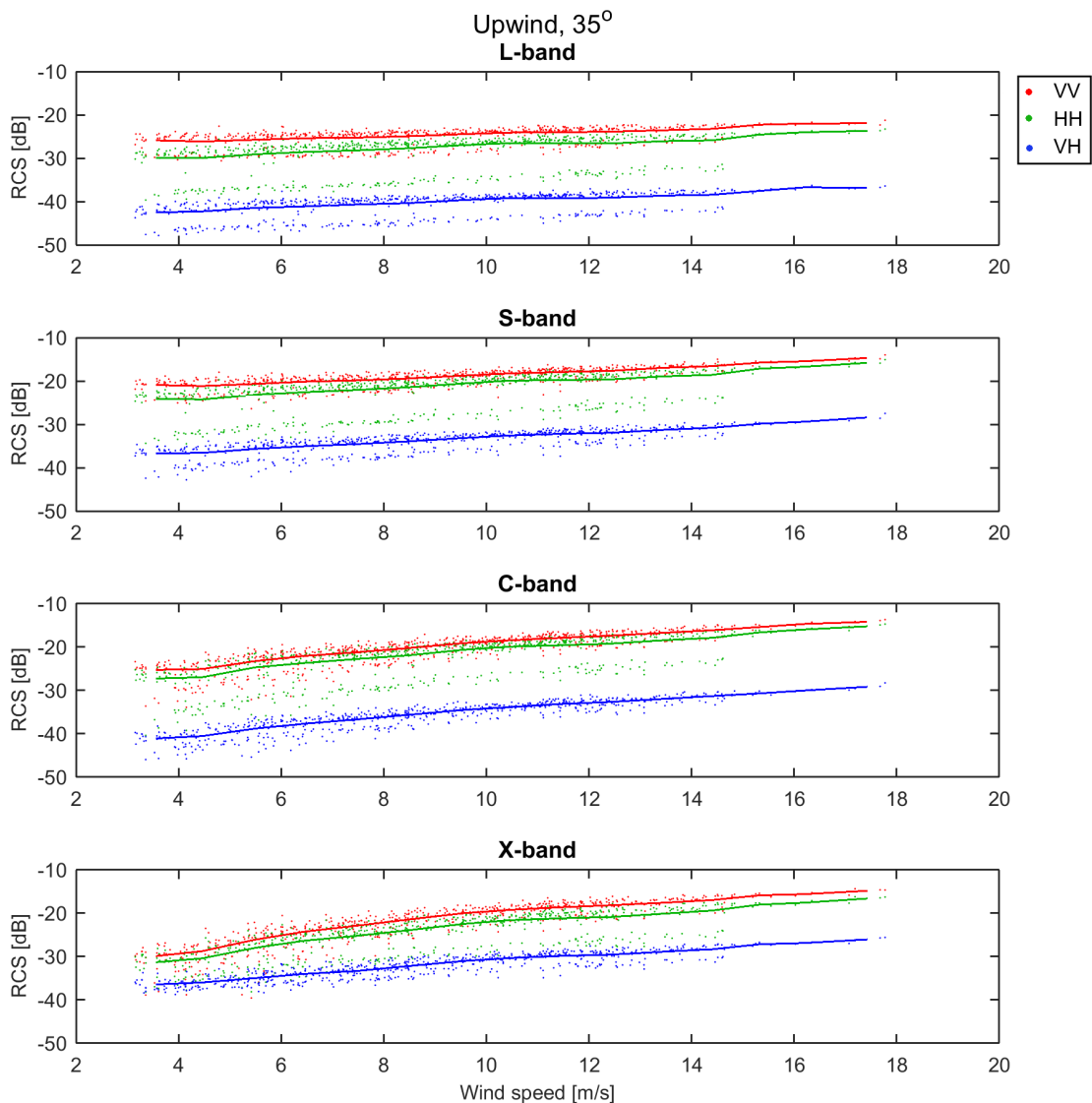


Figure A.3: Radar cross section in dB at 35° incidence angles as a function of wind speed in m/s , at four microwave frequencies (L-, S-, C-, X-band respectively from upper panel to lower panel), upwind direction and VV (red), HH (green), and VH (blue) polarization combinations. Each data point corresponds to averaged over 1 hour measurements and the lines show averaged value of radar cross section for windows of $0.5m/s$ wind speed.

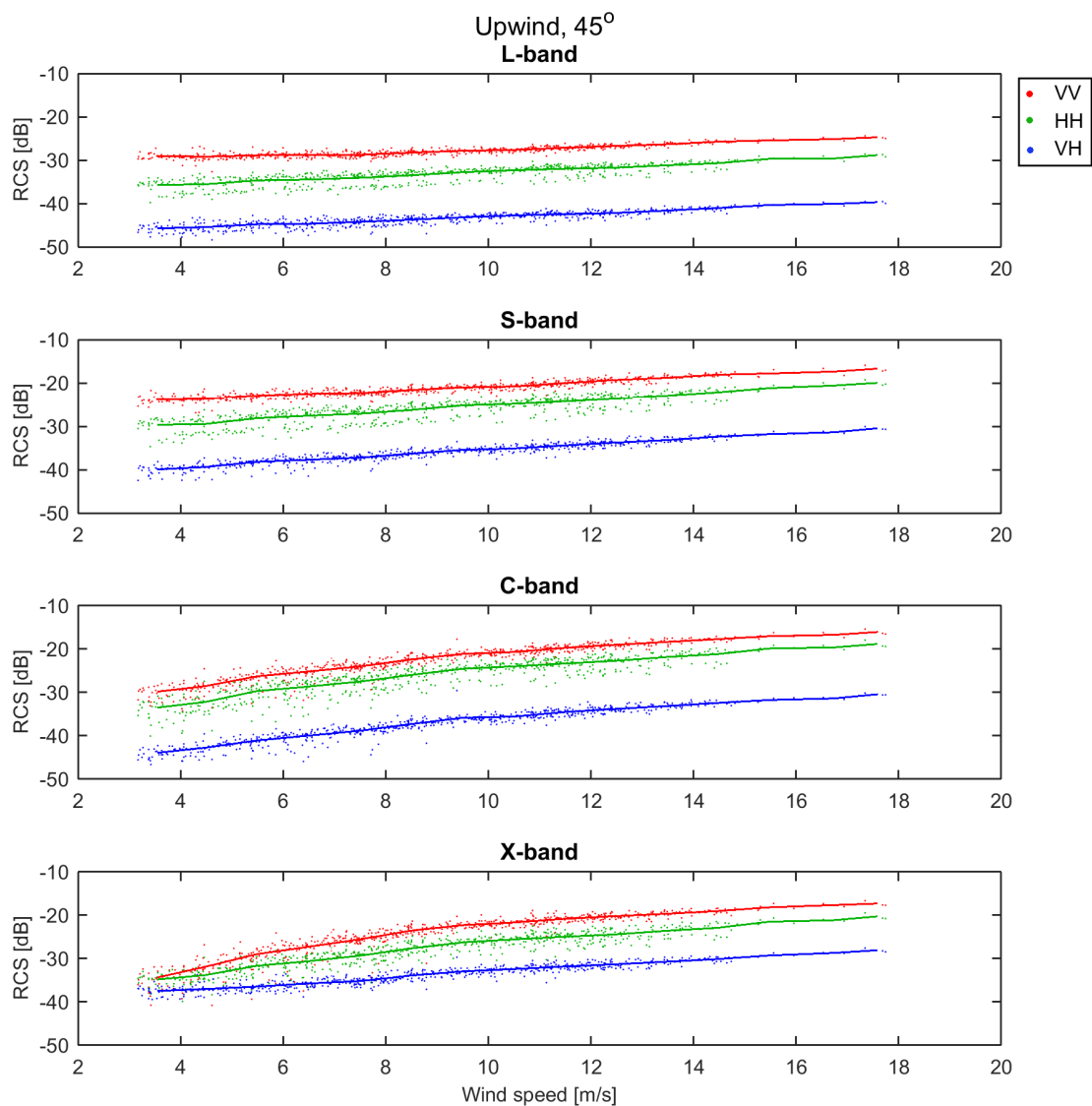


Figure A.4: Radar cross section in dB at 45° incidence angles as a function of wind speed in m/s , at four microwave frequencies (L-, S-, C-, X-band respectively from upper panel to lower panel), upwind direction and VV (red), HH (green), and VH (blue) polarization combinations. Each data point corresponds to averaged over 1 hour measurements and the lines show averaged value of radar cross section for windows of $0.5m/s$ wind speed.

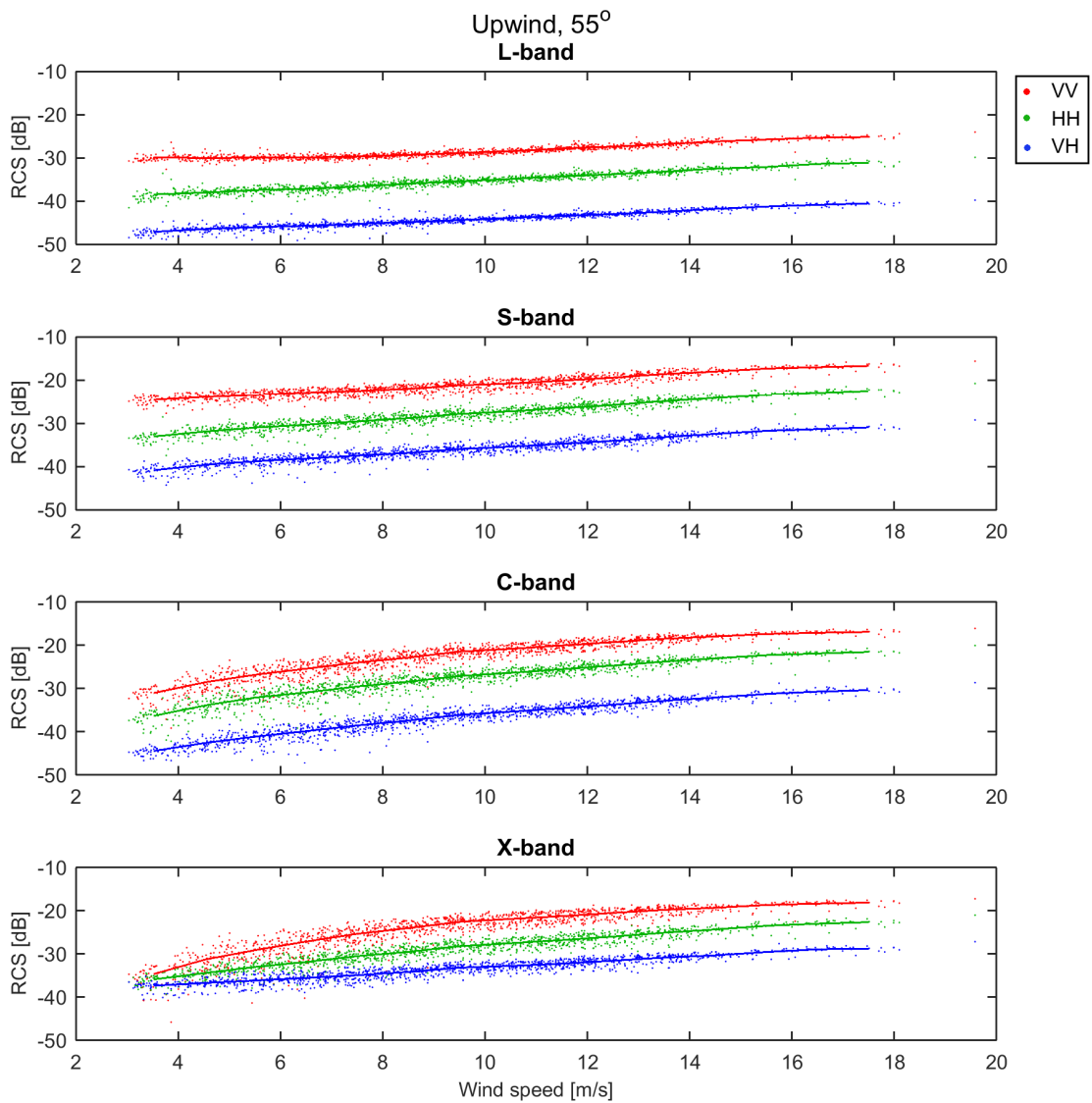


Figure A.5: Radar cross section in dB at 55° incidence angles as a function of wind speed in m/s , at four microwave frequencies (L-, S-, C-, X-band respectively from upper panel to lower panel), upwind direction and VV (red), HH (green), and VH (blue) polarization combinations. Each data point corresponds to averaged over 1 hour measurements and the lines show averaged value of radar cross section for windows of $0.5m/s$ wind speed.

A.3 Directional dependence of RCS

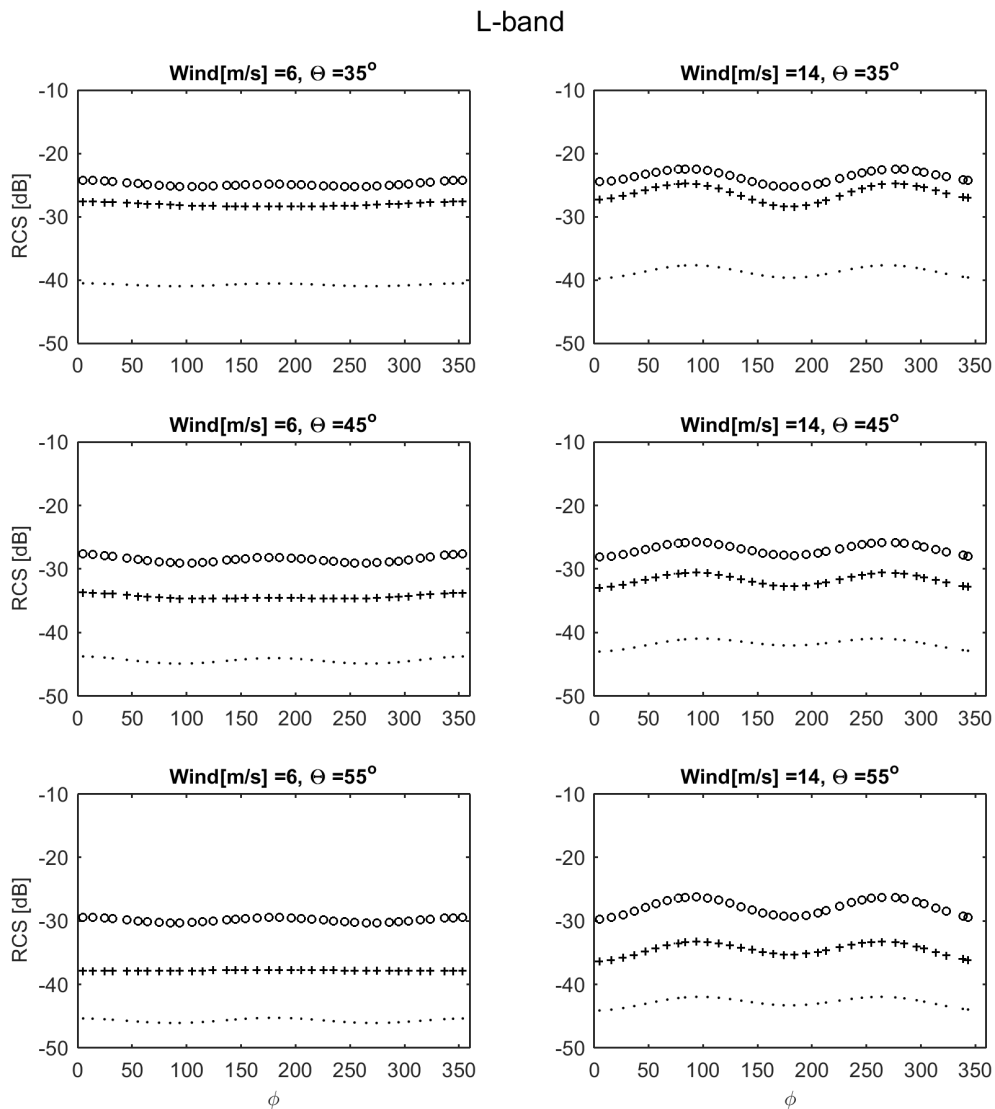


Figure A.6: Directional signature of L-band Radar Cross Section in VV (circle), HH (plus), and VH (dot) polarizations, for incidence angles of 35° (upper panels), 45° (middle panels), and 55° (lower panels) in two cases of wind speed 6 m/s (left column) and 14 m/s (right column).

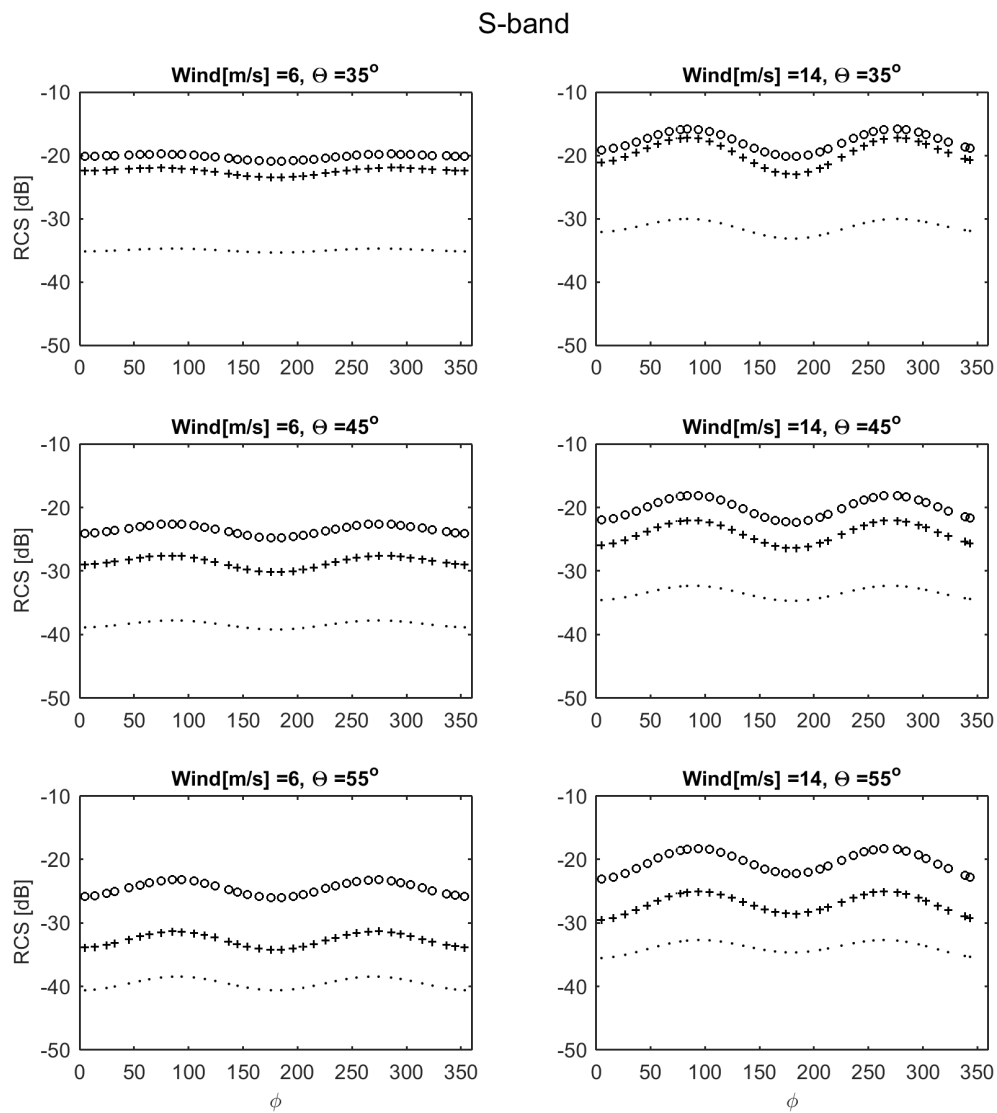


Figure A.7: Directional signature of S-band Radar Cross Section in VV (circle), HH (plus), and VH (dot) polarizations, for incidence angles of 35° (upper panels), 45° (middle panels), and 55° (lower panels) in two cases of wind speed 6 m/s (left column) and 14 m/s (right column).

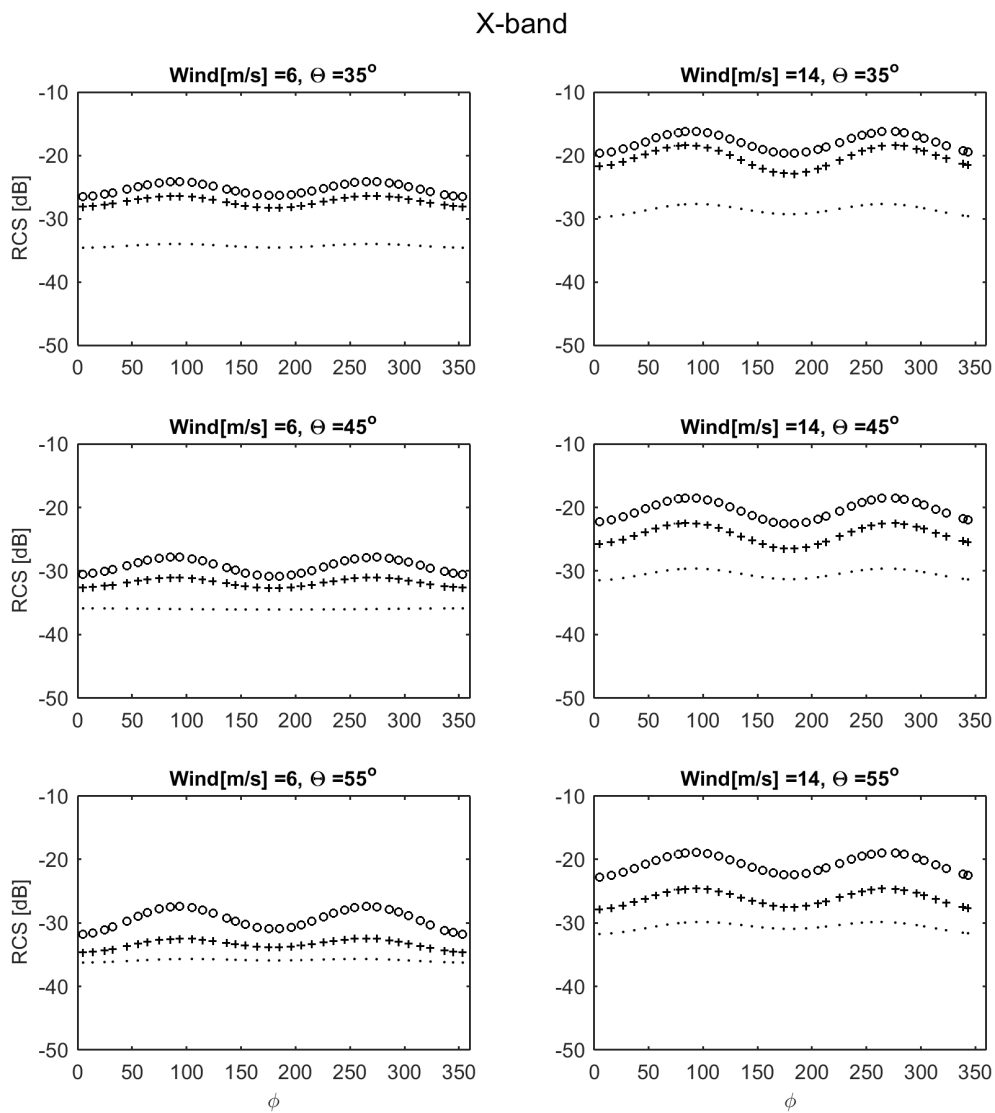


Figure A.8: Directional signature of X-band Radar Cross Section in VV (circle), HH (plus), and VH (dot) polarizations, for incidence angles of 35° (upper panels), 45° (middle panels), and 55° (lower panels) in two cases of wind speed 6 m/s (left column) and 14 m/s (right column).

A.4 Multi³Scat observation versus CMOD5 retrieved backscatter

In order to detect the difference between the Multi³Scat and CMOD5-retrieved RCS on seasonal timescale, the daily averaged RCS over one month at different seasons are displayed in Figure A.9. Each panel corresponds to one month of different seasons. The selection of the months is based on the different seasons and different atmospheric stratification (unstable-neutral-stable) during the measurement period. The atmospheric stability is determined using the air-sea temperature difference. The air-sea temperature difference is calculated from observations. The data are time-averaged over each month providing one single value for each day of the month. These values are used for the calculation of the statistics.

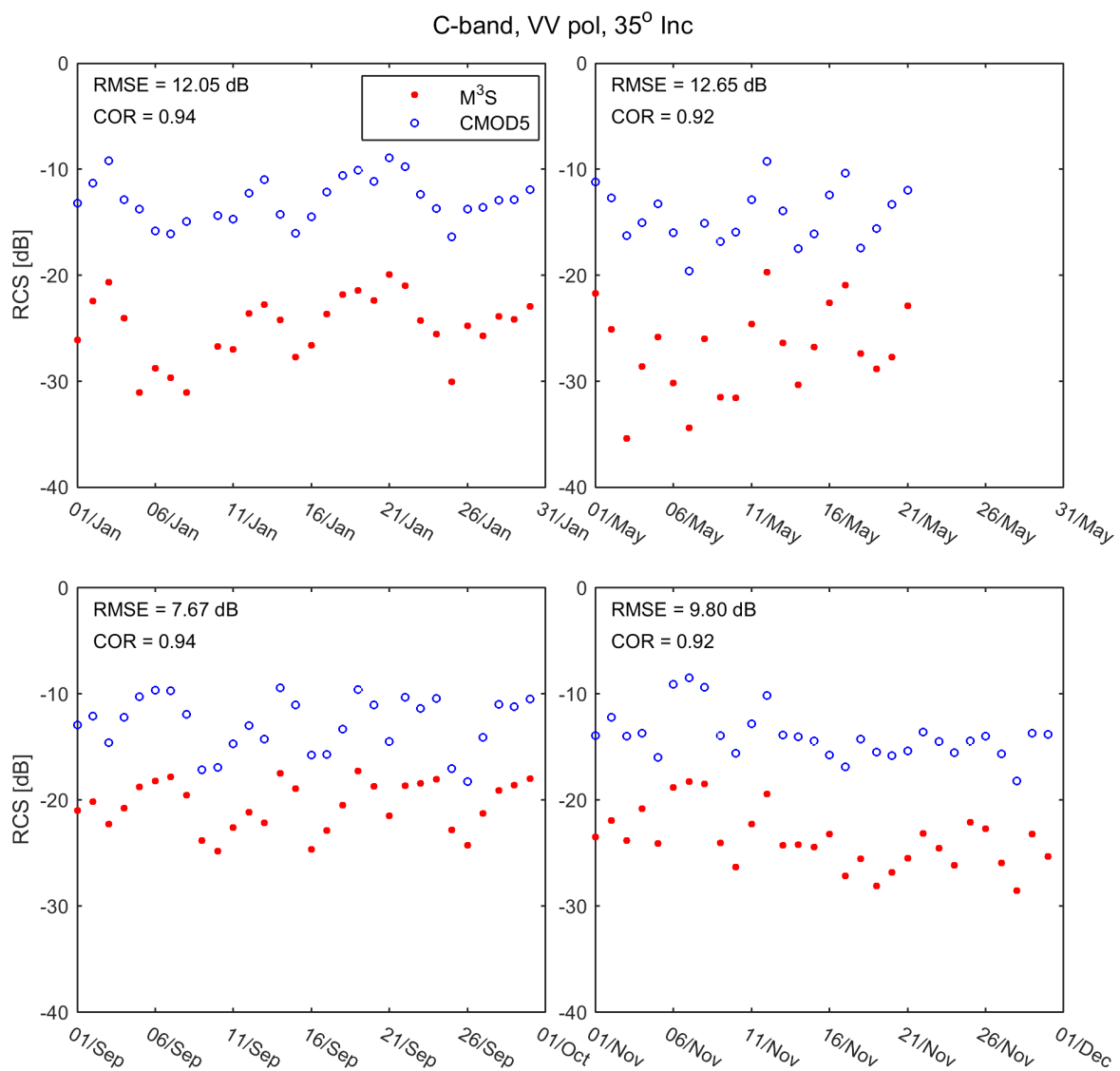


Figure A.9: Daily averaged radar cross section at C-band, VV polarization, 35° Incidence angle, the Multi³Scat observations (red circles) vs. CMOD5 model results (blue circles) data comparison under the same wind condition during one month measurements, upper left panel: January (mostly high wind speed), upper right: May (stable atmospheric stratification), lower left: October (neutral stratification), lower right: September (unstable stratification).

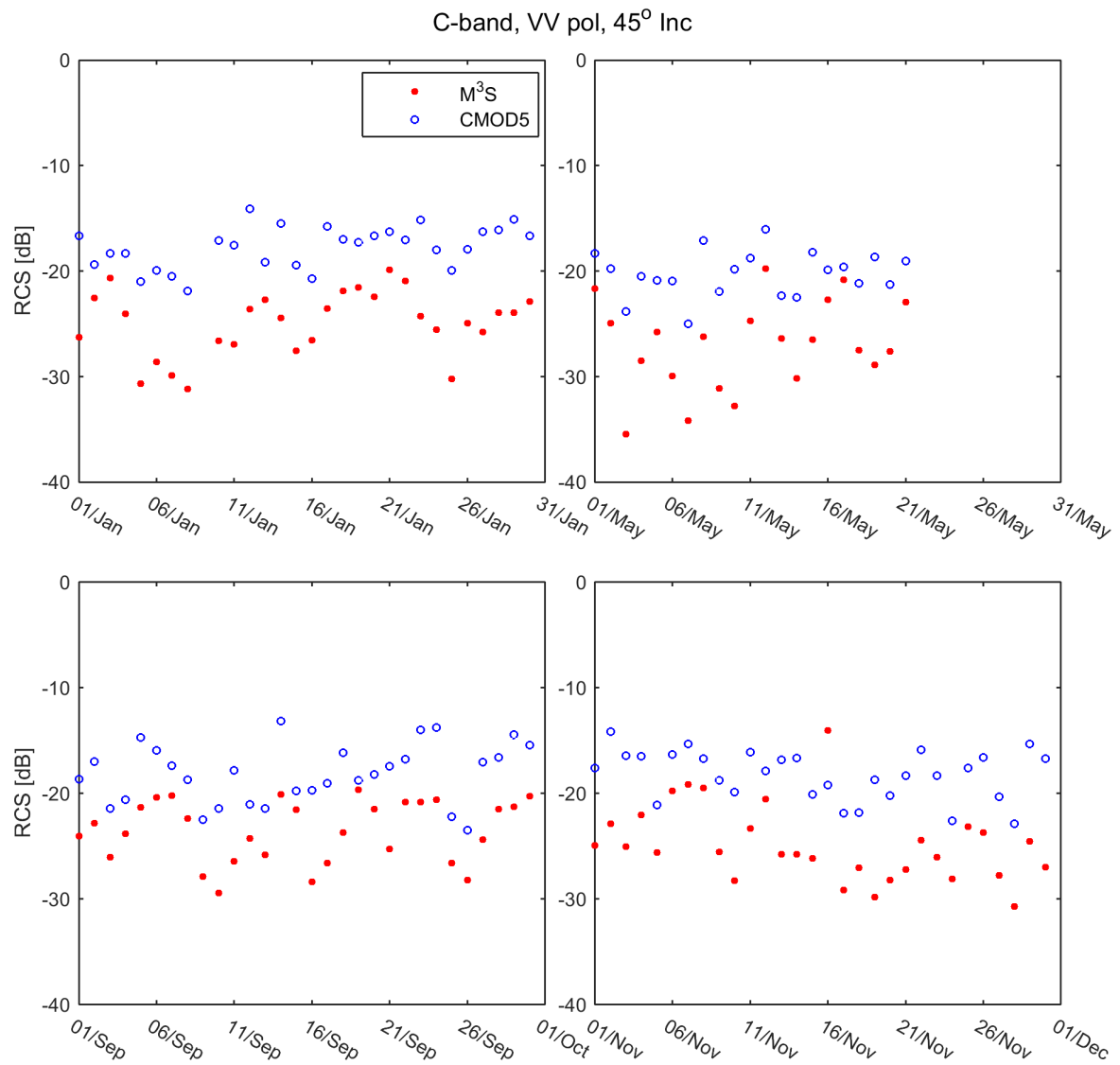


Figure A.10: Same as Figure A.9 but for 45° Incidence angle.

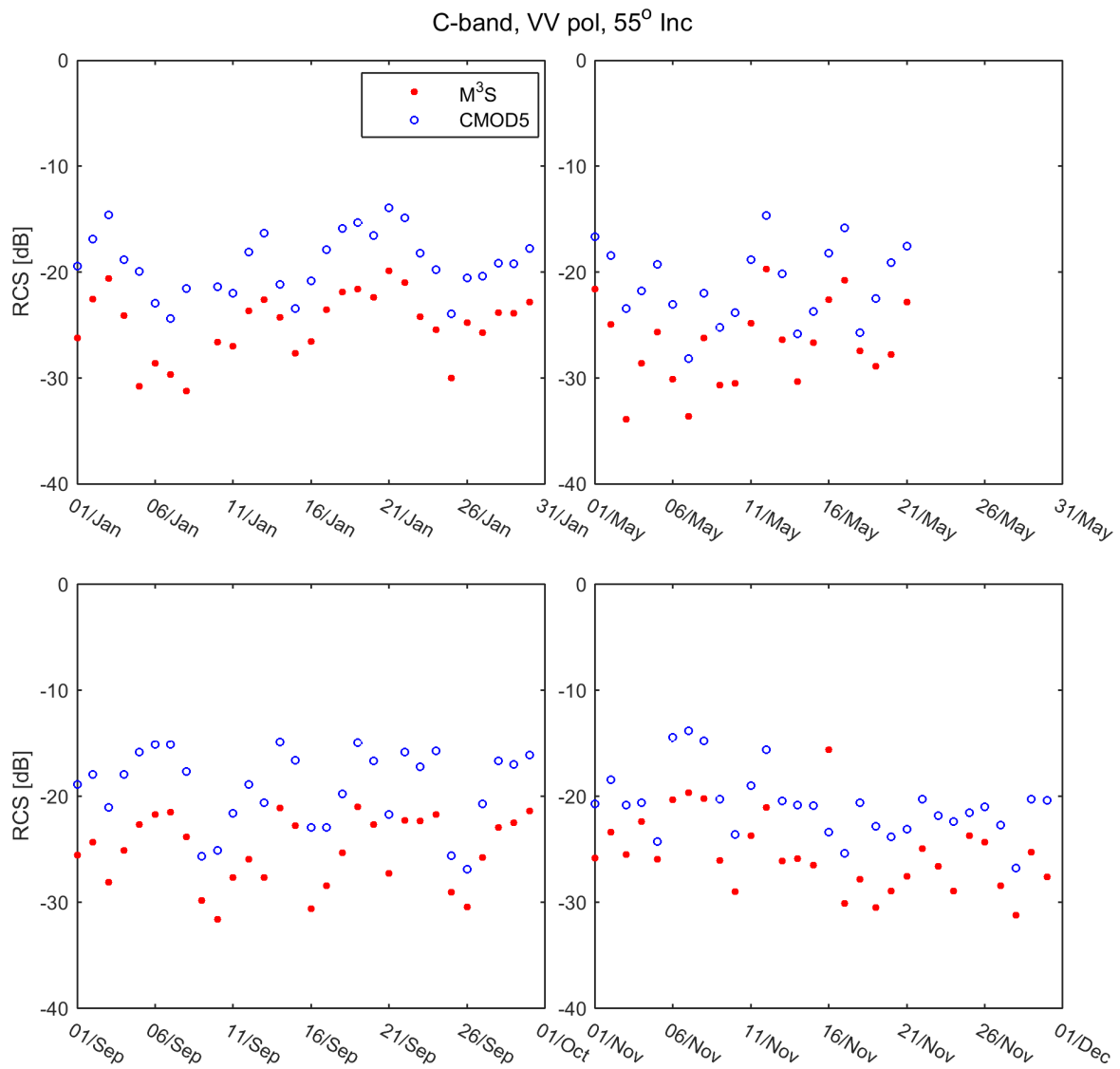


Figure A.11: Same as Figure A.9 but for 55° Incidence angle.

A.5 Polarization ratio at downwind direction

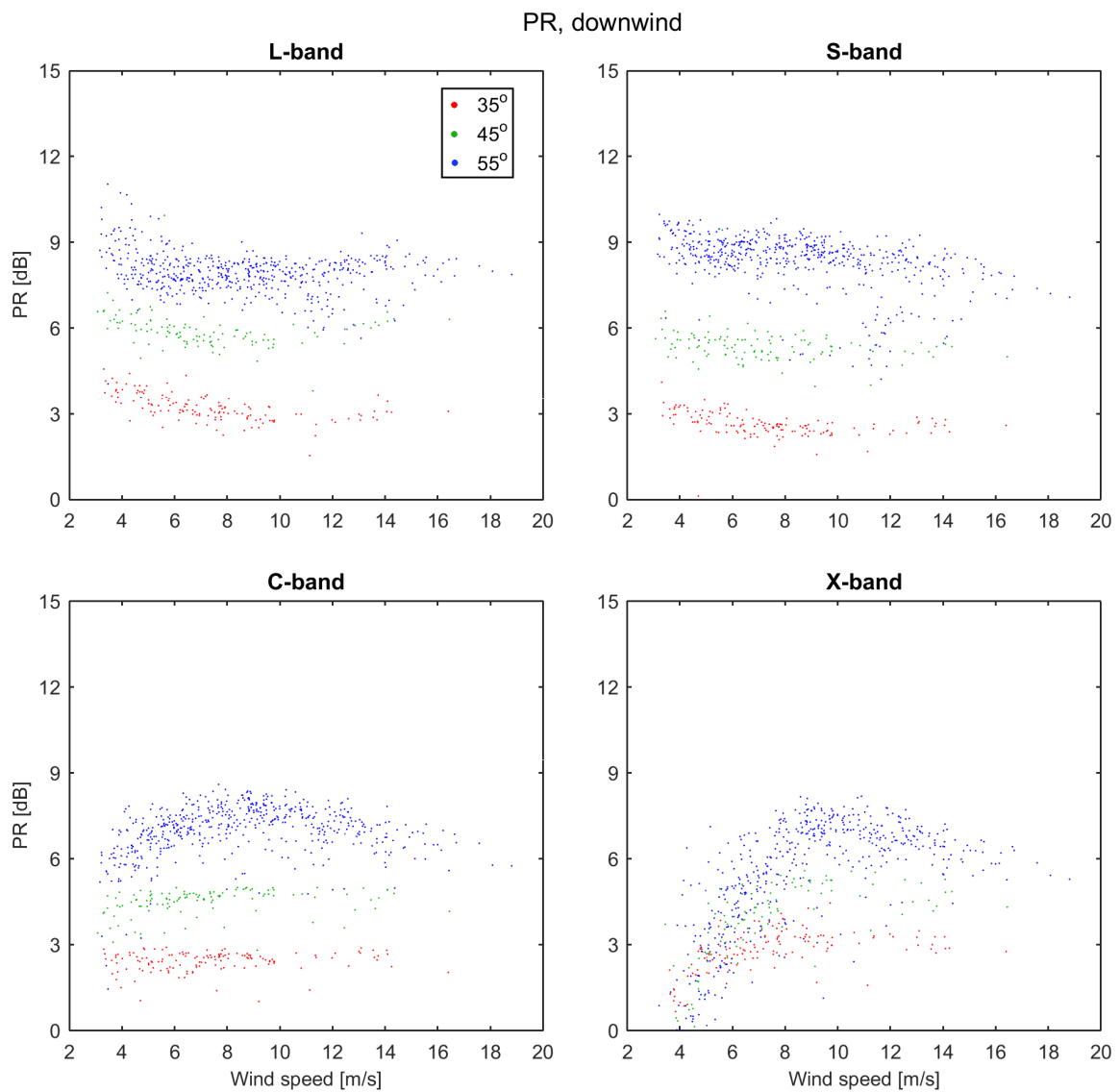


Figure A.12: Polarization ratio in dB as a function of wind speed in downwind direction, at four different frequency bands (L-, S-, C-, and X-band) and three incidence angles (35° (red), 45° (green), and 55° (blue)). Each data point corresponds to averaged over 1 hour measurements.

List of Figures

1.1	Climatological mean annual air-sea CO ₂ flux ($mol\ C\ m^{-2}\ year^{-1}$) for the reference year 2000, based on Takahashi et al. [2009] . The mean was computed by using the monthly averaged measurements of surface water P _{CO₂} , the NCEP-DOEAMIP-II Reanalysis 6-hours wind speed data, and the quadratic model of transfer velocity with a scaling factor of 0.26.	3
1.2	Simplified schematic of CO ₂ exchange across the air-sea interface (adapted from Hinrichs, 2014). The surface films and capillary waves that are riding on top of longer gravity waves are shown, as well as the wave breaking with the sharp crest and bubbles.	4
1.3	Wind based-gas transfer velocity parameterizations (shown in Table 2.1). They include the general relationships of Wanninkhof [1992] (star), Wanninkhof and McGillis [1999] (plus), Nightingale et al. [2000] (dot), and Weiss et al. [2007] (circle). The shaded area describes the deviation in the transfer velocity estimation from different formulations.	5
3.1	The scheme of a specular reflection from a calm sea surface (left) and microwave scattering from a rough surface (right). Here, the microwave scatterometer is fixed at a platform, transmitting and receiving the signals via one antenna.	18
3.2	Angular variation of radar backscatter for different sea states [Robinson, 2004]. The smooth surface at steep incidence angles follows the specular reflection so that radar backscatter is low. For the rough surface, a lot of energy is scattered in many directions but at shallower incidence angles; the reflected energy is more than that of the smooth surface at the same angle, which produces higher radar backscatter.	20
3.3	Angular dependence of radar backscatter at vertical (solid) and horizontal (dashed) polarizations. The gray vertical lines indicate the region of our measurements. Figure is adapted from [Barale and Gade, 2008].	22

3.4	The variation of σ_0 with the direction of the radar azimuth relative to the upwind direction at different wind scales. Figure describes radar cross section at 13.9 GHz and 40° incidence angle [Robinson, 2004].	25
3.5	The NRCS from CMOD5 model (C-band, VV polarization) as a function of incidence angle. The curves shows NRCS at different wind scales; high wind (plus) and low wind (circle), and for different wind directions; upwind (solid lines) and downwind (dashed lines). The calculated NRCS are based on the input data measured for the purpose of this study, including wind speed, wind direction, azimuth direction, and incidence angle.	27
4.1	The bathymetry map of the Western Baltic Sea, located in Northern Europe (from 11°E to 16°E and from 53.5°N to 57°N) and connected to the North Sea. The data source: Baltic Sea topography 1 minute of latitude and 2 minutes of longitude (iowtopo2).	30
4.2	The overview of the scatterometer components (Microwave part and PC system). Adapted from the Multi ³ Scat technical documentation.	32
4.3	The side view of the Multi ³ Scat antenna on FINO-2 platform, (Pictured by Mayk Fischer). The antenna diameter is 96 centimeters.	32
4.4	Variation of the radar backscatter measured by the Multi ³ Scat at different radar setting during the time of the measurements. Upper panel shows the backscatter with the focus on presenting the different microwave frequencies, the middle panel shows a comparison between polarization combinations, and the lower panel shows the aspect of various incidence angles. Each point indicates bin averaged of 1 day.	34
4.5	Photograph of the research platform FINO-2, which hosts the scatterometer (Multi ³ Scat) at a height of 25 m above the sea surface. FINO-2 is located 35 km north of the island Rügen in the Western Baltic Sea, border triangle of Germany, Denmark, and Sweden, (Pictured by Mayk Fischer).	36
4.6	Time table of the auxiliary data measured in/near the FINO-2 platform and used in this study. The light gray boxes correspond the months with not completed observations due to the instrumental failure, and the white boxes are the months with no observation. The green colored boxes indicate months with all data sets available, and the red colored boxes are the the months with less data sets.	37

- 4.7 Wind speed distribution and wind direction for 2012 (upper panel) and 2013 (lower panel). The maximum number of wind speeds are in the range of moderate wind 5 m/s to 10 m/s and the dominant wind direction is westerly. The y-axis shows the percentage of the number of data with respect to the total number at each interval. The number of the data points are normalized with the sum of the values. The vertical lines indicate the mean value (red) and the standard deviation (black). The red line fit the distribution using Weibull distribution coefficients. 38
- 4.8 Significant wave height distribution from buoy, 150 meters away from the platform (55° N, 13° E), for 2012 (left panel) and 2013 (right panel). The y-axis shows the percentage of the number of data at 30 minutes interval. The vertical lines indicate the mean value (red) and the standard deviation (green). The red line fit the distribution using Kernel distribution. 39
- 4.9 Time series of the data measured at FINO-2 platform. Radar backscatter at 5.3 GHz, VV pol, 55° Incidence angle (top). The black dots corresponds the backscattering in wind speed above 3 m/s and the red dots are the backscattering in wind speed below 3 m/s. Wind speed and wind direction over the measurements period (second and third, respectively). Water temperature measured by buoy placed about 150 m away from the platform (blue dots) and air temperature extrapolated to the temperature at 10 m height (red dots) (forth). Significant wave height measured by buoy (bottom). 40
- 4.10 The platform with the boom and the eddy correlation setup including the gas analyzer and sonic anemometer at both heights, 6.8 m and 13.8 m (left). The picture source: Sonstiges Schiff, IMO:16563, by Toron; www.vesseltracker.com. The close view of the complete setup at both height (right), and more detail of the distance between the gas analyzer and the anemometer (small picture). The picture from [Lammert and Ament \[2015\]](#). 41
- 4.11 Seasonal cycle of daily averaged CO₂ flux, atmospheric CO₂ mass density and partial pressure in the air and water surface. Observations at the FINO-2 platform from November 2011 till August 2012. The flux and mass density of CO₂ are directly measured at the platform by eddy covariance method. The water P_{CO₂} is measured on a cargo ship close to the platform. 43

- 5.1 S-band radar cross section measured by the Multi³Scat as a function of incidence angle, for wind speed ranges 5 – 7m/s (o) and 15 – 17m/s (+), at different polarization combinations, VV (red), HH (green), VH (blue), and different wind directions, Upwind (upper left), downwind (upper right), crosswind (lower left), (radar frequency: 2.4 GHz, wavelength: 12.5 cm). 47
- 5.2 Same as Figure 5.1 but for X-band RCS (radar frequency: 1.0 GHz, wavelength: 30 cm). 48
- 5.3 C-band, VV polarization radar cross section measured by the Multi³Scat as a function of incidence angle in comparison with CMOD5-NRCS at the same radar observation parameters, for wind speed ranges 5 – 7m/s (o) and 15 – 17m/s (+) and different wind directions, Upwind (upper left), downwind (upper right), crosswind (lower left), (radar frequency: 5.3 GHz, wavelength: 3.0 cm). 51
- 5.4 Multi³Scat RCS versus CMOD5 RCS in upwind direction, 35° incidence angle (left), and 55° incidence angle (right) over one year of measurements. Each data point corresponds to the averaged over 1 day of measurements. 52
- 5.5 Averaged polarization ratio of radar cross section as a function of incidence angle, at four microwave frequencies (different panels show different frequency band), the Multi³Scat observations at two different wind speed ranges, 5 m/s to 7 m/s (o) and 15 m/s to 17 m/s (+), upwind direction (red) and downwind direction (light red). Comparison with CMOD5 model results (black curves), [Thompson et al. \[1998\]](#) (gray), [Vachon and Wolfe \[2011\]](#) (blue) at C-band, [Shao et al. \[2016\]](#) (gray) at X-band, under the same wind condition. 54
- 5.6 Radar cross section in dB in VV polarization as a function of wind speed in m/s, at four microwave frequencies (L-, S-, C-, X-band respectively from upper panel to lower panel), upwind direction and three incidence angles (35° (red), 45° (green), and 55° (blue)). Each data point corresponds to an average over 1-hour measurement period and the lines show wind-averaged radar cross section for the windows of 0.5m/s wind speed. 57
- 5.7 The slope of the RCS-wind dependence shown in the Figure 5.6 as a function of microwave frequency band. Each panel displays the slopes at different incidence angles (35° (red), 45° (green), and 55° (blue)) for specific polarization; VV polarization (left), HH polarization (middle), and VH polarization (right). 58
- 5.8 Same as Figure 5.6, but in HH polarization radar backscatter. 60
- 5.9 Same as Figure 5.6, but in VH polarization radar backscatter. 61

- 5.10 Polarization ratio in dB as a function of wind speed in upwind direction from the Multi³Scat observations (circles), at four different frequency bands (L-, S-, C-, and X-band; corresponds to each panel) and three incidence angles (35° (red), 45° (green), and 55° (blue)). CMOD5-PR (calculated in combination with the PR model of [Hwang et al. \[2010\]](#)) at three incidence angles are shown in filled balls. Each data point corresponds to wind-averaged over 1 year of observation, providing values for every 1 *m/s* wind scale. 62
- 5.11 C-band radar cross section in VV (circle), HH (plus), and VH (dot) polarizations, as a function of the wind direction, for the incidence angle of 45° in different case of wind speed from 4 *m/s* to 14 *m/s* (± 1 *m/s*). Each data point corresponds to the averaged value over 10 deg wind direction for the duration of 1-year observations. The CMOD5 model results are plotted as blue filled circles and CMOD5+Hwang PR model in HH polarization is plotted as red dots. The vertical bar indicates the upwind direction. 65
- 5.12 Directional signature of C-band radar cross section in VV (circle), HH (plus), and VH (dot) polarizations, for incidence angles of 35° (upper panels), 45° (middle panels), and 55° (lower panels) in two cases of wind speed 6 *m/s* (left column) and 14 *m/s* (right column). 67
- 5.13 Directional dependence of C-band polarization ratio, for incidence angles of 35° (circle), 45° (plus), and 55° (dot) in two cases of wind speed a) 6 *m/s* and b) 13 *m/s*. The vertical bar indicate the upwind direction. 68
- 5.14 Directional dependence of a) L-band, b) S-band, and c) X-band polarization ratio, for incidence angles of 35° (circle), 45° (plus), and 55° (dot) in two cases of wind speed 6 *m/s* (left panel) and 13 *m/s* (right panel). The vertical bar indicate the upwind direction. 69
- 5.15 The impact of the atmospheric stratification on C-band radar backscatter in VV polarization, upwind direction, and wind speed ranges of 5 *m/s* to 7 *m/s* in blue, 7 *m/s* to 9 *m/s* in green, and 9 *m/s* to 11 *m/s* in red. Different panel presents different microwave frequencies. Negative air-sea temperature difference corresponds to the unstable atmospheric condition and positive air-sea temperature difference indicates the stable atmospheric condition. . . . 71
- 5.16 Seasonal variation of the daily averaged radar cross section difference between the Multi³Scat observations and CMOD5 value over two years (from January 2012 to August 2013), for different incidence angles; 35° (red), 45° (green), and 55° (blue). 72

- 5.17 C-band radar backscatter as a function of wind direction at unstable (red) and stable (blue) atmospheric conditions. 73
- 5.18 Radar cross section versus significant wave height in upwind direction, horizontal polarization, and incidence angles 35° (red), 45° (green), and 55° (blue). The small dots show the observations and the circles show the averaged values over 20 centimeters of wave height. 74
- 5.19 Directional dependence of RCS in low significant wave height (blue plus) and high significant wave height (red circle), at 35° (upper panels), 45° (middle panels), and 55° (lower panels), in VV-RCS (left), HH-RCS (middle), and VH-RCS (right). 75
- 6.1 CO_2 transfer velocity [cm/h] normalized with Sc number versus wind speed, from direct eddy covariance measurements in the Western Baltic Sea (red dots). Averaged value of transfer velocity over $0.5 \text{ m}/\text{s}$ classes of wind speed are shown in red filled circles. The error bars correspond to standard deviations of each window. The curves with gray patterns describe model results of Wanninkhof [1992] (star), Wanninkhof and McGillis [1999] (plus), Nightingale et al. [2000] (dot), Weiss et al. [2007] (circle). 81
- 6.2 Taylor diagram of gas transfer models of Wanninkhof [1992] (k92), Wanninkhof and McGillis [1999] (k99), Nightingale et al. [2000] (n2000), Weiss et al. [2007] (w2007) compared to the gas transfer computed from observations in the Western Baltic Sea. 83
- 6.3 Temporal variation of the CO_2 flux from observations (red dots) and four different calculated CO_2 fluxes using the gas transfer parameterizations presented in Table 2.1 (black dots). The data are time-averaged over the period from November 2011 to August 2012, providing one value every hour. The statistical comparison between the datasets are shown by the root mean square error between observations and calculated flux. The closest flux to observations is from Nightingale et al. [2000] with an RMSE of $0.28 \frac{\mu\text{mol}}{\text{m}^2\text{s}}$ 84
- 6.4 Averaged CO_2 transfer velocities [cm/h] normalized with Sc number versus wind speed of $0.5 \text{ m}/\text{s}$ classes, using observations a) from October 2011 to April 2012 and b) from April 2012 to October 2012, using direct eddy covariance measurements in the Western Baltic Sea (red circles). The error bars correspond to standard deviations at each wind class. The curves with black patterns are the outputs of the parameterizations introduced in Table 2.1. 86

6.5	The reproduced CO ₂ flux data (a) based on the seasonal variation of wind speed, solubility (b), partial pressure difference of CO ₂ (c), and air-sea temperature difference (d). Vertical dashed line indicate the season changes with respect to the coefficients used to reproduce CO ₂ flux from transfer velocity.	87
6.6	The simple schematic of the relationship between radar cross section and gas transfer velocity.	88
6.7	Upwind C-band RCS versus observed in situ CO ₂ transfer velocity in winter. Data are averaged over the measurements period, providing one single value for every 1 m/s wind speed.	90
6.8	Same as Figure 6.7, but in spring.	90
6.9	Upwind C-band RCS from Multi ³ Scat observations versus gas transfer velocity computed from the direct eddy covariance method, both in the Western Baltic Sea. The data are averaged over the period from November 2011 to August 2012, providing one data every 1 m/s wind speed. Red, green, and blue corresponds VV, HH, and VH polarization RCS, respectively.	92
6.10	The RCS-derived gas transfer velocity versus observed gas transfer velocity. Different panels corresponds to the different radar polarizations; VV (upper left), HH (upper right), and VH (lower left). The lower right panel compares the radar-based, observational, and modeled gas transfer velocities with the averaged datasets of 0.5 m/s wind speed.	93
6.11	Seasonal variation of the averaged gas transfer velocity in the Western Baltic Sea. The panel shows in red observational gas transfer velocity, in blue and turquoise the wind-based gas transfer velocities of Nightingale et al. [2000] and Weiss et al. [2007] , respectively, and in green colors the scatterometer-based gas transfer velocity.	94
6.12	C-band VH-RCS and gas transfer velocity from observations in the Western Baltic Sea in presence of unstable (red) and stable (blue) atmospheric stability.	95
6.13	RCS-based CO ₂ flux versus observations in the upwind direction. Statistics of the comparison are given in the panel.	96
6.14	Seasonal variation of the averaged CO ₂ flux in the Western Baltic Sea. The panel shows in dark blue the CO ₂ flux from eddy covariance system (direct observation) and in yellow the RCS-based flux computed from Equation 1.1 using our RCS-based gas transfer velocity.	97
6.15	Same as Figure 6.14 but for modified radar cross section considering the bias between the Multi ³ Scat C-band, VV polarization and CMOD5 results.	98

- A.1 L-band radar cross section measured by the Multi³Scat as a function of incidence angle, for wind speed ranges $5 - 7m/s$ (o) and $15 - 17m/s$ (+), at different polarization combinations, VV (red), HH (green), VH (blue), and different wind directions, Upwind (upper left), downwind (upper right), crosswind (lower left), (radar frequency: 1.0 GHz, wavelength: 30 cm). 109
- A.2 Same as Figure A.1 but for C-band RCS (radar frequency: 5.3 GHz, wavelength: 3.0 cm). 110
- A.3 Radar cross section in dB at 35° incidence angles as a function of wind speed in m/s , at four microwave frequencies (L-, S-, C-, X-band respectively from upper panel to lower panel), upwind direction and VV (red), HH (green), and VH (blue) polarization combinations. Each data point corresponds to averaged over 1 hour measurements and the lines show averaged value of radar cross section for windows of $0.5m/s$ wind speed. 111
- A.4 Radar cross section in dB at 45° incidence angles as a function of wind speed in m/s , at four microwave frequencies (L-, S-, C-, X-band respectively from upper panel to lower panel), upwind direction and VV (red), HH (green), and VH (blue) polarization combinations. Each data point corresponds to averaged over 1 hour measurements and the lines show averaged value of radar cross section for windows of $0.5m/s$ wind speed. 112
- A.5 Radar cross section in dB at 55° incidence angles as a function of wind speed in m/s , at four microwave frequencies (L-, S-, C-, X-band respectively from upper panel to lower panel), upwind direction and VV (red), HH (green), and VH (blue) polarization combinations. Each data point corresponds to averaged over 1 hour measurements and the lines show averaged value of radar cross section for windows of $0.5m/s$ wind speed. 113
- A.6 Directional signature of L-band Radar Cross Section in VV (circle), HH (plus), and VH (dot) polarizations, for incidence angles of 35° (upper panels), 45° (middle panels), and 55° (lower panels) in two cases of wind speed $6m/s$ (left column) and $14m/s$ (right column). 114
- A.7 Directional signature of S-band Radar Cross Section in VV (circle), HH (plus), and VH (dot) polarizations, for incidence angles of 35° (upper panels), 45° (middle panels), and 55° (lower panels) in two cases of wind speed $6m/s$ (left column) and $14m/s$ (right column). 115

A.8	Directional signature of X-band Radar Cross Section in VV (circle), HH (plus), and VH (dot) polarizations, for incidence angles of 35° (upper panels), 45° (middle panels), and 55° (lower panels) in two cases of wind speed 6m/s (left column) and 14m/s (right column).	116
A.9	Daily averaged radar cross section at C-band, VV polarization, 35° Incidence angle, the Multi ³ Scat observations (red circles) vs. CMOD5 model results (blue circles) data comparison under the same wind condition during one month measurements, upper left panel: January (mostly high wind speed), upper right: May (stable atmospheric stratification), lower left: October (neutral stratification), lower right: September (unstable stratification).	118
A.10	Same as Figure A.9 but for 45° Incidence angle.	119
A.11	Same as Figure A.9 but for 55° Incidence angle.	120
A.12	Polarization ratio in dB as a function of wind speed in downwind direction, at four different frequency bands (L-, S-, C-, and X-band) and three incidence angles (35° (red), 45° (green), and 55° (blue)). Each data point corresponds to averaged over 1 hour measurements.	121

List of Tables

2.1	Wind-based gas transfer velocity parameterizations applied in this study. . .	15
3.1	The scale of the waves that influence radar backscatter. The water wavelengths are calculated from equation 3.2 according to Bragg scattering theory.	19
4.1	Technical overview of the Multi ³ Scat instrument. Table explains the frequency, wavelength, antenna gain, and beam width for each particular microwave band.	33
5.1	Standard deviation (in [dB]) of the angular dependence of RCS measured by the Multi ³ Scat in different polarizations and incidence angles for S- and X-band microwave frequencies.	49
5.2	Slope of the angular dependence of RCS measured by the Multi ³ Scat and CMOD5-retrieved RCS and the related statistics at different wind conditions.	50
5.3	C-band and X-band polarization ratio model coefficients (5.1).	54
5.4	Coefficient polarization ratio as a function of incidence angles for different microwave frequency bands based on the observed data used in this study (5.4).	56
5.5	The slope of the radar cross section-wind dependence for different radar observation settings (frequency, polarization, and incidence angle).	58
6.1	The empirically determined coefficients of the scatterometer retrieved gas transfer velocity from the experiments by the Multi ³ Scat at different radar frequencies and polarizations and their related statistics.	91

Abbreviations

AT	total alkalinity
CMOD	C-band Model Function
EC-system	Eddy Covariance system
ECMWF	European Center for Medium-Range Weather Forecasts
ESA	European Space Agency
FINO-2	Forschungsplattformen in Nord und Ostsee No.2
GMF	Geophysical Model Function
IPCC	Intergovernmental Panel on Climate Change
MSS	Mean Square Slope
Multi³Scat	Multi-frequency/Multi-polarization Scatterometer
NCEP	National Center for Environmental Prediction
pH	potential of Hydrogen
PR	Polarization Ratio
RADAR	RAdio Detection And Ranging

RCS	Radar Cross Section
RMSE	Root Mean Square Error
SWH	Significant Wave Height
SST	Sea Surface Temperature
QuikSCAT	Quick recovery mission carrying SeaWinds instrument

Symbols

α	Solubility	$[mol\ m^{-3}\ atm^{-1}]$
ΔP_{CO_2}	Partial pressure difference of CO ₂	$[\mu\ atm]$
D_{heat}	Molecular diffusive coefficient of the heat	$[cm/h]$
F	CO ₂ Flux	$[\mu\ mol\ m^{-2}\ s^{-1}]$
H	Henry's law parameter	[dimensionless]
k	Wavenumber	$[rad/m]$
κ	Gas transfer velocity	$[cm/h]$
λ	Wavelength	[cm]
ϕ	Wind direction	[°]
φ	Azimuth direction	[°]
$\psi(k)$	Wavenumber spectrum	$[m^3\ rad^{-1}]$
Sc	Schmidt number	[dimensionless]
σ_0	Normalized Radar Cross Section	[dB]
θ	Incidence angle	[°]

Bibliography

- Aubinet, M., Vesala, T., and Papale, D. (2012). *Eddy covariance: a practical guide to measurement and data analysis*. Springer Science & Business Media.
- Banner, M. L. and Phillips, O. (1974). On the incipient breaking of small scale waves. *Journal of Fluid Mechanics*, 65(04):647–656.
- Barale, V. and Gade, M. (2008). *Remote sensing of the European seas*. Springer Science & Business Media.
- Bergeron, T., Bernier, M., Chokmani, K., Lessard-Fontaine, A., Lafrance, G., and Beaucage, P. (2011). Wind speed estimation using polarimetric radarsat-2 images: Finding the best polarization and polarization ratio. *IEEE Journal of Selected Topics in Applied Earth Observations and Remote Sensing*, 4(4):896–904.
- Bock, E. J., Hara, T., Frew, N. M., and McGillis, W. R. (1999). Relationship between air-sea gas transfer and short wind waves. *Journal of Geophysical Research: Oceans*, 104(C11):25821–25831.
- Bogucki, D., Carr, M.-E., Drennan, W. M., Woiceshyn, P., Hara, T., and Schmeltz, M. (2010). Preliminary and novel estimates of co2 gas transfer using a satellite scatterometer during the 2001 gasex experiment. *International Journal of Remote Sensing*, 31(1):75–92.
- Cole, J. J. and Caraco, N. F. (1998). Atmospheric exchange of carbon dioxide in a low-wind oligotrophic lake measured by. *Limnology and Oceanography*, 43(4):647–656.
- Colton, M. C., Plant, W. J., Keller, W. C., and Geernaert, G. L. (1995). Tower-based measurements of normalized radar cross section from lake ontario: Evidence of wind stress dependence. *Journal of Geophysical Research: Oceans*, 100(C5):8791–8813.
- Donelan, M. A. and Pierson, W. J. (1987). Radar scattering and equilibrium ranges in wind-generated waves with application to scatterometry. *Journal of Geophysical Research: Oceans*, 92(C5):4971–5029.

- Elfouhaily, T., Chapron, B., Katsaros, K., and Vandemark, D. (1997). A unified directional spectrum for long and short wind-driven waves. *Journal of Geophysical Research: Oceans*, 102(C7):15781–15796.
- Fangohr, S., Woolf, D. K., Jeffery, C. D., and Robinson, I. S. (2008). Calculating long-term global air-sea flux of carbon dioxide using scatterometer, passive microwave, and model reanalysis wind data. *Journal of Geophysical Research: Oceans*, 113(C9).
- Frew, N. M., Glover, D. M., Bock, E. J., and McCue, S. J. (2007). A new approach to estimation of global air-sea gas transfer velocity fields using dual-frequency altimeter backscatter. *Journal of Geophysical Research: Oceans*, 112(C11).
- Garbe, C. S., Handler, R. A., and Jähne, B. (2014a). *Transport at the Air-sea Interface*. Springer.
- Garbe, C. S., Rutgersson, A., Boutin, J., De Leeuw, G., Delille, B., Fairall, C. W., Gruber, N., Hare, J., Ho, D. T., Johnson, M. T., et al. (2014b). Transfer across the air-sea interface. In *Ocean-Atmosphere Interactions of Gases and Particles*, pages 55–112. Springer.
- Glover, D. M., Frew, N. M., and McCue, S. J. (2007). Air-sea gas transfer velocity estimates from the Jason-1 and TOPEX altimeters: Prospects for a long-term global time series. *Journal of Marine Systems*, 66(1):173–181.
- Glover, D. M., Frew, N. M., McCue, S. J., and Bock, E. J. (2002). A multi-year time series of global gas transfer velocity from the TOPEX dual frequency, normalized radar backscatter algorithm. *Gas Transfer at Water Surfaces*, pages 325–331.
- Goddijn-Murphy, L., Woolf, D. K., Chapron, B., and Queffelec, P. (2013). Improvements to estimating the air-sea gas transfer velocity by using dual-frequency, altimeter backscatter. *Remote Sensing of Environment*, 139:1–5.
- Hasse, L. (1980). Gas exchange across the air-sea interface. *Tellus*, 32(5):470–481.
- Hersbach, H. (2003). Cmod5 an improved geophysical model function for ers c-band scatterometry, /techn. mem./, ecmwf. Reading, UK.
- Hersbach, H., Stoffelen, A., and De Haan, S. (2007). An improved c-band scatterometer ocean geophysical model function: Cmod5. *Journal of Geophysical Research: Oceans*, 112(C3).
- Hinrichs, I. (2014). Bestimmung des zeitabhängigen CO₂-Gasaustauschs über dem globalen eisfreien Ozean unter Verwendung von Winddaten aus satellitengestützten Messungen.

- Ho, D. T., Law, C. S., Smith, M. J., Schlosser, P., Harvey, M., and Hill, P. (2006). Measurements of air-sea gas exchange at high wind speeds in the southern ocean: Implications for global parameterizations. *Geophysical Research Letters*, 33(16).
- Hwang, P. A. (2005). Wave number spectrum and mean square slope of intermediate-scale ocean surface waves. *Journal of Geophysical Research: Oceans*, 110(C10).
- Hwang, P. A. and Fois, F. (2015). Surface roughness and breaking wave properties retrieved from polarimetric microwave radar backscattering. *Journal of Geophysical Research: Oceans*, 120(5):3640–3657.
- Hwang, P. A., Zhang, B., Toporkov, J. V., and Perrie, W. (2010). Comparison of composite bragg theory and quad-polarization radar backscatter from radarsat-2: With applications to wave breaking and high wind retrieval. *Journal of Geophysical Research: Oceans*, 115(C8).
- Jähne, B., Libner, P., Fischer, R., Billen, T., and Plate, E. (1989). Investigating the transfer processes across the free aqueous viscous boundary layer by the controlled flux method. *Tellus B*, 41(2):177–195.
- Jähne, B., Münnich, K. O., Bössinger, R., Dutzi, A., Huber, W., and Libner, P. (1987). On the parameters influencing air-water gas exchange. *Journal of Geophysical Research: Oceans*, 92(C2):1937–1949.
- Jones, W. L. and Schroeder, L. (1978). Radar backscatter from the ocean: dependence on surface friction velocity. *Boundary-Layer Meteorology*, 13(1-4):133–149.
- Jonsson, A., Åberg, J., Lindroth, A., and Jansson, M. (2008). Gas transfer rate and co₂ flux between an unproductive lake and the atmosphere in northern sweden. *Journal of Geophysical Research: Biogeosciences*, 113(G4).
- Keller, W. C., Plant, W. J., and Weissman, D. E. (1985). The dependence of x band microwave sea return on atmospheric stability and sea state. *Journal of Geophysical Research: Oceans*, 90(C1):1019–1029.
- Keller, W. C., Wismann, V., and Alpers, W. (1989a). Tower-based measurements of the ocean c band radar backscattering cross section. *Journal of Geophysical Research: Oceans*, 94(C1):924–930.
- Keller, W. C., WISMANN, Y., and Alpers, W. (1989b). Radar backscattering cross section. *Journal of Geophysical Research*, 94(C1):924–930.

- Kern, S., Brath, M., Fontes, R., Gade, M., Gurgel, K.-W., Kaleschke, L., Spreen, G., Schulz, S., Winderlich, A., and Stammer, D. (2009). Multi scata helicopter-based scatterometer for snow-cover and sea-ice investigations. *IEEE Geoscience and Remote Sensing Letters*, 6(4):703–707.
- Kudryavtsev, V., Hauser, D., Caudal, G., and Chapron, B. (2003). A semiempirical model of the normalized radar cross-section of the sea surface 1. background model. *Journal of Geophysical Research: Oceans*, 108(C3).
- Lammert, A. and Ament, F. (2015). Co 2-flux measurements above the baltic sea at two heights: flux gradients in the surface layer? *Earth System Science Data*, 7(2):311–317.
- Lansø, A. S., Bendtsen, J., Christensen, J., Sørensen, L., Chen, H., Meijer, H., and Geels, C. (2015). Sensitivity of the air–sea co 2 exchange in the baltic sea and danish inner waters to atmospheric short-term variability. *Biogeosciences*, 12(9):2753–2772.
- Leppäranta, M. and Myrberg, K. (2009). *Physical oceanography of the Baltic Sea*. Springer Science & Business Media.
- Liss, P. S. and Merlivat, L. (1986). Air-sea gas exchange rates: Introduction and synthesis. In *The role of air-sea exchange in geochemical cycling*, pages 113–127. Springer.
- Long, D. G., Barrowes, B. E., and Arnold, D. V. (1999). Radar cross section dependence on wind speed. In *Geoscience and Remote Sensing Symposium, 1999. IGARSS'99 Proceedings. IEEE 1999 International*, volume 3, pages 1863–1865. IEEE.
- Long, D. G., Collyer, R., and Arnold, D. V. (1996). Dependence of the normalized radar cross section of water waves on bragg wavelength-wind speed sensitivity. *IEEE Transactions on Geoscience and Remote Sensing*, 34(3):656–666.
- Melville, W. (1996). The role of surface-wave breaking in air-sea interaction. *Annual review of fluid mechanics*, 28(1):279–321.
- Mouche, A. A., Hauser, D., and Kudryavtsev, V. (2006). Radar scattering of the ocean surface and sea-roughness properties: A combined analysis from dual-polarizations airborne radar observations and models in c band. *Journal of Geophysical Research: Oceans*, 111(C9).
- Nightingale, P. D., Liss, P. S., and Schlosser, P. (2000). Measurements of air-sea gas transfer during an open ocean algal bloom. *Geophysical Research Letters*, 27(14):2117–2120.

- Pachauri, R. K., Allen, M. R., Barros, V. R., Broome, J., Cramer, W., Christ, R., Church, J. A., Clarke, L., Dahe, Q., Dasgupta, P., et al. (2014). *Climate change 2014: synthesis report. Contribution of Working Groups I, II and III to the fifth assessment report of the Intergovernmental Panel on Climate Change*. IPCC.
- Phillips, O. (1988). Radar returns from the sea surface bragg scattering and breaking waves. *Journal of physical oceanography*, 18(8):1065–1074.
- Plant, W., Keller, W., and Weissman, D. (1985). The dependence of the microwave radar cross section on the air-sea interaction and the wave slope. In *The Ocean Surface*, pages 289–296. Springer.
- Plant, W. and Wright, J. (1977). Growth and equilibrium of short gravity waves in a wind-wave tank. *Journal of Fluid Mechanics*, 82(04):767–793.
- Plant, W. J. (1990). Bragg scattering of electromagnetic waves from the air/sea interface. In *Surface waves and fluxes*, pages 41–108. Springer.
- Robinson, I. S. (2004). *Measuring the oceans from space: the principles and methods of satellite oceanography*. Springer Science & Business Media.
- Romeiser, R., Alpers, W., and Wismann, V. (1997). An improved composite surface model for the radar backscattering cross section of the ocean surface: 1. theory of the model and optimization/validation by scatterometer data. *Journal of Geophysical Research: Oceans*, 102(C11):25237–25250.
- Rufenach, C. (1995). A new relationship between radar cross-section and ocean surface wind speed using ers-t scatterometer and buoy measurements. *International Journal of Remote Sensing*, 16(18):3629–3647.
- Rutgersson, A., Norman, M., and Åström, G. (2009). Atmospheric co₂ variation over the baltic sea and the impact on air–sea exchange. *Boreal environment research*, 14(1):238–249.
- Rutgersson, A., Norman, M., Schneider, B., Pettersson, H., and Sahlée, E. (2008). The annual cycle of carbon dioxide and parameters influencing the air–sea carbon exchange in the baltic proper. *Journal of Marine Systems*, 74(1):381–394.
- Schneider, B., Gustafsson, E., and Sadkowiak, B. (2014). Control of the mid-summer net community production and nitrogen fixation in the central baltic sea: an approach based on pco₂ measurements on a cargo ship. *Journal of Marine Systems*, 136:1–9.

- Schneider, B., Kaitala, S., Raateoja, M., and Sadkowiak, B. (2009). A nitrogen fixation estimate for the baltic sea based on continuous pco₂ measurements on a cargo ship and total nitrogen data. *Continental Shelf Research*, 29(11):1535–1540.
- Seifert, T., Tauber, F., and Kayser, B. (2001). A high resolution spherical grid topography of the baltic sea 2nd edition. *Baltic Sea Science Congress, Stockholm*, 147:147.
- Shao, W., Zhang, Z., Li, X., and Wang, W. (2016). Sea surface wind speed retrieval from terrasar-x hh polarization data using an improved polarization ratio model. *IEEE Journal of Selected Topics in Applied Earth Observations and Remote Sensing*, 9(11):4991–4997.
- Soloviev, A., Donelan, M., Graber, H., Haus, B., and Schlüssel, P. (2007). An approach to estimation of near-surface turbulence and co₂ transfer velocity from remote sensing data. *Journal of Marine Systems*, 66(1):182–194.
- Stammer, D. (2017). Multi-frequency / multi-polarization scatterometer measurements in the western baltic sea in support of air-sea flux studies. *In preparation*, 0(0).
- Takahashi, T., Sutherland, S. C., Sweeney, C., Poisson, A., Metz, N., Tilbrook, B., Bates, N., Wanninkhof, R., Feely, R. A., Sabine, C., et al. (2002). Global sea–air co₂ flux based on climatological surface ocean pco₂, and seasonal biological and temperature effects. *Deep Sea Research Part II: Topical Studies in Oceanography*, 49(9):1601–1622.
- Takahashi, T., Sutherland, S. C., Wanninkhof, R., Sweeney, C., Feely, R. A., Chipman, D. W., Hales, B., Friederich, G., Chavez, F., Sabine, C., et al. (2009). Climatological mean and decadal change in surface ocean pco₂, and net sea–air co₂ flux over the global oceans. *Deep Sea Research Part II: Topical Studies in Oceanography*, 56(8):554–577.
- Thompson, D. R., Elfouhaily, T. M., and Chapron, B. (1998). Polarization ratio for microwave backscattering from the ocean surface at low to moderate incidence angles. In *Geoscience and Remote Sensing Symposium Proceedings, 1998. IGARSS'98. 1998 IEEE International*, volume 3, pages 1671–1673. IEEE.
- Ulaby, F. T., Moore, R. K., and Fung, A. K. (1982). Microwave remote sensing active and passive-volume ii: Radar remote sensing and surface scattering and emission theory.
- Vachon, P. W. and Wolfe, J. (2011). C-band cross-polarization wind speed retrieval. *IEEE Geoscience and Remote Sensing Letters*, 8(3):456–459.
- Valenzuela, G. R. (1978). Theories for the interaction of electromagnetic and oceanic waves a review. *Boundary-Layer Meteorology*, 13(1):61–85.

- Wanninkhof, R. (1992). Relationship between wind speed and gas exchange over the ocean. *Journal of Geophysical Research: Oceans*, 97(C5):7373–7382.
- Wanninkhof, R., Asher, W. E., Ho, D. T., Sweeney, C., and McGillis, W. R. (2009). Advances in quantifying air-sea gas exchange and environmental forcing. *Annual Review of Marine Science*, 1:213–244.
- Wanninkhof, R. and McGillis, W. R. (1999). A cubic relationship between air-sea CO₂ exchange and wind speed. *Geophysical Research Letters*, 26(13):1889–1892.
- Webb, E. K., Pearman, G. I., and Leuning, R. (1980). Correction of flux measurements for density effects due to heat and water vapour transfer. *Quarterly Journal of the Royal Meteorological Society*, 106(447):85–100.
- Weiss, A., Kuss, J., Peters, G., and Schneider, B. (2007). Evaluating transfer velocity-wind speed relationship using a long-term series of direct eddy correlation CO₂ flux measurements. *Journal of Marine Systems*, 66(1):130–139.
- Weiss, R. (1974). Carbon dioxide in water and seawater: the solubility of a non-ideal gas. *Marine chemistry*, 2(3):203–215.
- Wentz, F., Petehtych, S., and Thomas, L. (1984). A model function for ocean radar cross sections at 14.6 GHz. *Journal of Geophysical Research: Oceans*, 89(C3):3689–3704.
- Wesslander, K., Hall, P., Hjalmarsson, S., Lefevre, D., Omstedt, A., Rutgersson, A., Sahlée, E., and Tengberg, A. (2011). Observed carbon dioxide and oxygen dynamics in a Baltic sea coastal region. *Journal of Marine Systems*, 86(1):1–9.
- Wright, J. (1968). A new model for sea clutter. *IEEE Transactions on antennas and propagation*, 16(2):217–223.
- Yu, T., He, Y., Song, J., Shen, H., Wang, J., and Gao, G. (2014). Uncertainty in air-sea CO₂ flux due to transfer velocity. *International Journal of Remote Sensing*, 35(11-12):4340–4370.
- Zappa, C. J., Asher, W., and Jessup, A. (2001). Microscale wave breaking and air-water gas transfer. *Journal of Geophysical Research: Oceans*, 106(C5):9385–9391.
- Zappa, C. J., Asher, W., Jessup, A., Klinke, J., and Long, S. (2004). Microbreaking and the enhancement of air-water transfer velocity. *Journal of Geophysical Research: Oceans*, 109(C8).

Zhang, B., Perrie, W., Hwang, P. A., and He, Y. (2010). A new polarization ratio model from c-band radarsat-2 fine quad-pol imagery. In *Geoscience and Remote Sensing Symposium (IGARSS), 2010 IEEE International*, pages 1948–1951. IEEE.

Acknowledgements

My sincere gratitude goes first to my supervisor, Prof. Dr. Detlef Stammer, who expertly guided and supported me during my Ph.D. study. His skillful guidance, innovative ideas, and unwavering enthusiasm for research in physical oceanography and ocean remote sensing kept me constantly engaged with my research. I truly enjoyed working in his group and under his supervision.

I would like to especially thank the valuable input of my co-adviser, Dr. Martin Gade. His patient in teaching the experimental design and analysis methods, in combination with his constructive comments, and his support during my Ph.D. study, helped me to shape this work. Thanks also go to my advisory panel, Prof. Felix Ament, for the useful discussions and his helpful suggestions.

I would like to acknowledge the technical group of the University of Hamburg, institute of oceanography, for technical support during the scatterometer measurements and data processing, Thomas Schlick, Mayk Fischer, and Frauke Grawe.

The work was supported by the SOPRAN project and the Federal Ministry of Education and Research (BMBF).

I would like to thank the institutions that provided the data used in this study:

The meteorological data from the FINO-2 platform (the Forschungsplattformen in Nord- und Ostsee) and buoy data provided by Bundesamt für Seeschifffahrt und Hydrographie (BSH) are greatly acknowledged. The Institute of Warnemünde is thanked for providing the partial pressure of CO₂. The University of Hamburg, Institute of meteorology is greatly thanked for providing the CO₂ flux data.

I thank my office mate Xin, for making my stay in the office pleasant, and lots of constructive remarks. Thanks to all my colleagues in the Remote Sensing and Assimilation Group of the Institute of Oceanography for their friendly supports and help. A big thank you to Mark and Meike for proof reading. This acknowledgment would not be completed without mentioning my friends, not only for helpful comments but also for everything beyond work; Elina, Maciej, Norman, Oleksandr, Yulia, and our new friend Sayantani.

I would like to especially thank Lennart Rueggen, for the discussion, helps, supports,

and understanding in difficult times. Finally, my deepest appreciation belongs to my family; Mother, Father, Sister, and Brother in law, for their patient, understanding, and support from far way, especially my uncle, Siamak Ghobadian, for all his support and caring.